MULTI-SCALE MODELING OF MICROSTRUCTURAL EVOLUTION IN STRUCTURAL METALLIC SYSTEMS

By

Lei Zhao

A dissertation submitted in partial fulfillment of
the requirements for the degree of

Doctor of Philosophy
(Materials Science)

at the

UNIVERSITY OF WISCONSIN–MADISON

2017

Date of final oral examination: 09/07/2017

The dissertation is approved by the following members of the Final Oral Committee:

Dane Morgan, Professor, Department of Materials Science & Engineering
John Perepezko, Professor, Department of Materials Science & Engineering
Shiva Rudraraju, Assistant Professor, Department of Mechanical Engineering
Izabela Szlufarska, Professor, Department of Materials Science & Engineering
Paul Voyles, Professor, Department of Materials Science & Engineering

Abstract

Metallic alloys are a widely used class of structural materials, and the mechanical properties of these alloys are strongly dependent on the microstructure. Therefore, the scientific design of metallic materials with superior mechanical properties requires the understanding of the microstructural evolution. Computational models and simulations offer a number of advantages over experimental techniques in the prediction of microstructural evolution, because they can allow studies of microstructural evolution in situ, i.e., while the material is mechanically loaded (meso-scale simulations), and bring atomic-level insights into the microstructure (atomistic simulations). In this thesis, we applied a multi-scale modeling approach to study the microstructural evolution in several metallic systems, including polycrystalline materials and metallic glasses (MGs).

Specifically, for polycrystalline materials, we developed a coupled finite element model that combines phase field method and crystal plasticity theory to study the plasticity effect on grain boundary (GB) migration. Our model is not only coupled strongly (i.e., we include plastic driving force on GB migration directly) and concurrently (i.e., coupled equations are solved simultaneously), but also it qualitatively captures such phenomena as the dislocation absorption by mobile GBs. The developed model provides a tool to study the microstructural evolution in plastically deformed metals and alloys.

For MGs, we used molecular dynamics (MD) simulations to investigate the nucleation kinetics in the primary crystallization in Al-Sm system. We calculated the time-temperature-transformation curves for low Sm concentrations, from which the strong suppressing effect of Sm solute on Al nucleation and its influencing mechanism are revealed. Also, through the comparative analysis of both Al attachment and Al diffu-

sion in MGs, it has been found that the nucleation kinetics is controlled by interfacial attachment of Al, and that the attachment behavior takes place collectively and heterogeneously, similarly to Al diffusion in MGs.

Finally, we applied the MD technique to study the origin of five-fold twinning nucleation during the solidification of Al base alloys. We studied several model alloys and reported the observed nucleation pathway. We found that the key factors controlling the five-fold twinning are the twin boundary energy and the formation of pentagon structures, and the twin boundary energy plays the dominant role in the five-fold twinning in the model alloys studied.

Table of Contents

List of Figures

List of Tables

List of Terminology

BC	Boundary condition
BCC	Body-centered cubic
CNA	Common neighbor analysis
CNT	Classical nucleation theory
CPFE	Crystal plasticity finite element
DA	Diffusing atom
EAM	Embedded atom method
FCC	Face-centered cubic
FS	Finnis-Sinclair
GB	Grain boundary
HCP	Hexagonal close packed
iQC	icosahedral quasicrystal
JFNK	Jacobian-free Newton-Krylov
MC	Monte Carlo
MD	Molecular dynamics
MG	Metallic glass
MRO	Medium-range order
NNA	Nearest neighbor analysis
NNI	Nearest neighbor index
PDE	Partial differential equation
SRO	Short-range order
TB	Twin boundary
TTT	Time−temperature−transformation
VP	Voronoi polyhedra

Acknowledgments

First, I would like to express my deepest appreciation to my advisor Prof. Izabela Szlufarska, who has offered me continuous and precious guidance and support in the past 5 memorable years, not only in my studies and research, but also in my life and career plan. Prof. Izabela Szlufarska is always happy to provide very helpful advice on how to overcome obstacles in my research and make consistent progress. Without her guidance, it is not possible for me to accomplish my doctoral studies or this dissertation. Also, Prof. Izabela Szlufarska kindly provides great help and support in my life and career. For example, I really appreciate her understanding and support in the overwhelming days of my daughter's birth, as well as her help in my career preparation and job search. I am really impressed by, and have learned a lot from Prof. Izabela Szlufarska's great dedication to science, professional attitude and enthusiasm, and pleasant personality.

I would like to express my sincere gratitude to my collaborators in different stages of my doctoral studies. Specifically, I thank Dr. Mike Tonks from University of Florida and Dr. Pritam Chakraborty from India Institute of Technology, who were then both from Idaho National Laboratory (INL) and have given me great help in the development of our coupled phase field model. I am also grateful to Prof. John Perepezko for his helpful guidance and suggestions in the project of nucleation kinetics in metallic glasses. Prof. John Perepezko's immense knowledge and great dedication to research really impress me. In addition, I express my sincere gratitude to Prof. Dane Morgan and Prof. Paul Voyles, who provide me lots of helpful suggestions and comments on my work. Prof. Dane Morgan also kindly offers his help in my job search. Finally, I would like to thank Dr. George Bokas, who works closely with me in the past years and is always happy to offer his patient help in the project of metallic glasses. I would never have made such

accomplishments without the great help from these collaborators.

I thank all members in the Computational Materials Group at University of Wisconsin - Madison (UW-Madison), led by Prof. Izabela Szlufarska and Prof. Dane Morgan. I also appreciate the help from MOOSE and MARMOT teams at INL. I thank both INL and Center for High Throughput Computing at UW-Madison for the computing resources.

I greatly appreciate the time and support from my thesis committee members, including Prof. Dane Morgan, Prof. John Perepezko, Prof. Shiva Rudraraju, Prof. Izabela Szlufarska, and Prof. Paul Voyles.

I appreciate the funding support from the U.S. Army Research Office under grant No. W911NF-12-1-0548, and the NSF-DMREF under grant No. DMR-1332851, without which this work could not have been done.

Finally, I would like to express my sincere gratitude to my families, including my wife Qing, daughter Alice, parents, parents in law and sisters. It is their understanding and support that give me the most significant motivation in the past years.

Chapter 1 : Introduction

1.1 Importance of microstructure in metallic materials

Metallic materials (metals and alloys) are the most important type of structural materials in human civilization and industrialization. Strength, hardness, wear resistance, corrosion resistance, castability and plasticity are among the desirable mechanical properties of structural metallic materials. Design of materials with superior performance is the ultimate goal in the research of metallic materials.

Since the materials science and engineering is comprised of four primary critical elements: processing, structure, properties and performance, therefore the systematic materials design requires the understanding of the interconnections between these four primary elements, as shown in the paradigm in Fig. 1.1. As Fig. 1.1 suggests, the deductive cause-and-effect logic of science flows to the right, while the inductive goal-means relations of engineering flow to the left. Structure is at the heart of the paradigm connecting processing with properties. In the hierarchy of material structures, microstructure (i.e., the appearance of the material on the nm-cm length scale) offers the richest variety of structural arrangements. Access to this variety is often conveniently available through simple processing such as heat treatment and mechanical deformation. As material structure determines its properties, engineering a target microstructural state with desired properties therefore becomes the critical task in materials design. Once the realm of the target microstructure has been identified, the key to the design of microstructures is an understanding of microstructural evolution.

According to the pattern of the atomic packing in the microstructure, metallic systems can be classified into crystalline materials and metallic glasses (MGs). In this thesis,

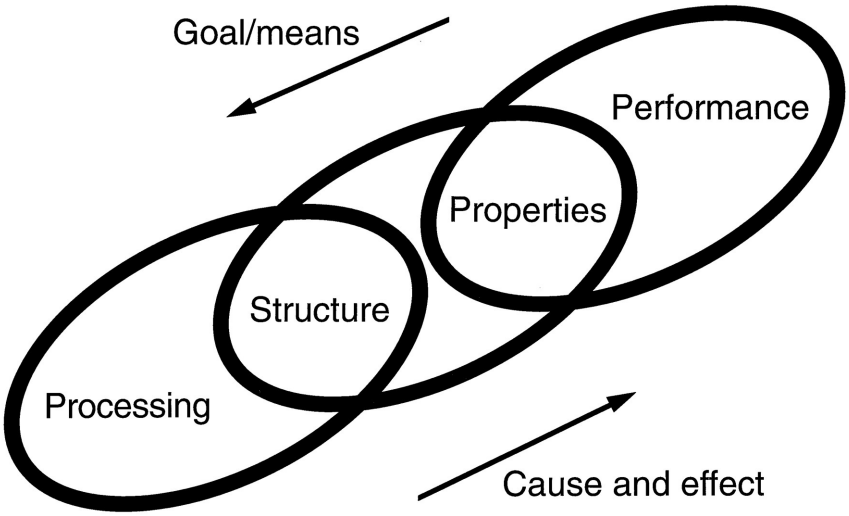

Fig. 1.1: The materials science and engineering paradigm that shows the structure connects processing with properties [1].

we study the microstructural evolution in both two classes of materials. In crystalline metals and alloys, the constituent atoms are arranged on a lattice with a long range order, except for the interruptions by materials defects. The microstructure in crystalline materials is comprised of phases, phase boundaries, grains, grain boundaries (GBs), dislocations, etc. In contrast, MGs lack the long-range order and only exhibit short-range order (SRO) and medium-range order (MRO). Commonly, SRO is characterized by Voronoi polyhedrons (VPs) and MRO by the arrangement of VPs into networks. Therefore, SRO and MRO, together with the possible crystal nuclei and crystal particles (if any), comprise the scope of microstructure in MGs. In the following sections, both the crystalline metallic materials and MGs will be introduced.

1.2 Crystalline metals and alloys

Crystalline metals and alloys typically possess high strength and hardness, fatigue resistance and good malleability, and therefore are used in a wide variety of applications. There are several strengthening mechanisms to improve the mechanical properties of

crystalline metals and alloys, such as work hardening, solid solution strengthening, precipitation hardening and GB strengthening, etc. To take a concrete example, GB strengthening by means of grain refinement is one of the common techniques to enhance materials properties in polycrystalline metals and alloys. Grain size has a tremendous influence on the mechanical behaviors, because GBs act as an impediment to dislocation motion in plastic deformation. The grain size dependence of materials strength can be mathematically described as the Hall-Petch relationship:

$$\sigma_{\mathrm{y}} = \sigma_0 + \frac{k_{\mathrm{y}}}{\sqrt{d}}, \tag{1.1}$$

where σ_{y} is the yield strength, σ_0 is the reference yield strength, k_{y} is a constant, and d is the average grain diameter in the polycrystals.

Although typical grain refinement can increase the yield strength for ultrafine- and nano-grained materials, this strength enhancement often comes at the expense of degraded ductility. It has been reported [2, 3] that bulk ultrafine- and nano-grained alloys with fine twin structures can achieve a combination of both high strength and good tensile ductility. This is because, in the presence of pre-existing fine twins, the dominant slip mechanism changes from full dislocation activities to twin boundary (TB) migration, which can accommodate a considerable amount of plastic strain. Therefore, TB strengthening becomes an important strategy for microstructure engineering. Among the twin structures, five-fold twins (five $\{111\}$ neighboring twins that share a common $\langle 110 \rangle$ direction and have a five-fold symmetry relationship) are of particular interest, not only because they introduce TBs and increase materials strength while preserving ductility, but also because they are suggested to correlate with effective grain refinement [4–6] and to be responsible for the formation of twined dendrites in Al alloys [7, 8]. However, the formation mechanism of five-fold twins has not been well understood. In this thesis, we used molecular dynamics (MD) simulation to study the five-fold twinning of

model systems, since MD method is a powerful tool to reveal the atomic-level behaviors underlying the crystallization and therefore can offer many precious insights into the nucleation mechanism of five-fold twinning in Al alloys.

Apart from the application of aforementioned strengthening mechanisms to design the desirable microstructure, the prediction of microstructure degradation of in-service materials is equally important for their performance and lifetime. Under the effects of mechanical deformation, temperature and aging, the microstructure can be degraded due to grain coarsening, solute segregation to interfaces, precipitation of detrimental phases, fatigue and creep, etc. Therefore, understanding the microstructural evolution of materials *in operando* is crucial in advanced material design. Among all the adverse factors in the service environment of structural materials, plastic deformation is one of the most common and it would result in grain coarsening, creep, recrystallization, crack initiation and propagation, etc. Considering the limitations of experimental approaches, understanding the way how plastic deformation fundamentally affects the microstructural evolution requires one to develop a computational model to study the plasticity effect on GB migration.

Phase field method is a useful and versatile technique for modeling the microstructural evolution. Therefore, in this thesis we coupled concurrently and strongly the phase field model with the crystal plasticity theory to simulate the plasticity driven GB migration. The developed coupling framework has been implemented into MOOSE/MARMOT simulation package.

1.3 Metallic glasses

MGs are solid metallic materials with disordered atomic-scale structures, i.e., they have glass-like atomic arrangements. Unlike common glasses, such as window glasses which are transparent and typically electrical insulators, MGs are opaque and have good elec-

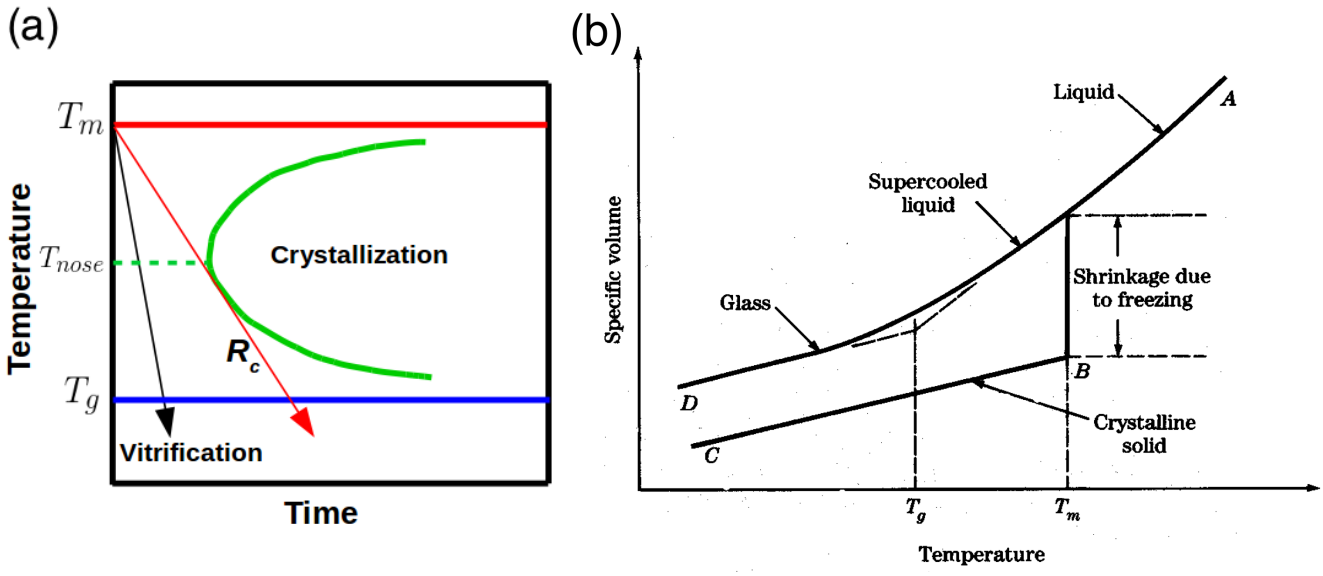

Fig. 1.2: (Color online) (a) Schematic representation of TTT curve for solidification and (b) Change of specific volume during the cooling of liquid alloys.

trical conductivity. Compared to crystalline metals and alloys, MGs usually have very attractive mechanical properties such as high strength and high elastic limit, high resistance to wear and corrosion, as well as good biocompatibility [9–15]. Therefore, MGs have attracted a lot of interest since they were first reported in 1960 by Duwez *et al.* [16]. However, the low glass forming ability (GFA) of some alloys such as Al-base systems has so far hindered synthesis of the bulk samples and therefore limited the engineering applications of these materials. Therefore, lots of efforts have been devoted towards developing alloys with high GFA [9, 17, 18].

There are several approaches in which MGs can be produced, including extremely rapid cooling (or melt quenching), physical vapor deposition, solid-state reaction, ion irradiation, and mechanical alloying [19, 20]. Rapid cooling is the most common technique to prepare MGs. As shown in the time−temperature−transformation (TTT) curve in Fig. 1.2a, if the liquid alloy is cooled down at a cooling rate higher than the critical cooling rate R_c, the crystallization would be frustrated and the supercooled liquid

would vitrify once the temperature reaches below the glass transition temperature T_g. Fig. 1.2b shows the change of specific volume as the alloy cools down for two extreme cases, including crystallization and glass transition. As the first-order phase transition, crystallization is usually accompanied by an abrupt drop of materials properties such as specific volume and enthalpy around the melting temperature T_m. In contrast, glass transition is a second-order phase transformation, and the specific volume and enthalpy decrease continuously as the glass transition takes place at T_g. In spite of the knowledge of the preparation methods of MGs, the nature of glass transition and GFA of alloys are still yet to be well understood, and they have been undergoing intensive research.

According to whether the crystallization nucleation can be avoided entirely in typical experimental conditions, MGs can be classified to bulk metallic glass (BMG) formers and marginal glass formers. BMGs are relatively better glass formers and their synthesis is nucleation controlled. In contrast, the marginal glass formers usually have very high R_c and the occurrence of nucleation is often inevitable. Therefore, rapid quenching by melt spinning technique (the cooling rate of 10^3 - 10^6 K/s can be achieved typically) is usually used to control the growth of the fine nuclei. R_c directly quantifies the GFA of alloys. The lower the value of R_c is, the higher the GFA is. For Al base alloys, which are all marginal glass formers, the values of R_c typically range from 10^4 to 10^6 K/s [21, 22].

Despite the key role of R_c in the research of MGs, experimental challenges have limited its measurement to a minute fraction of known glass formers. Also, usually computational methods cannot be applied for calculating R_c due to limited time scales of molecular simulations. Therefore, it is difficult to identify the alloy compositions with good GFA. In order to overcome this challenge, some empirical temperature-related indicators have been proposed to infer the relative GFA [23, 24]. These empirical indicators include T_g/T_l, T_x/T_l, $T_x/(T_g + T_l)$, etc., where T_g, T_l and T_x are the glass transition temperature, liquidus temperature, and the onset crystallization temperature, respectively. However, the aforementioned empirical indicators are not robust and they require the

experimental preparation of an alloy to measure T_g, T_l, and T_x. More recently, structural descriptors of MGs have been proposed to infer the GFA of alloys, such as the icosahedral VPs and superclusters. For instance, it has been found [20] that during the rapid solidification of Al-Sm MG, the population of icosahedral VPs keeps increasing with the decreasing temperature, and the maximum icosahedral-ordering has been found in $Al_{90}Sm_{10}$ alloy, which is consistent with the range of compositions (8.0 at.% - 16.0 at.%) found experimentally with high GFA. Therefore, understanding the structural evolution during the rapid quenching of alloys is not only helpful to the understanding of glass transition nature, but also critical to the design of MGs with good GFA.

As mentioned earlier, Al-based alloys are all marginal glass formers, and the rapid quenched Al-based MGs are usually characterized by a primary crystallization reaction upon heating, which produces a high density of Al nano-scale crystalline particles and consequently enhances the mechanical properties of alloys [25–27]. For instance, the fracture strength of the dispersion-strenthened MGs can be 20% - 120% higher than that of pure amorphous MGs [28–30]. The origin of the high density of fine Al crystals is still under debate, and it may result from the quenched-in nuclei [26, 27] or nucleation at a potent heterogeneous site upon heating [31]. In addition, the effects of micro-alloying on the nucleation kinetics, especially on the atomic level, during the nanocrystallization were poorly studied previously. A knowledge of such effects will undoubtedly contribute to the understanding of the GFA of alloys. In this thesis, we used MD simulation method to study the nucleation kinetics and to identify the micro-alloying effect in the primary crystallization of Al-Sm MG.

1.4 Overview of the thesis

The remainder of the thesis is organized as follows. In Chap. 2, we introduce the computational tools used in this study. We first introduce the general concept of phase field

description of microstructure, followed by the phase field grain growth model. Then we briefly introduce the crystal plasticity theory. Finally we discuss the MD simulation technique, including the general simulation process and the common neighbor analysis.

In Chap. 3, we introduce the development of the multi-physics model which couples concurrently and strongly the phase field model with crystal plasticity theory. The derivation of the plastic driving force and the strategy for solving the coupled equations are introduced first. Then we discuss the model parameters including GB properties and crystal plasticity model parameters. Finally a bicrystal simulation example is used to demonstrate the effect of plasticity on GB migration.

In Chap. 4, we study the isothermal nucleation kinetics in Al-Sm MGs using MD simulations. First we calculate the time-temperature-transformation curves for low Sm concentrations, from which the Sm alloying effect and its influencing mechanism are revealed. Subsequently, the Al nucleation attachment mechanism is also identified and compared to the mechanism of Al diffusion in MGs.

In Chap. 5, we use MD simulations to investigate the nucleation mechanism of five-fold twins in Al model alloys. Our MD simulations reveal a new nucleation pathway, which does not require the participation of any nucleation templates. From the nucleation pathway, we identify two key factors, that is, the TB energy and the formation of pentagon structures. Through correlating each factor with the twinning propensity and five-fold twinning frequency, it is found that the TB energy plays the dominant role in the five-folding twinning for the model systems studied.

Finally, Chap. 6 concludes this thesis and briefly discusses some interesting directions that may be worthy of investigation in the future.

References

[1] Gregory B Olson. Computational design of hierarchically structured materials. *Science*, 277(5330):1237–1242, 1997.

[2] Y-H Zhao, John F Bingert, X-Z Liao, B-Z Cui, Ke Han, Alla V Sergueeva, Amiya K Mukherjee, Ruslan Z Valiev, Terence G Langdon, and Yuntian T Zhu. Simultaneously increasing the ductility and strength of ultra-fine-grained pure copper. *Advanced Materials*, 18(22):2949–2953, 2006.

[3] Ke Lu, Lei Lu, and S Suresh. Strengthening materials by engineering coherent internal boundaries at the nanoscale. *science*, 324(5925):349–352, 2009.

[4] Güven Kurtuldu, Philippe Jarry, and Michel Rappaz. Influence of cr on the nucleation of primary al and formation of twinned dendrites in al–zn–cr alloys: Can icosahedral solid clusters play a role? *Acta Materialia*, 61(19):7098–7108, 2013.

[5] Güven Kurtuldu, Alberto Sicco, and Michel Rappaz. Icosahedral quasicrystal-enhanced nucleation of the fcc phase in liquid gold alloys. *Acta Materialia*, 70:240–248, 2014.

[6] Güven Kurtuldu and Michel Rappaz. Probability of twin boundary formation associated with the nucleation of equiaxed grains on icosahedral quasicrystal templates. In *IOP Conference Series: Materials Science and Engineering*, volume 84, page 012012. IOP Publishing, 2015.

[7] S Henry, M Rappaz, and P Jarry. $\langle 110 \rangle$ dendrite growth in aluminum feathery grains. *Metallurgical and Materials Transactions A*, 29(11):2807–2817, 1998.

[8] MA Salgado-Ordorica and M Rappaz. Twinned dendrite growth in binary aluminum alloys. *Acta Materialia*, 56(19):5708–5718, 2008.

[9] Akihisa Inoue. Stabilization of metallic supercooled liquid and bulk amorphous alloys. *Acta materialia*, 48(1):279–306, 2000.

[10] John H Perepezko and Rainer J Hebert. Amorphous aluminum alloys-synthesis and stability. *JOM*, 54(3):34–39, 2002.

[11] AL Greer, KL Rutherford, and IM Hutchings. Wear resistance of amorphous alloys and related materials. *Int. Mater. Rev.*, 47(2):87–112, 2002.

[12] MF Ashby and AL Greer. Metallic glasses as structural materials. *Scripta Materialia*, 54(3):321–326, 2006.

[13] Christopher A Schuh, Todd C Hufnagel, and Upadrasta Ramamurty. Mechanical behavior of amorphous alloys. *Acta Mater.*, 55(12):4067–4109, 2007.

[14] Golden Kumar, Hong X Tang, and Jan Schroers. Nanomoulding with amorphous metals. *Nature*, 457(7231):868–872, 2009.

[15] A Inoue and A Takeuchi. Recent development and application products of bulk glassy alloys. *Acta Mater.*, 59(6):2243–2267, 2011.

[16] W Klement, RH Willens, and POL Duwez. Non-crystalline structure in solidified gold–silicon alloys. *Nature*, 187:869–870, 1960.

[17] MH Cohen and D Turnbull. Composition requirements for glass formation in metallic and ionic systems. *Nature*, 189(4759):131–132, 1961.

[18] YQ Cheng, E Ma, and HW Sheng. Alloying strongly influences the structure, dynamics, and glass forming ability of metallic supercooled liquids. *Appl. Phys. Lett.*, 93(11):111913, 2008.

[19] Michael I Ojovan and William Bill E Lee. Connectivity and glass transition in disordered oxide systems. *Journal of Non-Crystalline Solids*, 356(44):2534–2540, 2010.

[20] GB Bokas, L Zhao, JH Perepezko, and I Szlufarska. On the role of Sm in solidification of Al-Sm metallic glasses. *Scr. Mater.*, 124:99–102, 2016.

[21] ON Senkov and DB Miracle. Effect of the atomic size distribution on glass forming ability of amorphous metallic alloys. *Mater. Res. Bull.*, 36(12):2183–2198, 2001.

[22] RO Suzuki, Y Komatsu, KF Kobayashi, and PH Shingu. Formation and crystallization of Al-Fe-Si amorphous alloys. *J. Mater. Sci.*, 18(4):1195–1201, 1983.

[23] ZP Lu and CT Liu. A new glass-forming ability criterion for bulk metallic glasses. *Acta materialia*, 50(13):3501–3512, 2002.

[24] ZP Lu and CT Liu. Glass formation criterion for various glass-forming systems. *Physical review letters*, 91(11):115505, 2003.

[25] Y He, SJ Poon, and GJ Shiflet. Synthesis and properties of metallic glasses that contain aluminum. *Science*, 241(4873):1640, 1988.

[26] JC Foley, DR Allen, and JH Perepezko. Analysis of nanocrystal development in Al-Y-Fe and Al-Sm glasses. *Scr. Mater.*, 35(5):655–660, 1996.

[27] G Wilde, H Sieber, and JH Perepezko. Glass formation versus nanocrystallization in an Al92Sm8 alloy. *Scr. Mater.*, 40(7):779–783, 1999.

[28] H Chen, Y He, GJ Shiflet, and SJ Poon. Mechanical properties of partially crystallized aluminum based metallic glasses. *Scr. Metall. et Mater.*, 25(6):1421–1424, 1991.

[29] Yeong-Hwan Kim, Akihisa Inoue, and Tsuyoshi Masumoto. Increase in mechanical strength of Al–Y–Ni amorphous alloys by dispersion of nanoscale fcc-Al particles. *Mater. Trans., JIM*, 32(4):331–338, 1991.

[30] Yeong-Hwan Kim, Akihisa Inoue, and Tsuyoshi Masumoto. Ultrahigh mechanical strengths of $Al_{88}Y_2Ni_{10-x}M_x$ (M= Mn, Fe or Co) amorphous alloys containing nanoscale fcc-Al particles. *Mater. Trans., JIM*, 32(7):599–608, 1991.

[31] DR Allen, JC Foley, and JH Perepezko. Nanocrystal development during primary crystallization of amorphous alloys. *Acta Mater.*, 46(2):431–440, 1998.

Chapter 2 : Methods

In this chapter, we introduce the multi-scale simulation methods applied in this thesis. Specifically, in the first two sections, phase field model and crystal plasticity finite element (CPFE) are introduced, which are coupled in Chap. 3 to study the plasticity driven grain boundary (GB) migration. In the last section, molecular dynamics (MD) method is discussed, which we apply to study the nucleation kinetics in Al-Sm MGs in Chap. 4 and multiple twinning in Al alloys in Chap. 5.

2.1 Phase field method

2.1.1 Phase field description of microstructure

The phase field method has become an important and extremely versatile technique for simulating microstructural evolution at the mesoscale. In the phase field method, microstucture is represented numerically with a set of so-called phase field variables, including conserved and non-conserved ones. In particular, conserved variables are typically related to the local composition, or volume fraction, while the non-conserved variables usually contain information on the local (crystal) structure and orientation, like order parameters. The set of phase-field variables must capture the important physics behind the phase transformation or coarsening process. The key merit of phase field method is the diffuse interface description of microstructure. As Figure 2.1 shows, diffuse interface model allows properties (structure, orientation and composition) to evolve continuously across the interface, as opposed to the sharp interface model. Under the diffuse-interface description, the total system free energy F is consisted of bulk (chemical) free energy F_{bulk}, interfacial energy F_{int}, and other contributions F_{oth} (e.g., deformation energy, elec-

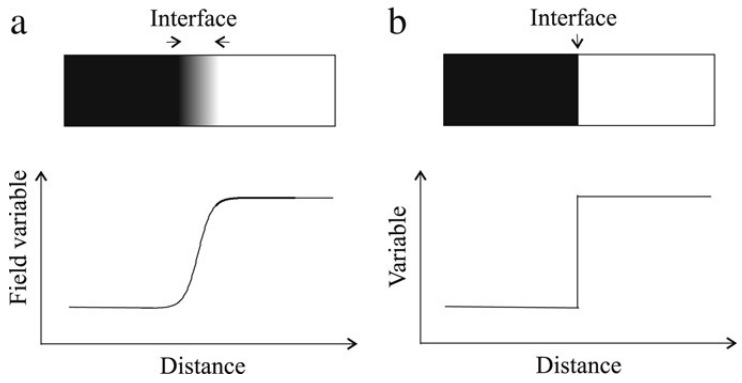

Fig. 2.1: Schematic representation of (a) diffuse and (b) sharp interface models [2].

tric energy, magnetic energy, etc.) [1]

$$F = F_{\text{bulk}} + F_{\text{int}} + F_{\text{oth}}. \tag{2.1}$$

The microstructural evolution, represented as the interface kinetics, is driven by the reduction of the total free energy F. The interface kinetics is modeled by evolving the phase field variables temporally according to a set of partial differential equations (PDEs), which are derived based on general thermodynamic and kinetic principles [2]. Specifically, the conserved variables are evolved according to the Cahn-Hilliard equation, i.e., [3]

$$\frac{\partial c_i}{\partial t} = \nabla \cdot M \nabla \frac{\partial F}{\partial c_i}, \tag{2.2}$$

where M is the species mobility. Non-conserved variables are evolved following the Allen-Cahn equatioin [4],

$$\frac{\partial \eta_i}{\partial t} = -L \frac{\partial F}{\partial \eta_i}, \tag{2.3}$$

where L is the order parameter mobility.

Phase field method makes it possible to study the evolution of arbitrary complex phase/grain morphologies without the need to track the interface explicitly, which is the main advantage of this model over the sharp interface ones such as the Monte Carlo

Potts model. Therefore, this method has been extensively used to study many physical problems in materials science, such as solidification modeling [5, 6], solid-state phase transformations [7–10], coarsening, and grain growth [11–14].

2.1.2 Phase field grain growth model

We apply the grain growth model proposed by Chen [11]. In this model, each grain is represented using one of the order parameters $\{\eta_i\}$, which take on the value of 1 within grains they represent, and change gradually to 0 across the boundaries. According to the diffuse interface theory [15], the total system free energy is usually expressed in the form of an integral:

$$F = \int_V \left[f_0(\eta_1, \eta_2, ..., \eta_p) + \sum_i^p \frac{\kappa_i}{2} (\nabla \eta_i)^2 + \psi \right] \mathrm{d}V, \tag{2.4}$$

where V is the system volume, $f_0(\eta_1, \eta_2, ..., \eta_p)$ is the bulk chemical free energy density, κ_i is the gradient energy coefficient. ψ is the other type of free energy density (such as deformation energy which will be discussed in the next chapter, etc.). Following the proposal by Moelans *et al.* [16], we choose the chemical free energy density $f_0(\eta_1, \eta_2, ..., \eta_p)$ to be represented by a polynomial

$$f_0(\eta_1, \eta_2, ..., \eta_p) = \mu \left[\sum_{i=1}^{p} (-\frac{1}{2}\eta_i^2 + \frac{1}{4}\eta_i^4) + \gamma \sum_{i=1}^{p} \sum_{j \neq i} \eta_i^2 \cdot \eta_j^2 + \frac{1}{4} \right], \tag{2.5}$$

where μ and γ are parameters associated with GB properties. By plugging in Eqs. (2.4) and (2.5) into Eq. (2.3), the Allen-Cahn equatioin is reduced to

$$\frac{\partial \eta_i}{\partial t} = -L \left[\mu \left(\eta_i^3 - \eta_i + 2\gamma \eta_i \sum_{j \neq i} \eta_j^2 \right) - \nabla \cdot \kappa_i \nabla \eta_i + \frac{\partial \psi}{\partial \eta_i} \right]. \tag{2.6}$$

The model parameters μ, γ, κ_i and L are selected such that they can reproduce the desired GB energy σ_{GB} and GB mobility m_{GB}. Here the values of these parameters are

determined according to the following relations proposed by Moelans *et al.* [16]

$$\gamma = 1.5, \tag{2.7a}$$

$$\kappa_i \approx \frac{3}{4}\sigma_{\mathrm{GB}} l_{\mathrm{GB}}, \tag{2.7b}$$

$$L \approx \frac{4}{3}\frac{m_{\mathrm{GB}}}{l_{\mathrm{GB}}}, \tag{2.7c}$$

$$\mu \approx \frac{3}{4}\frac{1}{f_{0,\mathrm{saddle}}(\gamma)}\frac{\sigma_{\mathrm{GB}}}{l_{\mathrm{GB}}}, \tag{2.7d}$$

where l_{GB} is the diffuse GB width and $f_{0,\mathrm{saddle}}(\gamma)$ is the chemical free energy of the system at the saddle point. Details of the parameterization method are described in Ref. [16].

If the grain growth is driven only by reducing the total interfacial free energy ($\frac{\partial \psi}{\partial \eta_i} = 0$ in Eq. (2.6)), the average local curvature of GB becomes the sole driving force for GB migration, namely, $P = \sigma_{\mathrm{GB}}(\gamma_1 + \gamma_2)$, where P is the driving force, γ_1 and γ_2 are the average local curvatures along two perpendicular tangents of the GB surface. The grain growth process is shown to obey the empirical kinetics law: $\overline{R}_t^m - \overline{R}_0^m = kt$, where k is kinetics coefficient, $\overline{R}_0$ and $\overline{R}_t$ are average equivalent grain radii in initial state and at time t, respectively, and m is called grain growth exponent. For normal grain growth without impurity drag effect or system anisotropy, the value of m equals 2 theoretically.

Figure 2.2 shows snapshots of a 2D grain growth simulation of Cu with isotropic GB properties ($m_{\mathrm{GB}} = 3.2 \times 10^{-9}\ \mathrm{m}^4/(\mathrm{J}\cdot\mathrm{s})$, $\sigma_{\mathrm{GB}} = 0.708\ \mathrm{J/m}^2$) in a 2 μm $\times$ 2 μm system. The initial structure was obtained from the Voronoi tessellation and contained 1000 grains. Figure 2.3 shows the evolution of average grain size $\overline{R}$ with time t. The data were fitted to the equation $t = A\overline{R}^m + B$ by a multi-parameter non-linear least-square fitting routine to extract the growth exponent m. The data in the initial 300 ns were removed from the fitting to eliminate the effect of the initial structure relaxation. The normal grain growth exponent obtained is shown to be almost 2. This suggests that phase field method is

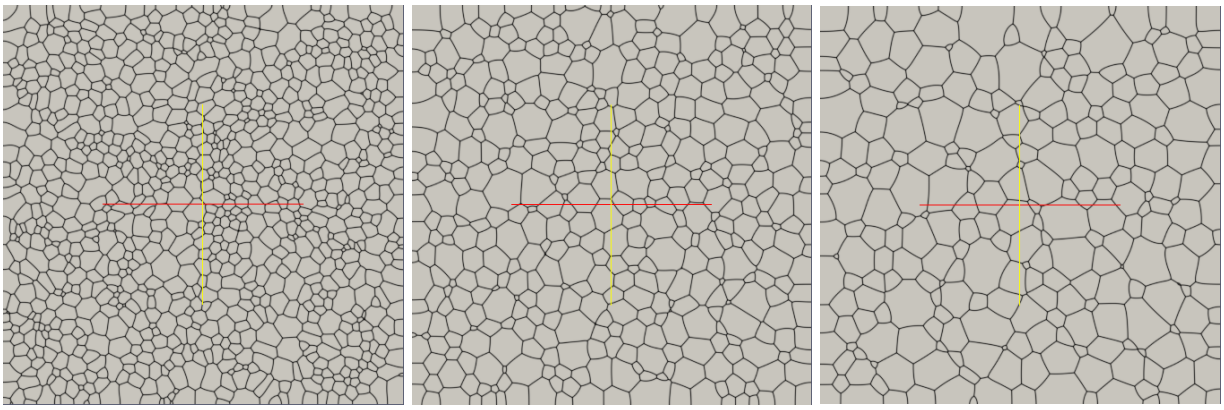

(a) t = 0 μs (b) t = 2.2 μs (c) t = 4.7 μs

Fig. 2.2: Snapshots of curvature driven grain growth in a 2 μm $\times$ 2 μm system, with (a) initial structure, (b) and (c) structures after 2.2 μs and 4.7 μs, respectively.

an effective and accurate approach to model the meso-scale grain growth in metals and alloys.

The aforementioned phase field model can be coupled with other physics model to study more complicated grain growth phenomena. For instance, one can couple linear elasticity with the above phase field model to study the elasticity driven grain growth. Following the constitutive law ($\boldsymbol{\sigma} = \mathbf{C} \cdot \boldsymbol{\epsilon}$) in the linear elasticity theory, the elastic energy density can be written as $\psi = \frac{1}{2} C_{ijkl} \cdot \epsilon_{ij} \epsilon_{kl}$. Here, C_{ijkl} is the weight averaged elasticity tensor among multiple grains, and ϵ_{ij} and ϵ_{kl} are the strain components. The derivative $\frac{\partial \psi}{\partial \eta_i}$ can therefore be derived to be

$$\frac{\partial \psi}{\partial \eta_i} = \frac{\sum h(\eta_i) \psi_i}{\sum h(\eta_i)}. \tag{2.8}$$

Plugging in Eq. (2.8) into Eq. (2.6), one can simulate the effect of elasticity on grain growth.

Fig. 2.4 shows an example of a 2D elastic grain growth simulation in a 1 μm $\times$ 1 μm system. The initial structure was obtained from the Voronoi tessellation, and grain

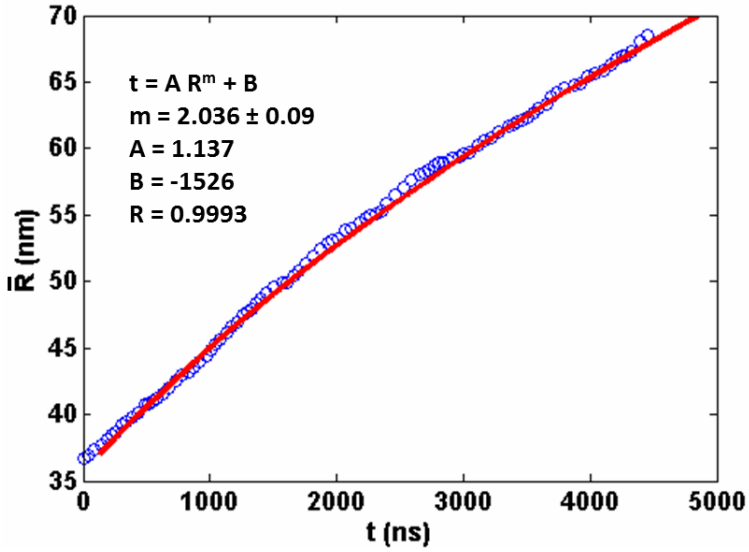

Fig. 2.3: The time dependence of average grain radius in the 2 μm $\times$ 2 μm system. Data are fitted into equation $t = A\overline{R}^m + B$.

orientations were randomly assigned to each grain in the beginning of the simulation. The Dirichlet boundary condition (BC), a displacement d_x of 20 nm, was applied on the right boundary along [100] direction. GB migration is driven by both the GB curvature and the elastic energy. One can see from Fig. 2.4 that, $\langle 100 \rangle$ direction becomes the preferred orientation as grain growth proceeds. This is because the grains near $\langle 100 \rangle$ orientation are "soft" grains with respect to the loading in this case, which contain the smaller elastic energy density and grow at the expense of the "hard" grains.

2.2 *Crystal plasticity finite element*

The crystal plasticity finite element (CPFE) method has emerged as a powerful tool to model heterogeneous deformation and stress at the microstructure level [17, 18]. In CPFE method, a single crystal plasticity model is employed at each material point in a finite element (FE) simulation. As shown in Fig. 2.5, the deformation gradient **F** is decomposed into the elastic part (lattice strain and rotation) $\mathbf{F}^e$ and the plastic part (dislocation slip)

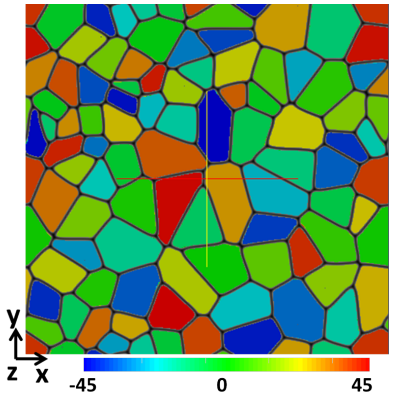

(a) t = 0 ns

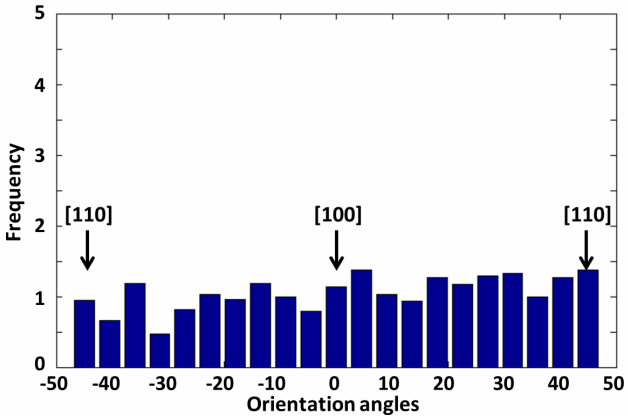

(b) t = 0 ns

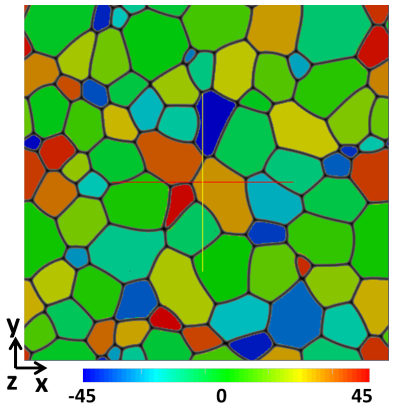

(c) t = 600 ns

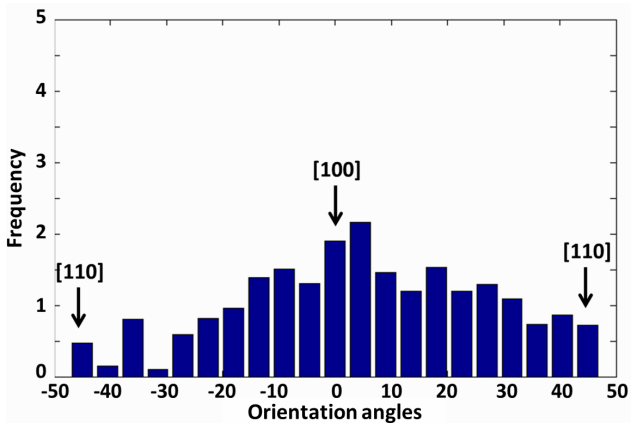

(d) t = 600 ns

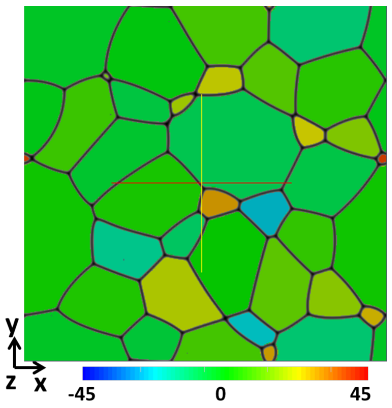

(e) t = 1500 ns

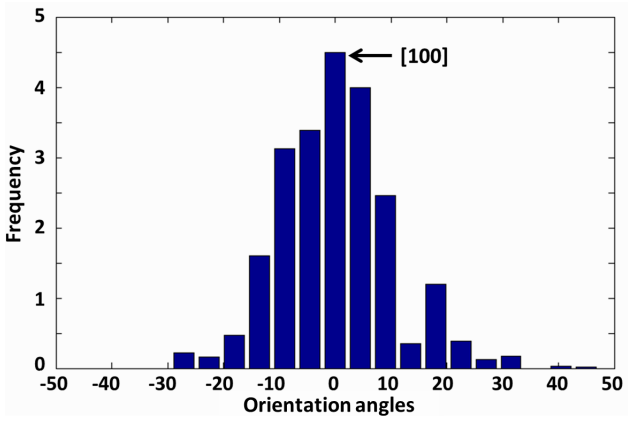

(f) t = 1500 ns

Fig. 2.4: Snapshots of elasticity driven grain growth of Cu in a 1 μm $\times$ 1 μm system of 90 grains initially, subjected to a Dirichlet BC $d_x = 20$ nm on the right boundary. (a), (c) and (e) are the initial Voronoi polyhedra, structures after 600 ns and 1500 ns, respectively; (b), (d) and (f) are the corresponding grain occurrence frequencies along different orientations. x, y and z represent [100], [010] and [001] crystallographic directions, respectively.

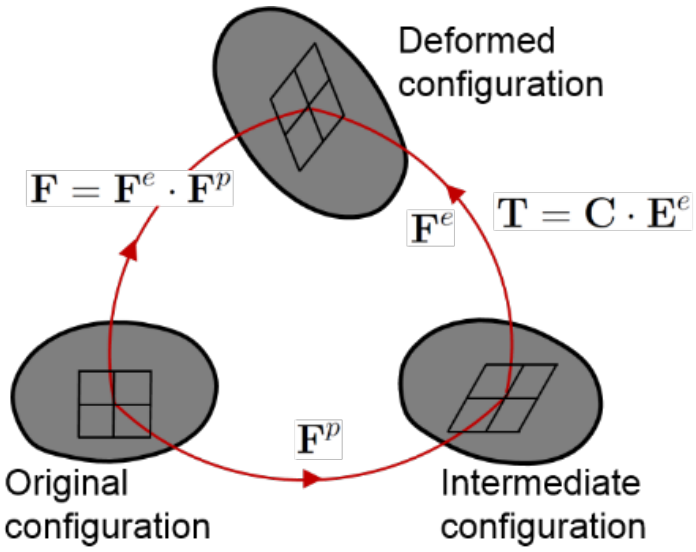

Fig. 2.5: Multiplicative decomposition of deformation gradient.

$\mathbf{F}^{\mathrm{p}}$ according to the following equation

$$\mathbf{F} = \mathbf{F}^{\mathrm{e}}\,\mathbf{F}^{\mathrm{p}}. \tag{2.9}$$

The model assumes dislocation slip to be the sole mechanism for plastic deformation [19], and therefore, the evolution of velocity gradient is given by

$$\dot{\mathbf{F}}^{\mathrm{p}}\mathbf{F}^{\mathrm{p}\,-1} = \sum_{\alpha=1}^{n} \dot{\gamma}^{\alpha}\mathbf{m}^{\alpha} \otimes \mathbf{n}^{\alpha}, \tag{2.10}$$

where $\mathbf{m}^{\alpha}$, $\mathbf{n}^{\alpha}$ and $\dot{\gamma}^{\alpha}$ are the slip direction, slip plane normal, and plastic shear rate on the α-th slip system, respectively. The Schmid tensor is defined as $\mathbf{S}^{\alpha} \equiv \mathbf{m}^{\alpha} \otimes \mathbf{n}^{\alpha}$. The shear stress, τ^{α}, resolved on each slip system activates the slip activity following the flow rule [20]

$$\dot{\gamma}^{\alpha} = \dot{\gamma}_0 \left| \frac{\tau^{\alpha}}{s^{\alpha}} \right|^{1/m} \mathrm{sgn}(\tau^{\alpha}), \tag{2.11}$$

where $\dot{\gamma}_0$ is the reference slip rate, s^{α} is the slip system resistance, m is the strain rate sensitivity, and sgn() is a sign function that takes values of ± 1. When the α-th slip

system undergoes shear, it increases its own slip resistance s^α (a phenomenon known as self hardening), as well as the resistances of all the other slip systems s^β ($\beta \neq \alpha$) (known as latent hardening). Therefore, the material is work hardened through both self and latent hardening mechanisms and the rate of change of slip resistance can be described as [21]

$$\dot{s}^\alpha = \sum_\beta h^{\alpha\beta} |\dot{\gamma}^\beta|. \tag{2.12}$$

In the above equation $h^{\alpha\beta}$ is the hardening matrix, which takes the form [22]

$$h^{\alpha\beta} = q^{\alpha\beta} h_0 \left| 1 - \frac{s^\beta}{s_s} \right|^c \operatorname{sgn}\left(1 - \frac{s^\beta}{s_s}\right), \tag{2.13}$$

where s_s is the saturated slip system resistance. The prefactor h_0 and the exponent c are constants and $q^{\alpha\beta}$ is a measure for self ($\alpha = \beta$) and latent ($\alpha \neq \beta$) hardening. $q^{\alpha\beta}$ usually takes the value of 1.0 for coplanar slip system and 1.4 otherwise, based on the fact that material is usually work hardened more effectively if multiple slip systems are activated as compared to activation of a single slip system [22]. Equation (2.13) phenomenologically captures the micromechanical interaction among different slip systems.

In the multiplicative crystal plasticity model, the stress and strain tensors are related in the intermediate configuration, where elastic strain is released but plastic strain is retained. The constitutive law takes the following form

$$\mathbf{T} = \mathbf{C} \cdot \mathbf{E}^{\mathrm{e}}, \tag{2.14}$$

where $\mathbf{C}$ is the elasticity tensor. $\mathbf{T}$ is the 2$^{\mathrm{nd}}$ Piola-Kirchhoff stress and it is related to the Cauchy stress $\boldsymbol{\sigma}$ through $\mathbf{T} \equiv (\det \mathbf{F}^{\mathrm{e}}) \mathbf{F}^{\mathrm{e}-1} \boldsymbol{\sigma} \mathbf{F}^{\mathrm{e}-\mathrm{T}}$. $\mathbf{E}^{\mathrm{e}}$ is the Lagrange elastic strain and is defined as $\mathbf{E}^{\mathrm{e}} \equiv \frac{1}{2} \mathbf{F}^{\mathrm{e}\mathrm{T}} \mathbf{F}^{\mathrm{e}} - \mathbf{I}$, where $\mathbf{I}$ is the identity tensor.

Given the above plasticity framework, the governing equations (strong form) associated with quasistatic solid mechanics on the domain Ω and boundary $\Gamma = \Gamma_t \cup \Gamma_g$ can

be expressed as

$$\nabla \cdot \boldsymbol{\sigma} + \vec{b} = \vec{0} \quad \text{in } \Omega, \tag{2.15a}$$

$$\vec{u} = \vec{g} \quad \text{on } \Gamma_g, \tag{2.15b}$$

$$\boldsymbol{\sigma} \cdot \vec{n} = \vec{\imath} \quad \text{on } \Gamma_\imath, \tag{2.15c}$$

where $\vec{u}$ is the displacement vector, $\vec{b}$ is the body force, $\vec{n}$ is the unit normal to the boundary, $\vec{g}$ is the prescribed displacement on the boundary and $\vec{\imath}$ is the prescribed traction on the boundary.

In contrast to J_2 plasticity model which applies the von Mises yield criterion, crystal plasticity model not only does not require an explicit yield criterion, it also captures the plasticity anisotropy since the material can only flow along slip systems. CPFE method has been applied to a large range of materials and crystal structures [23, 24].

2.3 *Molecular dynamics*

MD technique, developed by Fermi *et al.* [25], Alder *et al.* [26] and Rahman *et al.* [27], is a classical computer simulation method used to study the atomic-scale dynamic evolution of a many-body system. MD method models the motion of classical particles (e.g., atoms or molecules) by solving Newton's equations of motion:

$$m_i \frac{d^2 \vec{r}_i}{dt^2} = \sum_{j \neq i} \vec{F}_{ij} + \vec{F}_i^{\text{e}}, \tag{2.16}$$

where m_i and r_i are the mass and position, respectively, of atom i, $\vec{F}_{ij}$ is the interatomic force applied by atom j on atom i, and $\vec{F}_i^{\text{e}}$ is the external force applied on atom i. The calculation of $\vec{F}_{ij}$ will be discussed later in this section. Eq. 2.16 is usually integrated numerically over a small timestep Δt, the size of which for atomic system is of the order of 10^{-15} s (1 fs). The Velocity-Verlet algorithm is one of the most commonly used

integration schema and it implements the following equations:

$$\vec{r}_i(t+\Delta t) = \vec{r}_i(t) + \vec{v}_i(t)\Delta t + \frac{\vec{F}_i(t)}{2m_i}(\Delta t)^2, \tag{2.17a}$$

$$\vec{v}_i(t+\Delta t) = \vec{v}_i(t) + \frac{\vec{F}_i(t) + \vec{F}_i(t+\Delta t)}{2m_i}\Delta t, \tag{2.17b}$$

where $\vec{v}_i$ is the velocity of atom i and $\vec{F}_i = \sum_{j\neq i}\vec{F}_{ij} + \vec{F}_i^{\mathrm{e}}$ represents the total force acting on atom i.

A simplified schematic representation of the standard MD simulation process is shown in Fig. 2.6. MD simulations can be valuable in providing insights into statistical problems as no *a priori* assumptions are required in MD method. The best physical fidelity and accuracy that MD simulations can achieve depend largely on the calculation of force fields. In classical MD simulations, the interatomic force $\vec{F}_{ij}$ is usually calculated from the gradient of the interatomic potential energy:

$$\vec{F}_{ij} = -\nabla U_{ij}(\vec{r}_{ij}), \tag{2.18}$$

where $U_{ij}(\vec{r}_{ij})$ is the interatomic potential energy between atom i and atom j. Development of force fields is beyond the scope of this thesis.

The most popular types of potentials employed to simulate phase transformations in metallic systems are Finnis-Sinclair (FS) [28] and embedded atom method (EAM) [29] potentials. As many-body potentials, FS and EAM potentials are comparable to pair potentials with respect to computational efficiency, but outweigh them in the reproduction of important properties. FS type potential has the following functional form

$$U = \sum_{i=1}^{N-1}\sum_{j=i+1}^{N}\phi_{t_i t_j}(r_{ij}) + \sum_{i=1}^{N}\Phi_{t_i}(\rho_i), \tag{2.19}$$

where t_i represents species of atom i, N is the total number of atoms, r_{ij} is the distance

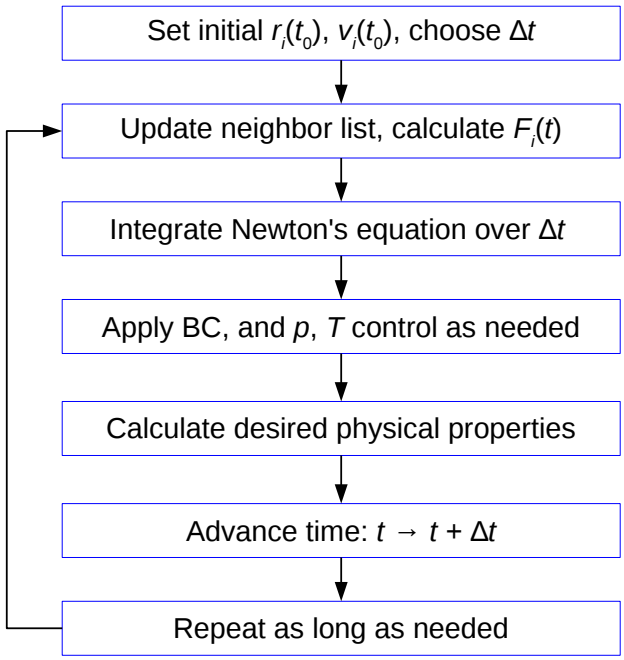

Fig. 2.6: Simplified schematic representation of MD simulation process.

between atom i and j, $\phi_{t_i t_j}(r_{ij})$ is the pairwise interaction energy, $\Phi_{t_i}(\rho_i)$ is the embedding energy function, $\rho_i = \sum_j \Psi_{t_i t_j}(r_{ij})$ is the electronic density, and $\Psi_{t_i t_j}(r_{ij})$ are density functions. In this work, the FS potential was used to study the nucleation kinetics of Al-Sm MGs (Chap. 4) and multiple twinning in Al alloys (Chap. 5).

In the EAM potential description, the potential energy of atom i is given by

$$E_i = \Phi_{t_i}\left(\sum_{i \neq j} \rho_{t_j}(r_{ij})\right) + \frac{1}{2}\sum_{i \neq j} \phi_{t_i t_j}(r_{ij}), \tag{2.20}$$

where t_i represents species of atom i, r_{ij} is the distance between atoms i and j, ρ_{t_j} is the contribution to the electron charge density from atom j at the position of atom i, Φ_{t_i} is the embedding function energy that is required to place atom i into the electron cloud, and $\phi_{t_i t_j}$ is a pairwise potential function. In our studies, the EAM potential was applied for simulating multiple twinning in Al alloys (see Chap. 5 for more details).

In our MD simulations, the common neighbor analysis (CNA) [30, 31] was used extensively to conduct the structural analysis. In this method, the CNA pattern of each atom is first calculated from the topology of its nearest neighboring atoms, then compared to the reference pattern and finally classified into face-centered cubic (FCC), body-centered cubic (BCC), hexagonal close packed (HCP) or other structures. The nearest neighbor list is obtained by comparing the distance of two atoms with the predefined cutoff r_c, which is often set to be the average of the first and the second nearest neighboring atoms in the perfect crystal structures. Specifically,

$$r_c^{\text{fcc}} = \frac{1}{2}\left(\frac{\sqrt{2}}{2}+1\right)a, \tag{2.21a}$$

$$r_c^{\text{bcc}} = \frac{1}{2}(\sqrt{2}+1)a, \tag{2.21b}$$

$$r_c^{\text{hcp}} = \frac{1}{2}\left(\sqrt{\frac{4+2x^2}{3}}+1\right)a. \tag{2.21c}$$

Here, a is the lattice parameter, $x = (c/a)/1.633$, where c is the unit cell height in HCP structure. More details of CNA method can be found in Ref. [30].

In summary, in this chapter we briefly discussed the different computational methods used in our studies. For phase field and crystal plasticity models, we used the MOOSE/MARMOT simulation package to conduct all the simulations, where we also implemented the developed framework coupling phase field and crystal plasticity theory. The details of the coupling approach and the FE technique used for solving PDEs will be discussed in Chap. 3. For MD simulations, the LAMMPS simulation package is used throughout this thesis, and the simulation details will be presented in Chap. 4 for the study of nucleation kinetics in MGs and in Chap. 5 for multiple twinning studies in Al alloys.

References

[1] Long-Qing Chen. Phase-field models for microstructure evolution. *Annual review of materials research*, 32(1):113–140, 2002.

[2] Nele Moelans, Bart Blanpain, and Patrick Wollants. An introduction to phase-field modeling of microstructure evolution. *Calphad*, 32(2):268–294, 2008.

[3] John W Cahn. On spinodal decomposition. *Acta Metallurgica*, 9(9):795–801, 1961.

[4] JW Cahn and SM Allen. A microscopic theory for domain wall motion and its experimental verification in Fe-Al alloy domain growth kinetics. *Le Journal de Physique Colloques*, 38(C7):C7–51, 1977.

[5] Ryo Kobayashi. Modeling and numerical simulations of dendritic crystal growth. *Physica D: Nonlinear Phenomena*, 63(34):410 – 423, 1993.

[6] WJ Boettinger, JA Warren, C Beckermann, and A Karma. Phase-field simulation of solidification 1. *Annual review of materials research*, 32(1):163–194, 2002.

[7] Hiraku Nishimori and Akira Onuki. Pattern formation in phase-separating alloys with cubic symmetry. *Phys. Rev. B*, 42:980–983, Jul 1990.

[8] Y. Wang, D. Banerjee, C.C. Su, and A.G. Khachaturyan. Field kinetic model and computer simulation of precipitation of {L12} ordered intermetallics from f.c.c. solid solution. *Acta Materialia*, 46(9):2983 – 3001, 1998.

[9] DY Li and LQ Chen. Shape evolution and splitting of coherent particles under applied stresses. *Acta materialia*, 47(1):247–257, 1998.

[10] Danan Fan and Long-Qing Chen. Computer simulation of twin formation during the displacive c t phase transformation in the zirconia-yttria system. *Journal of the American Ceramic Society*, 78(3):769–773, 1995.

[11] Long-Qing Chen and Wei Yang. Computer simulation of the domain dynamics of a quenched system with a large number of nonconserved order parameters: The grain-growth kinetics. *Physical Review B*, 50(21):15752, 1994.

[12] Danan Fan and L-Q Chen. Computer simulation of grain growth using a continuum field model. *Acta Materialia*, 45(2):611–622, 1997.

[13] I Steinbach, F Pezzolla, B Nestler, M Seeßelberg, R Prieler, GJ Schmitz, and JLL Rezende. A phase field concept for multiphase systems. *Physica D: Nonlinear Phenomena*, 94(3):135–147, 1996.

[14] Harald Garcke, Britta Nestler, and Barbara Stoth. A multiphase field concept: numerical simulations of moving phase boundaries and multiple junctions. *SIAM Journal on Applied Mathematics*, 60(1):295–315, 1999.

[15] John W Cahn and John E Hilliard. Free energy of a nonuniform system. I. interfacial free energy. *The Journal of Chemical Physics*, 28(2):258–267, 1958.

[16] Nele Moelans, Bart Blanpain, and Patrick Wollants. Quantitative analysis of grain boundary properties in a generalized phase field model for grain growth in anisotropic systems. *Physical Review B*, 78(2):024113, 2008.

[17] L Anand and M Kothari. A computational procedure for rate-independent crystal plasticity. *Journal of the Mechanics and Physics of Solids*, 44(4):525–558, 1996.

[18] Franz Roters, Philip Eisenlohr, Thomas R Bieler, and Dierk Raabe. *Crystal Plasticity Finite Element Methods: In Materials Science and Engineering*. John Wiley & Sons, 2010.

[19] Vlado A Lubarda. *Elastoplasticity theory*. CRC press, 2010.

[20] Robert J Asaro and A Needleman. Overview no. 42 Texture development and strain hardening in rate dependent polycrystals. *Acta Metallurgica*, 33(6):923–953, 1985.

[21] Manish Kothari. *Rate independent crystal plasticity*. PhD thesis, Massachusetts Institute of Technology, 1995.

[22] F Roters, P Eisenlohr, L Hantcherli, DD Tjahjanto, TR Bieler, and D Raabe. Overview of constitutive laws, kinematics, homogenization and multiscale methods in crystal plasticity finite-element modeling: Theory, experiments, applications. *Acta Materialia*, 58(4):1152–1211, 2010.

[23] M Kothari and L Anand. Elasto-viscoplastic constitutive equations for polycrystalline metals: application to tantalum. *Journal of the Mechanics and Physics of Solids*, 46(1):5169–6783, 1998.

[24] A Staroselsky and L Anand. A constitutive model for hcp materials deforming by slip and twinning: application to magnesium alloy az31b. *International journal of Plasticity*, 19(10):1843–1864, 2003.

[25] E Fermi, J Pasta, S Ulam, and M Tsingou. Los alamos report no. *LA-1940*, page 978, 1955.

[26] Berni J Alder and T E Wainwright. Studies in molecular dynamics. i. general method. *The Journal of Chemical Physics*, 31(2):459–466, 1959.

[27] A Rahman. Correlations in the motion of atoms in liquid argon. *Physical Review*, 136(2A):A405, 1964.

[28] MW Finnis and JE Sinclair. A simple empirical n-body potential for transition metals. *Philosophical Magazine A*, 50(1):45–55, 1984.

[29] MS Daw and MI Baskes. Embedded-atom-method functions for the fcc metals cu, ag, au, ni, pd, pt, and their alloys. *Phys. Rev. B*, 29:6443, 1984.

[30] Daniel Faken and Hannes Jónsson. Systematic analysis of local atomic structure combined with 3d computer graphics. *Computational Materials Science*, 2(2):279–286, 1994.

[31] Helio Tsuzuki, Paulo S Branicio, and José P Rino. Structural characterization of deformed crystals by analysis of common atomic neighborhood. *Computer physics communications*, 177(6):518–523, 2007.

Chapter 3 : Modeling the Plastic Driving Force for Grain Boundary Migration

Dislocations stored in heavily deformed materials play an important role in driving microstructural evolution. In this chapter, we developed a full coupling model that concurrently couples the phase field method with CPFE analysis to study GB migration under a plastic driving force [1]. In our model, we describe multiple active grains in GB regions with crystal plasticity theory and use a weighted sum of their properties (i.e., stress and elastic/plastic potentials, etc.) to evaluate the plastic driving force for GB migration. The model can qualitatively capture the absorption of dislocations by mobile GBs through re-initialization of slip system resistances of newly active grains. A FE based preconditioned Jacobian-free Newton-Krylov approach is used to simultaneously solve all the nonlinear partial differential equations for the coupled physics models. Determining model parameters and validation of the model are accomplished by simulating copper bicrystals and comparing the results to available experiments. This model provides a useful tool for effectively simulating GB migration in metals undergoing large plastic deformation. All the developments have been implemented in the MOOSE/MARMOT simulation package.

3.1 Introduction

Mechanical properties of polycrystalline alloys depend on the details of the microstructure, e.g., grain sizes and orientations, GB networks, dislocation densities. Not only the grain size affects the mechanical properties of materials, but mechanical deformations can also alter the grain size. Both deformation-induced grain refinement [2–5] and

grain coarsening [6, 7] have been reported in experimental and computational studies. Therefore, understanding and predicting how GBs migrate in the presence of plastic deformation is important to the development of materials with optimized mechanical properties.

Computer simulations make it possible to track the evolution of stresses and strains as well as microstructural evolution *in operando* (i.e., during deformation) and they allow one to isolate different effects in the interplay between mechanical deformation and microstructural evolution. Therefore simulations provide a useful complementary approach to experiments.

Different modeling techniques have been used to study plastic deformation behaviors of materials. Atomistic simulations, such as those based on the MD technique, are able to capture the effect of plastic deformation on GB migration and sliding [8, 9]. However, this method cannot simulate microstructural changes in materials on typical experimental time scales. For instance, the deformation rate for standard MD simulations ($10^8 - 10^{10}$ s^{-1}) is much higher than in experiments ($10^{-3} - 10^{-4}$ s^{-1}). Modeling of deformation on typical experimental time scales is often accomplished by the use of FE analysis, but in this method it can be challenging to efficiently track interface kinetics. A useful and highly versatile technique for modeling evolution of a microstructure, and more generally of interfaces, is the phase field method. This method can be coupled with a model of plastic deformation in order to simulate the effect of plastic behavior on microstructural evolution. A few approaches towards this goal have been reported so far, and they are summarized below.

A two-step coupling approach, proposed by Takaki *et al.* [10, 11], Güvenç *et al.* [12] and Vondrous *et al.* [13], describes the deformation process and microstructural evolution with separate models that are coupled sequentially. This approach has been used to model static recrystallization process during annealing, where the stored energy of deformation is the main driving force for microstructural evolution. Specifically, the de-

formation prior to annealing is simulated by the FE method based on crystal plasticity theory. Subsequently, the deformed structure is mapped onto the phase field mesh as input, so that the stored deformation energy can be used to drive the evolution of the microstructure. The two-step method is relatively easy to implement, but the one-way data transfer reduces the accuracy of the results and such approach is not capable of modeling dynamic recrystallization, where the GB migration and plasticity mutually affect each other.

Abrivard *et al.* [14] developed an iteratively-coupled model which accounts for both the GB driving force due to the stored deformation energy and the dislocation absorption by mobile GBs. In their framework, the data is mutually exchanged at each time step between phase field and crystal plasticity models. This model is therefore more applicable to studies of phenomena such as dynamic recrystallizations [14, 15]. While the model has many advantages, one of its limitations is that the coupling is hierarchical in nature due to the fact that the two individual physics models (i.e., mechanics/plasticity and phase field) are still solved separately and data exchange occurs only once per time step. This kind of loose coupling leaves open questions of stability and accuracy of the solutions, as discussed in Refs. [16, 17]. In addition, the authors followed the grain growth model proposed by Kobayashi, Warren and Craig Carter [18, 19] (often referred to as KWC model) which uses a single variable to describe the crystal orientations of all grains. This treatment of grain orientations can only deal with two dimensional problems. For three dimensional cases, an entirely different approach must be taken, for example using the quaternion representation [20]. In such case one would need to develop a completely different approach for coupling with the crystal plasticity model from what was done in Ref. [14].

One integrated approach taken by several authors involves incorporating dislocation dynamics into phase field using the microelasticity theory [21–23]. In this framework, both short-range and long-range interactions between dislocations are taken into account

and the model can account for strain hardening. In the presence of interfaces such as GBs, geometrically necessary dislocations are often taken into account in the model to physically represent the effect of interfaces on the non-uniform plastic deformation [24]. This approach provides a high level of physical fidelity. However, the fine mesh resolution required to resolve dislocations makes this approach computationally prohibitive for simulating large-scale problems, especially when one wants to combine simulations of microstructural evolution with models of dynamic mechanical contacts as we intend to do in the future.

Another approach has been introduced by Gaubert *et al.* [25] and Cottura *et al.* [26]. These authors developed phase field models that incorporate phenomenological viscoplasticity and used these models to study rafting in Ni-base superalloys. These approaches are able to address the dynamic coupling between microstructural evolution and viscoplastic deformation. By adding strain gradient plasticity formalism into their model, Cottura *et al.* [26] were also able to study the effects of precipitate size on viscoplastic behavior. However, the above framework only considers coherent interfaces, and therefore it cannot be used to simulate GB migration. In addition, although there is a free energy term in the model associated with hardening, the corresponding parameters are deliberately chosen so that the plastic driving force vanishes. Consequently, plasticity evolves the microstructure only indirectly by decreasing the elastic stress due to plastic strain. In other words, only the elastic driving force on the interface migration is present. This kind of model that neglects the plastic driving force (or more precisely, that includes the impact of plasticity effect indirectly as described above) will be referred to as a weakly coupled model in this work.

Here, we develop a multi-physics model that is coupled fully (i.e., PDEs for individual physics models are solved simultaneously) and strongly (i.e., we include plastic driving force on GB migration directly). In particular, we use CPFE method [24, 27] to simulate the plastic deformation and phase field grain growth model [28] to effectively

simulate the GB migration. We combine the FEM and Jacobian-free Newton-Krylov (JFNK) technique [29] to simultaneously solve the PDEs for both physics models (i.e., mechanics/plasticity and phase field) at each time step. More details of such FEM-JFNK approach will be discussed in Sec. 3.4. The theoretical framework developed in this work has been implemented in the MOOSE/MARMOT simulation software [30, 31] which was used to carry out all the simulations. Our model makes it possible to simulate the GB migration driven by plastic deformation. For instance, the model can be used to effectively model irregular grain growth in highly deformed materials. Note that the aim of our studies is to investigate GB migration within a bulk material and we do not include the effect of free surfaces as has been done by the authors of Refs. [32, 33].

The phase field method and crystal plasticity theory have been introduced in Sec. 2.1 and Sec. 2.2 in Chap. 2, respectively. The remainder of this chapter is organized as follows. In Secs. 3.2 to 3.4, we introduce the detailed coupling method and the strategy for solving systems of coupled PDEs that represent the two physics models in our study. In Sec. 3.5, we discuss the model parameters, including GB properties, and parameters for crystal plasticity model and the plastic potential. In Sec. 3.6, we apply the model to simulate compressive deformation of a Cu bicrystal to demonstrate the effect of plasticity on GB migration and to compare our results to published experiments where data is available. Finally a brief discussion and concluding remarks can be found in Sec. 3.7.

3.2 Elastic and plastic potential energies

When one couples a plasticity model with phase field model, the energy density ψ introduced in Eq. 2.4 would become the deformation-induced free energy. In this case, ψ consists of the elastic potential ψ^{e} and the plastic potential ψ^{p}. For any grain i,

$$\psi_i = \psi_i^{\mathrm{e}} + \psi_i^{\mathrm{p}}. \tag{3.1}$$

Considering hyperelasticity, the elastic potential energy can be written as

$$\psi_i^{\mathrm{e}} = \frac{1}{2}\mathbf{T} : \mathbf{E}^{\mathrm{e}}. \tag{3.2}$$

Plastic deformation is an energy dissipation process, with most of the plastic work spent on overcoming barriers to dislocation motion and dissipated as heat. However, a fraction of the plastic work is stored in form of elastic interactions of trapped dislocations, which is defined as the plastic potential energy. Instead of relating the plastic potential to evolving dislocation densities directly, we use an expression proposed by Ortiz and Repetto [34], where plastic potential energy is written in terms of internal variables of the previously discussed crystal plasticity model [34],

$$\psi_i^{\mathrm{p}} = A\left[\sum_{\alpha}\sum_{\beta} a^{\alpha\beta}|\gamma^{\alpha}\,\gamma^{\beta}|\right]^{3/4}. \tag{3.3}$$

Here γ^{α} and γ^{β} are the accumulated slip strains on slip systems α and β, respectively. $a^{\alpha\beta}$ is an interaction coefficient matrix, which we assume to take the same value as $q^{\alpha\beta}$ (related to work hardening through Eq. (2.13)), because both plastic potential and work hardening originate from the same physical mechanism – dislocation accumulation. A in Eq. (3.3) is a parameter related to the heat dissipation in plastic deformation. A reasonable choice of A should make the ratio δ of plastic potential rate over plastic power on the order of a few percent, with the exact value depending on a specific material [35]. Our approach to determine A will be described in more detail in Sec. 3.5.3.

3.3 Coupling of phase field and crystal plasticity

In our approach, we couple the phase field grain growth and crystal plasticity models to account for the interplay between microstructural evolution and plastic behavior in severely deformed materials. In the phase field method, the microstructure is defined

by the values of the phase field variables. However, in the crystal plasticity model, the microstructure is defined by local state variables at the integration points in the FE mesh that evolve during deformation. Thus, coupling of these two models requires a means of rectifying these two different descriptions. This is accomplished by describing multiple grains with the crystal plasticity model in the interfacial/GB regions. Mean field polycrystal plasticity methods [36] describe polycrystalline behavior using a weighted average of the stress in each individual crystal and a similar approach is taken here over the interfaces. In a grain interior, only one grain has a nonzero order parameter and thus there is only one active grain. Across the interface a number of order parameters could have nonzero values and thus be active. Based on Taylor's assumption [36], each of the active grains are assumed to experience the same strain rate. However, their stresses and internal states evolve differently. A weighted sum of stresses in different crystals provide the average stress at the material point.

In our implicit FEM approach, the iterative JFNK algorithm is used to solve for the variables values at a given time t. As part of the iterations, the residual functions for the displacements and all the phase field order parameters are evaluated at each integration point. For each evaluation, the number of active order parameters is determined by identifying the number of order parameters that have a value above a specified tolerance with value close to zero. For each active grain that was active in the previous time step, the local slip system resistances are evolved, as are the local crystal orientations. For a newly active grain, the values for these state variables are set to their initial values. Then, for active grain i, the crystal plasticity equations are solved, computing the Cauchy stress $\boldsymbol{\sigma}_i$, the elastic strain $\mathbf{E}_i^{\mathrm{e}}$, and the accumulated slip system strains γ_i^{α}. From these, the elastic and plastic potential energies, ψ_i^{e} and ψ_i^{p} are calculated. The total values at the integration points are weighted averages of the contributions from all active grains i at the integration point. Thus, the CPFE analysis is used to calculate the contribution $q_i \in \{\boldsymbol{\sigma}_i, s_i^{\alpha}, \psi_i^{\mathrm{e}}, \psi_i^{\mathrm{p}}\}$ and the final property q is obtained by interpolating q_i based on the

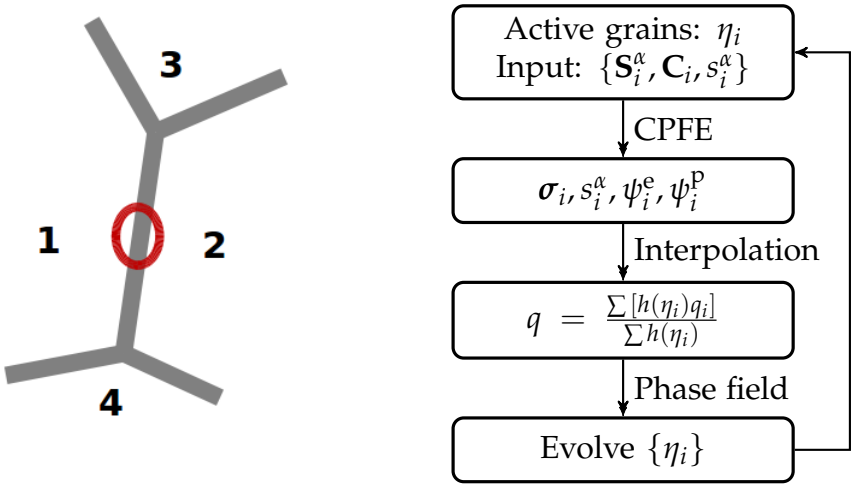

Fig. 3.1: Schematic illustration of the coupling scheme. The circled part of the GB connects two active crystals ($i = 1$ and $i = 2$). The diagram on the right outlines basic steps in the scheme. All the variables are explained in the main text. Briefly, $\mathbf{S}_i^\alpha$, $\mathbf{C}_i$, s_i^α, respectively, represent Schmid tensor, elasticity tensor, and slip system resistance in grain i. $\boldsymbol{\sigma}$, s^α, ψ^{e}, ψ^{p}, respectively, stand for Cauchy stress, slip system resistance, elastic and plastic potential on the GB. q and q_i represent a general property, i.e., $q \in \{\boldsymbol{\sigma}, s^\alpha, \psi^{\mathrm{e}}, \psi^{\mathrm{p}}\}$ and $q_i \in \{\boldsymbol{\sigma}_i, s_i^\alpha, \psi_i^{\mathrm{e}}, \psi_i^{\mathrm{p}}\}$.

weights of active grains $\{i\}$ according to

$$q = \frac{\sum h(\eta_i) q_i}{\sum h(\eta_i)}. \tag{3.4}$$

Here, $h(\eta_i) = \frac{1}{2}[1 + \sin(\pi(\eta_i - \frac{1}{2}))]$ is the interpolation weight function. These values are then used in the computation of the order parameter residuals. This process is illustrated in Fig. 3.1. Note that during each JFNK iteration, the residuals for displacements and order parameters are driven down simultaneously, as discussed in Sec. 3.4.

The above approach defines the plastic deformation behavior at the GB region. Since GB atomic structure is disordered and there are no well defined slip systems within the GBs, the plastic behavior of the GB region can be challenging to model. An al-

ternative approach would be to apply a sharp interface scheme, where all properties change abruptly and discontinuously across a GB. However, the infinite derivatives of properties across a GB can lead to convergence issues when the GB migrates. It is more common in phase field models to create continuously changing interface properties by applying some kind of interpolation scheme as done here. One of the approaches that has been shown to work well for pure elasticity problems [37, 38] is based on order parameter dependent weighted interpolation of elasticity tensors, which employs the actual gradient field of the order parameter. However, this approach cannot be used to interpolate Schmid tensors in the present case, because the rotation transformation and the interpolation do not preserve the zero trace property of the effective Schmid tensors. Therefore, we represent multiple active grains across the GB and use a weighted sum of their properties.

During grain growth in plastically deformed materials, a migrating GB leaves behind material with reduced dislocation density. This phenomenon may occur during a recrystallization process, where the stored deformation energy is the main driving force for GB migration [39]. We describe this phenomenon in our coupling approach when we set the slip system resistances for newly active grains to the initial value. For example, consider an integration point at which only order parameter five is active (the point is currently in the interior of grain five). This point has been plastically deforming such that the several of the slip system resistances are significantly above their initial value. Now, the boundary with grain eight approaches, such that order parameter eight is now active at the integration point and all its slip system resistances are reset to the initial state. Thus, grains five and eight are active, though grain five has significantly higher slip system resistance. The GB continues to migrate until order parameter five goes inactive, leaving only order parameter eight, with the lower slip resistances, such that the GB migration effectively reduces the dislocation density.

Under the coupling formulation introduced in this section, the derivatives of elastic

and plastic potential energy (eqs. (3.1)-(3.3)) with respect to the order parameter η_i are

$$\frac{\partial \psi^{\mathrm{e}}}{\partial \eta_i} = \frac{\psi_i^{\mathrm{e}} - \psi^{\mathrm{e}}}{\sum_i h(\eta_i)} \frac{\partial h(\eta_i)}{\partial \eta_i} \tag{3.5}$$

and

$$\frac{\partial \psi^{\mathrm{p}}}{\partial \eta_i} = \frac{\psi_i^{\mathrm{p}} - \psi^{\mathrm{p}}}{\sum_i h(\eta_i)} \frac{\partial h(\eta_i)}{\partial \eta_i}. \tag{3.6}$$

The derivative $\frac{\partial \psi}{\partial \eta_i} = \frac{\partial \psi^{\mathrm{e}}}{\partial \eta_i} + \frac{\partial \psi^{\mathrm{p}}}{\partial \eta_i}$ enters the Allen-Cahn equation (Eq. (2.6)) as discussed in Sec. 3.4.

Note that in our model we do not include the effect of the deformation-induced microstructure distortion as discussed in Ref. [40], since this effect is weak for low and intermediate deformation rates.

3.4 Jacobian-free Newton-Krylov (JFNK) method

We solve the nonlinear system of coupled PDEs using FEM. To prepare for the FEM discretization, we construct the weak form of Eqs. (2.6) and (2.15) in residual form

$$\begin{aligned} \boldsymbol{R}_1 = &\left(\frac{\partial \eta_i}{\partial t}, \phi_m\right) + L(\kappa_i \nabla \eta_i, \nabla \phi_m) - L\langle \kappa_i \nabla \eta_i \cdot \vec{n}, \phi_m \rangle \\ &+ L\left(\frac{\partial f_0}{\partial \eta_i} + \frac{\partial \psi^{\mathrm{e}}}{\partial \eta_i} + \frac{\partial \psi^{\mathrm{p}}}{\partial \eta_i}, \phi_m\right) = \boldsymbol{0} \end{aligned} \tag{3.7}$$

and

$$\boldsymbol{R}_2 = \left(\rho_0 \frac{\partial^2 \boldsymbol{u}}{\partial t^2}, \phi_m\right) - (\boldsymbol{\sigma}, \nabla \phi_m) + \langle \boldsymbol{\sigma} \cdot \vec{n}, \phi_m \rangle = \boldsymbol{0}, \tag{3.8}$$

where ρ_0 is the material density, ϕ_m is the test function, and $(\cdot)$ and $\langle \cdot \rangle$ represent volume and boundary integrals, respectively.

To solve a general vector of nonlinear residual equations $\boldsymbol{R}(\boldsymbol{x}) = \boldsymbol{0}$, one can use Newton's method which involves iterations of the following steps

(1) Compute the Jacobian matrix of the residual: $\boldsymbol{J}(\boldsymbol{x}) = \frac{\partial \boldsymbol{R}(\boldsymbol{x})}{\partial \boldsymbol{x}}$;

(2) Solve $\boldsymbol{J}(\boldsymbol{x}_k)\delta\boldsymbol{x} = -\boldsymbol{R}(\boldsymbol{x}_k)$ for $\delta\boldsymbol{x}$;

(3) Update $\boldsymbol{x}_{k+1} = \boldsymbol{x}_k + \delta\boldsymbol{x}$.

The iteration is continued until $\delta\boldsymbol{x}$ is sufficiently small or some other stopping criterion is met. However, for problems with large numbers of degrees of freedom (where the degrees of freedom is equal to the number of nodes multiplied by the number of variables in PDEs), the cost of calculating the Jacobian is typically very high and usually dominates the computation [30]. In addition, in multi-physics problems or nonlinear mechanics problems with complicated constitutive laws, the Jacobian can be difficult to determine and approximating the Jacobian slows or even prevents convergence [41].

In the JFNK approach, the Krylov solver does not require the Jacobian itself but instead the action of the Jacobian on a vector, $\boldsymbol{J}(\boldsymbol{x}_k)\boldsymbol{v}$. This Jacobian vector product can be approximated efficiently with finite difference method according to [29, 42]

$$\boldsymbol{J}(\boldsymbol{x}_k)\boldsymbol{v} \approx \frac{\boldsymbol{R}(\boldsymbol{x}_k + \epsilon\boldsymbol{v}) - \boldsymbol{R}(\boldsymbol{x}_k)}{\epsilon}, \tag{3.9}$$

where $\epsilon \ll 1$. The above finite difference approximation is used together with the generalized minimum residual method [43] to solve the Jacobian system. In order to make the computation more efficient, JFNK is usually applied along with a right preconditioning $\boldsymbol{J}(\boldsymbol{x}_k)M^{-1}(M\delta\boldsymbol{x}_k) = -\boldsymbol{R}(\boldsymbol{x}_k)$, where M^{-1} is the preconditioner. Eq. (3.9) becomes

$$\boldsymbol{J}(\boldsymbol{x}_k)M^{-1}\boldsymbol{v} \approx \frac{\boldsymbol{R}(\boldsymbol{x}_k + \epsilon M^{-1}\boldsymbol{v}) - \boldsymbol{R}(\boldsymbol{x}_k)}{\epsilon}. \tag{3.10}$$

Thus, the exact Jacobian is not required for convergence but does accelerate convergence. A common means of simplifying the preconditioning matrix is to only consider the diagonal blocks of the Jacobian, i.e., the blocks corresponding to the partial derivatives of the residual function with respect to its corresponding variable. This can drastically simplify the matrix for systems with many variables. In this approach we used this

approach and achieved reasonable convergence using JFNK.

The combination of FEM and the preconditioned JFNK approach allows one to simultaneously solve all the PDEs for coupled multi-physics problems at each time step, which guarantees high accuracy of the solution. This approach has been implemented in MOOSE software package.

3.5 Model parameterization

3.5.1 GB properties

We use the value of GB energy for pure Cu as determined from MD simulations by Schönfelder *et al.* [44], i.e., $\sigma_{\mathrm{GB}} = 0.708\ \mathrm{J/m^2}$. GB mobility m_{GB} in our phase field model is obtained from experimental measurements by Viswanathan and Bauer [45]. The authors studied GB migration in 99.999 wt.% purity Cu bicrystals with [001] rotation axis and they found the reduced GB mobility $m^{\star}_{\mathrm{GB}}$ ($m^{\star}_{\mathrm{GB}} = m_{\mathrm{GB}} \cdot \sigma_{\mathrm{GB}}$) to be in the range of $(0.975 - 1250) \times 10^{-13}\ \mathrm{m^2/s}$ at the temperature of $773 - 848$ K. Given the value of σ_{GB} assumed in our simulations, we can obtain the range of m_{GB} to be $1.38 \times 10^{-13} - 1.75 \times 10^{-10}\ \mathrm{m^4/(J \cdot s)}$. Therefore in our simulations we choose an intermediate value $m_{\mathrm{GB}} = 1.0 \times 10^{-12}\ \mathrm{m^4/(J \cdot s)}$. Here, we use the GB mobility variable to effectively capture the GB kinetics without considering explicitly the underlying physical mechanisms.

Phase field parameters μ, γ, κ_i and L (first introduced in Sec. 2.1) are determined from σ_{GB} and m_{GB} according to Eq. 2.7 developed by Moelans *et al.* [46].

3.5.2 Parameters of the crystal plasticity model

Most of the parameters for the crystal plasticity model of Cu are taken from Refs. [24, 47, 48] and these parameters are summarized in Table 3.1. For well annealed pure materials with negligible initial dislocation densities, the initial slip resistance s_0 is mainly due to the lattice friction, which must be overcome to move an individual dislocation. Therefore, here we approximate the initial slip resistance, assumed to be the same for all

Table 3.1: Crystal plasticity model parameters for Cu. In the table, m is strain rate sensitivity, $\dot{\gamma}_0$ is the reference slip rate (defined in Eq. (2.11)), c and h_0 are constants in the hardening matrix (Eq. (2.13)), $q^{\alpha\beta}$ is latent hardening coefficient, s_0 and s_s are the initial and the saturated slip system resistances, respectively, and C_{11}, C_{12} and C_{44} are the elastic constants.

Parameter	Value	Units
m	0.050 [48]	
$\dot{\gamma}_0$	0.001 [47]	s^{-1}
c	2.5 [47]	
$q^{\alpha\beta}$ $(\alpha = \beta)$	1.0 [24]	
$q^{\alpha\beta}$ $(\alpha \neq \beta)$	1.4 [24]	
h_0	541.5 [47]	MPa
s_0	10	MPa
s_s	110 [47]	MPa
C_{11}	1.684×10^5 [47]	MPa
C_{12}	1.214×10^5 [47]	MPa
C_{44}	7.500×10^4 [47]	MPa

slip systems in our simulations, with the value of the Peierls-Nabarro stress τ_{PN} [49, 50]

$$s_0 \approx \tau_{PN} = G \exp(-2\pi W/b), \tag{3.11}$$

where $W = \frac{d}{1-\nu}$ is the dislocation width, ν is Poisson's ratio, d and b are interplanar distance and the length of Burgers vector, respectively, and G is the shear modulus. For the $\langle 110 \rangle$ $\{111\}$ slip system in Cu, ν = 0.34, $d = 2.1$ Å, $b = 2.55$ Å, and $G = 27$ GPa [51]. Based on these values, s_0 is calculated to be around 10 MPa. The strain rate sensitivity m is chosen to be 0.05, corresponding to the temperature of around 800 K [48].

In order to test the validity of the parameters used in our crystal plasticity model, we simulate uniaxial compression of a 2D polycrystalline Cu sample without grain growth as shown in Fig. 3.2. The deformation is displacement-controlled so that the desired engineering strain rates $\dot{e}$ can be achieved. We calculate the stress field throughout the deformation process and determine the Von Mises equivalent stress σ_{vm} as a function of the equivalent true strain ε, and the results are plotted in Fig. 3.2. The simulated polycrystal has dimensions of 20 μm $\times$ 20 μm and it consists of 15 grains with the average grain diameter of around 5.9 μm. The polycrystal was prepared by Voronoi tessellation method starting with a random distribution of grain centers and grain orientations. We fit an empirical power law hardening equation $\sigma_{\text{vm}} = K\,\varepsilon^n$ to the calculated σ_{vm}-ε data set. Here, K is the work hardening coefficient, which depends on strain rate, and n is the work hardening exponent. The fitted K and n values for different strain rates are listed in Table 3.2. Typical values of K and n for Cu polycrystals deformed at experimental engineering strain rates ($\dot{e} = 10^{-3} - 10^{-4}$ s^{-1}) are reported as $K = 420 - 480$ MPa and $n = 0.35 - 0.50$ [48], which are reasonably close to our predicted values of K = 512 MPa and n = 0.446 for $\dot{e} = 10^{-3}$ s^{-1} and K = 457 MPa and n = 0.445 for $\dot{e} = 10^{-4}$ s^{-1}. This good agreement indicates that the crystal plasticity model with parameters in Table 3.1 can be used effectively to model large plastic deformation behavior of Cu.

3.5.3 Plastic potential parameters

The plastic energy stored in deformation is represented with an energy function developed by Ortiz and Repetto [34] and shown in Eq. (3.3). Here we discuss our approach to determine the value of the prefactor A in that equation. In general, A can be obtained by measuring experimentally the ratio of the dissipated heat over the total plastic work and fitting the parameter A in simulations to reproduce this ratio. Here, we determine A by fitting the potential energy data predicted from Eq. (3.3) at different strains to the energy calculated from an empirical formula for stored dislocation energy density

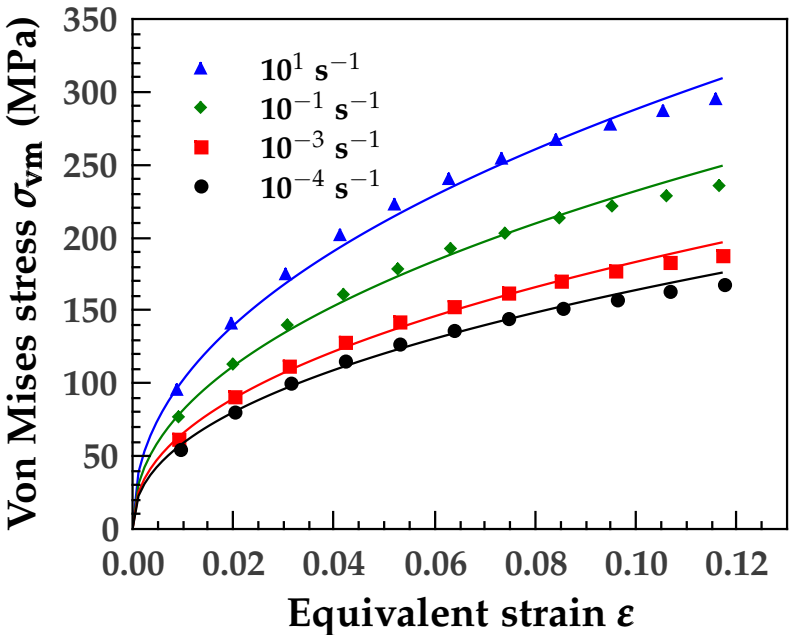

Fig. 3.2: (Color online) Predicted Von Mises equivalent stress $\sigma_{\rm vm}$ as a function of the equivalent true strain ε for a 2D polycrystalline Cu sample deformed at different engineering strain rates $\dot{e}$. The sample was compressed along one of the two dimensions and the boundaries along the other dimension were relaxed. The solid curves were obtained from the power law $\sigma_{\rm vm} = K\,\varepsilon^{n}$ with fitted parameters in Table 3.2.

Table 3.2: Fitted parameters in the hardening law ($\sigma_{\rm vm} = K\,\varepsilon^{n}$) of a simulated 2D polycrystalline Cu at different engineering strain rates $\dot{e}$. The ranges of experimental values of these parameters reported for Cu are $K = 420 - 480$ MPa and $n = 0.35 - 0.50$ [48].

$\dot{e}$ (s^{-1})	K (MPa)	n
1×10^{1}	812	0.448
1×10^{-1}	660	0.454
1×10^{-3}	512	0.446
1×10^{-4}	457	0.445

$$E^{\text{disl}} = \alpha' G b^2 \rho, \tag{3.12}$$

where ρ is dislocation density, α' is a dimensionless coefficient ranging from $0.3 - 0.5$ (here we assume $\alpha' = 0.4$), G is the shear modulus, and b is the length of Burgers vector.

Before we can determine A, first we express the dislocation density ρ in terms of internal variables of our model, and then we verify the applicability of the expression. Empirical data obtained for a large number of alloys and metals [52–55] suggests that ρ, irrespectively of the exact details of the spatial distributions of dislocations, can be approximately related to the slip system resistance s as

$$s = s_0 + \alpha' G b \rho^{1/2}, \tag{3.13}$$

where s_0 is the initial slip resistance and is assumed the same here for all slip systems, and s is the current slip resistance averaged over all slip systems. Equation (3.12) can be thus reduced to

$$E^{\text{disl}} = \frac{(s - s_0)^2}{\alpha' G}. \tag{3.14}$$

To verify that reasonable dislocation densities can be predicted by Eq. (3.13) from the values of slip system resistance in our model, we calculate the dislocation densities in a deformed 2D Cu single crystal and we compare them to dislocation densities measured experimentally and reported in Refs. [56–58]. In simulations, we apply an uniaxial compressive engineering strain of 10^{-3} s^{-1} along either the [100] or the [110] direction. Experimental specimens, even those that are reported as well-annealed, often have an initial non-negligible density of stored dislocations before the deformation is applied. The initial dislocation densities are usually introduced during synthesis and processing of specimens or they are left behind after annealing due to the incomplete dislocation annihilations. This initial dislocation density is accounted for in the initial slip resistance and is not included in the calculation of the dislocation density from Eq. (3.13). For this reason, when comparing to results of our model, we subtracted the initial dislocation

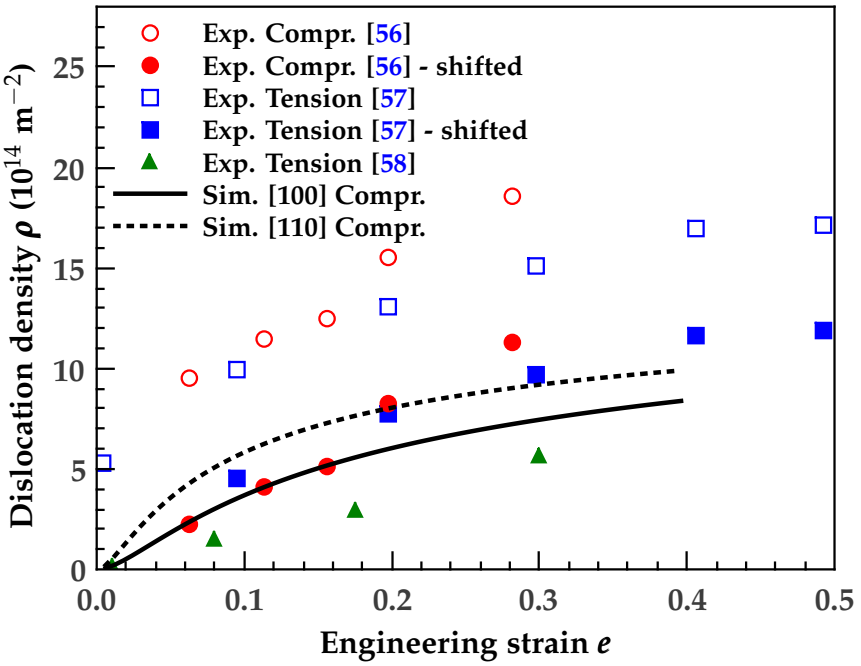

Fig. 3.3: (Color online) Comparison of dislocation densities calculated in our simulations to those determined experimentally (Refs. [56–58]). Solid and dashed lines show dislocation densities calculated using Eq. (3.13) from simulations of a Cu single crystal compressed at the engineering strain rate of 10^{-3} s^{-1} along the [100] and the [110] directions, respectively. Open symbols represent dislocation densities measured experimentally during uniaxial compression (Ref. [56]) or uniaxial tension (Refs. [57, 58]). The corresponding solid symbols represent experimental data shifted by the initial dislocation densities (equal to the offset on the vertical axis). "Compr.", "Exp." and "Sim." stand for "Compression", "Experiment" and "Simulation", respectively.

density from the original experimental data. The calculated dislocation density and the original and shifted experimental data are plotted in Fig. 3.3. Note that the data from Ref. [58] was not shifted because the initial dislocation density was already zero. Two curves are reported for the simulated data corresponding to uniaxial compression along [100] (solid line) and along [110] (dashed line) directions. The different dislocation densities for these two curves result from the plastic anisotropy of Cu crystal. Considering that the experimental specimens are polycrystalline and consist of grains with different orientations, the dislocation densities calculated from our model show a quite good agreement with the reported data. This agreement implies that Eqs. (3.13) and (3.14) can predict a reasonable dislocation density and stored deformation energy, respectively.

One should keep in mind that although Eq. (3.14) can be used to approximate the stored deformation energy, we choose not to use it for derivation of the plastic driving force. This is because the variable s in Eq. (3.14) is an average over all local slip systems, and it cannot capture the anisotropic nature of plastic deformation. Instead, Eq. (3.14) is only used to determine the prefactor A in the plastic potential function (Eq. (3.3)).

Having verified the empirical relation in Eq. (3.14), we can now determine the value of prefactor A (in Eq. (3.3)) using the fitting method described earlier in this section. Specifically, we simulate uniaxial compression of a 2D Cu single crystal at an engineering strain rate of 10^{-3} s^{-1} with the compression axis being parallel to either the [100] or the [110] direction. The BCs and system size in these simulations were the same as for the simulations that led to results shown in Fig. 3.3. The stored dislocation energy density, elastic potential and fitted plastic potential for [100] compression direction are plotted in Fig. 3.4. We find that the prefactor A is inversely proportional to the average slip strain $\overline{\gamma}$ over all slip systems

$$A = \frac{1}{k \cdot \overline{\gamma}} \text{ MPa}, \tag{3.15}$$

where $\overline{\gamma} = \frac{1}{12}\sum_{\alpha} \gamma^{\alpha}$, the constant k depends weakly on the deformation direction and

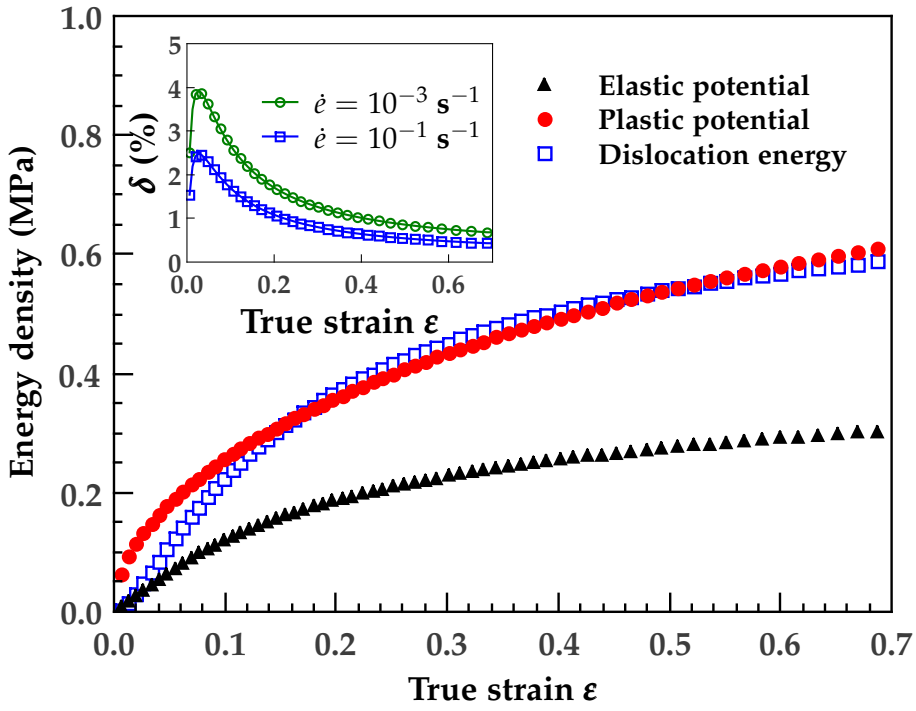

Fig. 3.4: (Color online) Dislocation energy density, elastic potential and fitted plastic potential of Cu single crystal compressed in simulation along [100] direction at an engineering strain rate $\dot{e} = 10^{-3}$ s^{-1}. The elastic potential and dislocation energy are computed from Eq. (3.2) and Eq. (3.14), respectively. The plastic potential is calculated from Eq. (3.3) where the prefactor A takes the form in Eq. (3.15). The inset shows the ratio δ of plastic potential over plastic work as a function of true strain ε for strain rate $\dot{e} = 10^{-3}$ s^{-1} and $\dot{e} = 10^{-1}$ s^{-1}.

is either 7.0 (for [100] direction) or 7.5 (for [110] direction). Therefore, we choose an intermediate value $k = 7.2$ in our later simulations of bicrystals. The ratio δ of plastic potential rate over plastic work rate is also calculated for different strain rates and shown in the inset of Fig. 3.4. We find that the value of δ is on the order of a few percent and shows a relatively weak strain rate dependence (a decrease of δ by less than 37% for an increase of $\dot{e}$ from 10^{-3} s^{-1} to 10^{-1} s^{-1}). The small value of δ and the relatively weak strain rate dependence are in a qualitative agreement with experimental findings in Refs. [35, 59].

3.6 Simulating GB migration using the coupled model

3.6.1 GB migration under different driving forces

The effect of plasticity on GB migration is illustrated in a simulation of compressive loading of a 2D Cu bicrystal with dimensions of 20 μm $\times$ 20 μm. Fig. 3.5 shows the geometry of the bicrystal in undeformed and deformed states, with two grains initially rotated by 45° relative to each other around the tilt [001] axis. The GB is normal to the x-axis, and the initial GB position is at $x = 10$ μm. The compressive load is applied along the y-axis at an engineering strain rate of $\dot{e} = 1.0 \times 10^{-2}$ s^{-1}.

In our simulations we assume that individual grains have a single static crystal orientation without any gradient or heterogeneity, which renders a constant elasticity and Schmid tensor throughout each grain. In reality, this assumption does not have to be valid and there can be small variations in the orientation within a deformed grain due to the heterogeneous distribution of dislocations. For instance, transmission electron microscopy (TEM) observations of dislocation arrangements by Bailey *et al.* [58, 60] in polycrystalline Cu indicate that the dislocations form cell structures with relatively dislocation-free interior of the cells. Bailey *et al.*'s analysis also shows that the misorientations across the cell walls are equal or smaller than 2° in Cu foil deformed in uniaxial

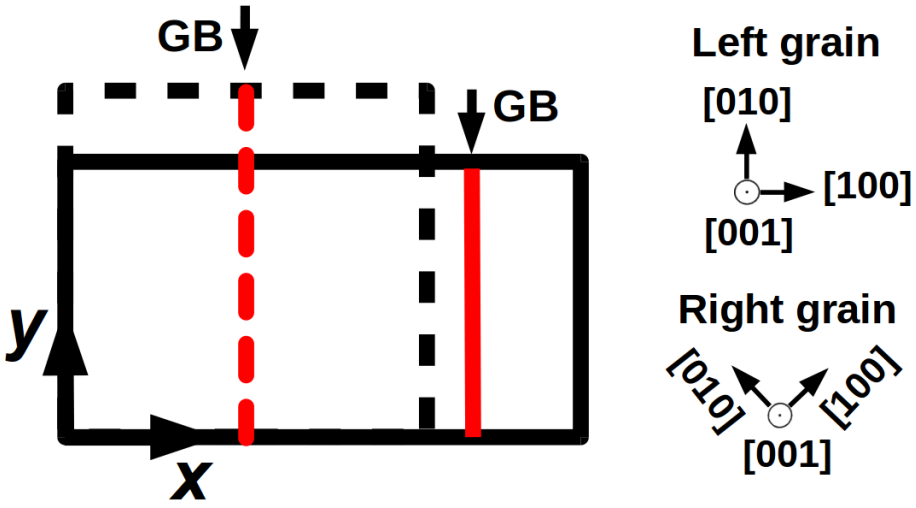

Fig. 3.5: Schematic representation of a bicrystal simulation cell before (dashed) and after (solid) deformation. GB positions are indicated by arrows. Before deformation, the right grain is rotated with respect to the left one by 45° around the [001] axis. A compressive load is applied at an engineering strain rate of 1.0×10^{-2} s^{-1} along the y direction.

tension up to 30% strain. Since such small misorientations would not cause big changes in elastic constants or slip system orientations, our approximation that these properties are uniform within each grain is reasonable.

In order to compare the effects of elasticity and plasticity on GB migration, we conduct the following three simulations on the same bicrystal model, but with three different material models and driving forces for GB migration:

I Linear elasticity model for deformation, with only elastic driving force for GB migration;

II Crystal plasticity model for deformation, with only elastic driving force (Eq. (3.5)) for GB motion included explicitly in the model;

III Crystal plasticity model for deformation, with both elastic (Eq. (3.5)) and plastic (Eq. (3.6)) driving forces for GB migration explicitly included in the model.

In all cases, GB migrates to the right (although the GB velocity vary among the three cases), because the left grain has a lower potential energy density than the right one. The energy difference between these two grains drives the GB to migrate in such a way that the system potential energy is decreased. The crystallographic orientation of the left grain is preferred during texture development under the load conditions applied in our simulations. GB migration distances as a function of time are plotted in Fig. 3.6. In the linear elasticity simulations (case I), all of the externally applied work is transferred into the elastic potential energy without any dissipation. As a result, the driving force for GB migration in case I is the largest among all three cases. Crystal plasticity approach (cases II and III), on the other hand, includes the energy dissipation effect in the construction of the driving forces on GB migration as discussed in Sec. 3.2. The difference between GB velocities for case II and case III, shown in Fig. 3.6, demonstrates that the stored dislocation energy provides a significant driving force for GB migration, especially for large deformations.

3.6.2 Dislocation absorptions by mobile GBs

As we discussed in Sec. 3.3, in order to model reduction of dislocation density behind a moving GB, newly active grains are initialized with slip system resistances at the initial value. The purpose is to capture qualitatively absorption of crystal lattice dislocations by GBs. Consequently, dislocation density, plastic potential and material hardness are also reduced. There are two competing processes included in our model that contribute to the change in dislocation density ($d\rho$): (i) Dislocation increase ($d\rho^+$) is induced by continued deformation and (ii) Dislocation reduction ($d\rho^-$) occurs due to absorption of dislocation by a moving GB. One can therefore write

$$d\rho = d\rho^+ + d\rho^-. \tag{3.16}$$

Since the material undergoes plastic deformation continuously in our simulation, in

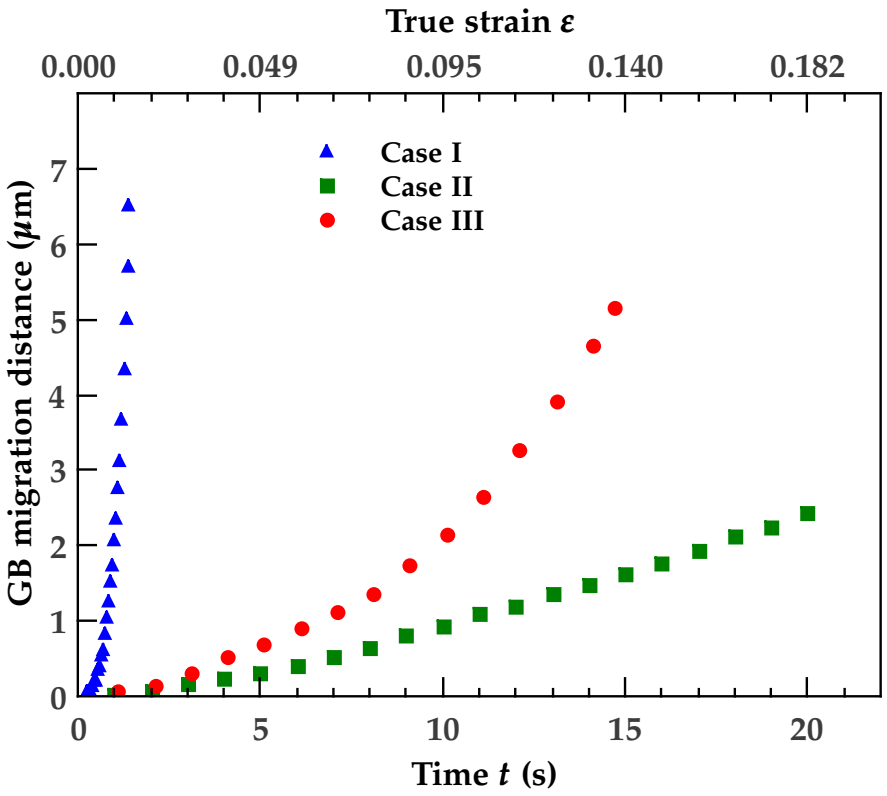

Fig. 3.6: (Color online) Comparison of GB migration distances predicted by case I (linear elasticity), case II (crystal plasticity with only elastic driving force) and case III (crystal plasticity with both elastic and plastic driving forces).

the initial stage of the simulation when the slip system resistances are near their initial values and the plastic driving force is low, the first term ($d\rho^+$) dominates. At a later stage (at $t = 9 - 10$ s in our simulation), as the slip system resistances get larger, the second term ($d\rho^-$) becomes increasingly important. The combined effect of the two terms leads to an abrupt decrease of ρ and forms a local minimum right behind a moving GB due to the dominance of $d\rho^-$, and a gradual increase of ρ away from the GB (until a plateau is reached) due to the increasing dominance of $d\rho^+$. Since slip system resistance, plastic potential, and Von Mises equivalent stresses are all closely related to dislocation density, these variables should show similar trends. Profiles of these variables across a migrating GB are plotted in Fig. 3.7. The abrupt decrease and the gradual increase of these property values are indicated by vertical and inclined arrows, respectively. The local minimum of dislocation density behind the GB is responsible for the distinct change in the slope of the GB migration distance curve between 9 and 10 seconds for case III in Fig. 3.6. This is because this local minimum increases the energy gradient across the GB and therefore it increases the plastic driving force for GB migration.

The dislocation-reduced region, predicted in our model, has also been observed experimentally in the microstructure of deformed polycrystalline Cu. For instance, Bailey and Hirsch [60] investigated static annealing of deformed Ni and Cu, and they reported that there were comparatively few dislocations in the region through which the GB has moved. Sakai *et al.* [61] reported TEM observations of Cu microstructure during discontinuous dynamic recrystallization and their studies indicate that GB migration left behind a dislocation-free region and new dislocations accumulated further away from the mobile GB. Our simulations are in a qualitative agreement with such experiments.

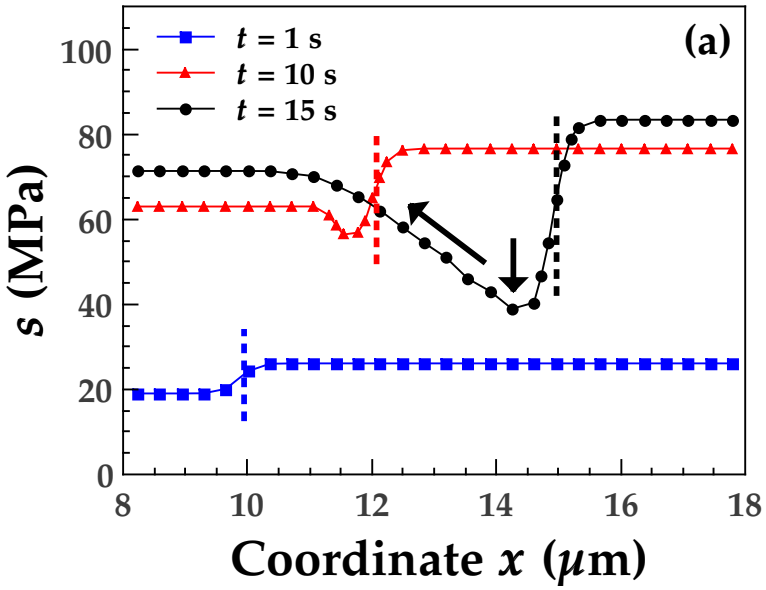
(a)
t = 1 s
t = 10 s
t = 15 s
s (MPa)
Coordinate x (μm)
0
20
40
60
80
100
8
10
12
14
16
18

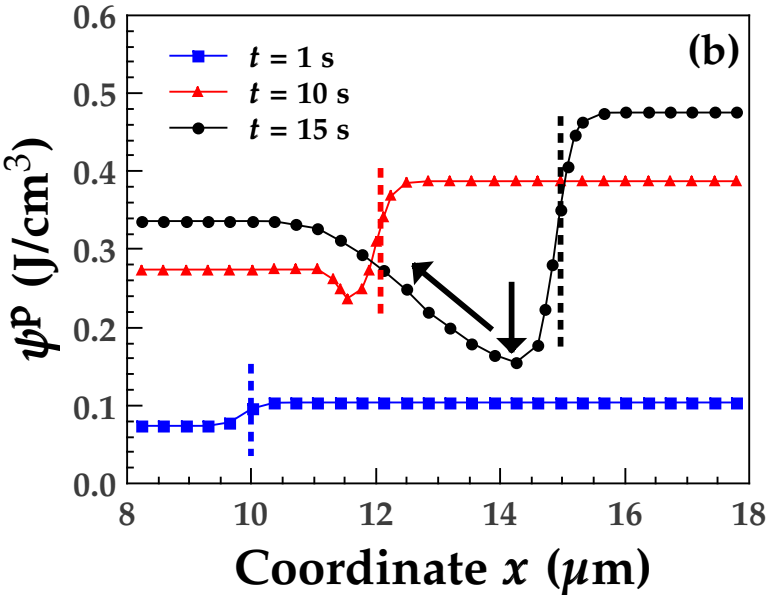
(b)
t = 1 s
t = 10 s
t = 15 s
ψP (J/cm3)
Coordinate x (μm)
0.0
0.1
0.2
0.3
0.4
0.5
0.6
8
10
12
14
16
18

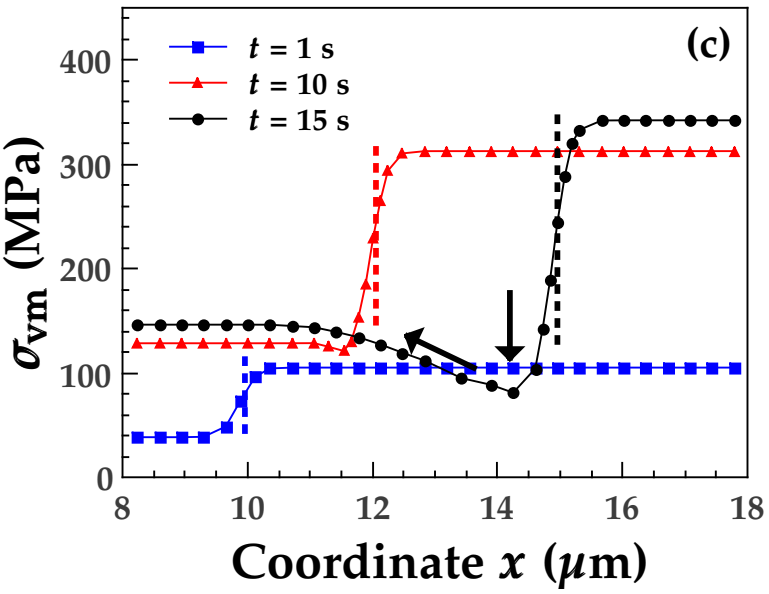

Fig. 3.7: (Color online) Profiles of weight averaged properties (calculated from Eq. (3.4)) as a function of the coordinate x across GB at different times t. (a) Slip system resistance s averaged over all slip systems; (b) Plastic potential ψ^{p}, and (c) Von Mises stress σ_{vm}. GB positions at different times are indicated with vertical dashed lines. The vertical arrows indicate the minima of these properties in the region behind the moving GB, whereas the inclined arrows represent a gradual increase of the property values away from the GB until a plateau is reached. The minima of these properties start to develop at $t = 9 - 10$ s.

3.7 Discussion and Conclusions

Our coupling model combines crystal plasticity with phase field grain growth to enable simulations of plasticity effects on GB migration. Our simulations show that the stored deformation energy exerts a strong driving force on GB motion, especially at large strains. Many experiments [60, 62–65] have shown that, in a highly deformed material, a mobile GB absorbs dislocations encountered in its pathway so that the dislocation density is lowered in the region swept by the GB. In our framework, we assume the migration of GB completely resets the material to its original dislocation density. This approach does not distinguish among the different physical mechanisms of interaction between dislocation and GB. These mechanisms can include: 1) GBs acting as barriers to dislocation motion, 2) partial transfer of dislocations across GBs, and 3) GBs acting as sources and sinks of dislocations. One should also keep in mind that in our model the mechanisms for GB movement are incorporated effectively into GB mobility, instead of being included explicitly.

The main conclusions of this chapter can be summarized as follows:

1) We developed a multi-physics model where the phase field grain growth model and CPFE method are fully coupled. In other words, FEM-JFNK numerical approach is applied to simultaneously solve the nonlinear system of PDEs for both physics models;

2) The multi-physics model is strongly coupled as it incorporates explicitly the plastic driving force for GB migration. Also, our model captures qualitatively the interaction of dislocations with mobile GBs, and leads to formation of dislocation-free region behind a moving GB, as were observed in experiments.

References

[1] L Zhao, P Chakraborty, MR Tonks, and I Szlufarska. On the plastic driving force of grain boundary migration: A fully coupled phase field and crystal plasticity model. *Computational Materials Science*, 128:320–330, 2017.

[2] HW Zhang, ZK Hei, Gang Liu, J Lu, and K Lu. Formation of nanostructured surface layer on AISI 304 stainless steel by means of surface mechanical attrition treatment. *Acta Materialia*, 51(7):1871–1881, 2003.

[3] X Wu, N Tao, Y Hong, G Liu, B Xu, J Lu, and K Lu. Strain-induced grain refinement of cobalt during surface mechanical attrition treatment. *Acta Materialia*, 53(3):681–691, 2005.

[4] K Wang, NR Tao, G Liu, J Lu, and K Lu. Plastic strain-induced grain refinement at the nanometer scale in copper. *Acta Materialia*, 54(19):5281–5291, 2006.

[5] Alfons Fischer, Sabine Weiß, and Markus A Wimmer. The tribological difference between biomedical steels and CoCrMo-alloys. *Journal of the Mechanical Behavior of Biomedical Materials*, 9:50–62, 2012.

[6] David G Morris and MA Munoz-Morris. Microstructure of severely deformed Al–3Mg and its evolution during annealing. *Acta Materialia*, 50(16):4047–4060, 2002.

[7] Pedro A Romero, Tommi T Järvi, Nils Beckmann, Matous Mrovec, and Michael Moseler. Coarse graining and localized plasticity between sliding nanocrystalline metals. *Physical Review Letters*, 113(3):036101, 2014.

[8] Izabela Szlufarska, Aiichiro Nakano, and Priya Vashishta. A crossover in the mechanical response of nanocrystalline ceramics. *Science*, 309(5736):911–914, 2005.

[9] Ao Li and Izabela Szlufarska. How grain size controls friction and wear in nanocrystalline metals. *Physical Review B*, 92(7):075418, 2015.

[10] Tomohiro Takaki, Akinori Yamanaka, and Yoshihiro Tomita. Phase-field modeling and simulation of nucleation and growth of recrystallized grains. In *Materials Science Forum*, volume 558, pages 1195–1200. Trans Tech Publ, 2007.

[11] T Takaki and Y Tomita. Static recrystallization simulations starting from predicted deformation microstructure by coupling multi-phase-field method and finite element method based on crystal plasticity. *International Journal of Mechanical Sciences*, 52(2):320–328, 2010.

[12] Onur Güvenç, Markus Bambach, and Gerhard Hirt. Coupling of crystal plasticity finite element and phase field methods for the prediction of SRX kinetics after hot working. *Steel Research International*, 85(6):999–1009, 2014.

[13] Alexander Vondrous, Pierre Bienger, Simone Schreijäg, Michael Selzer, Daniel Schneider, Britta Nestler, Dirk Helm, and Reiner Mönig. Combined crystal plasticity and phase-field method for recrystallization in a process chain of sheet metal production. *Computational Mechanics*, 55(2):439–452, 2015.

[14] Guillaume Abrivard, Esteban P Busso, Samuel Forest, and Benoit Appolaire. Phase field modelling of grain boundary motion driven by curvature and stored energy gradients. Part I: theory and numerical implementation. *Philosophical Magazine*, 92(28-30):3618–3642, 2012.

[15] Guillaume Abrivard, Esteban P Busso, Samuel Forest, and Benoit Appolaire. Phase field modelling of grain boundary motion driven by curvature and stored energy gradients. Part II: application to recrystallisation. *Philosophical magazine*, 92(28-30):3643–3664, 2012.

[16] D Gaston, G Hansen, S Kadioglu, DA Knoll, C Newman, H Park, C Permann, and W Taitano. Parallel multiphysics algorithms and software for computational nuclear engineering. In *Journal of Physics: Conference Series*, volume 180, page 012012. IOP Publishing, 2009.

[17] SR Novascone, BW Spencer, D Andrs, RL Williamson, JD Hales, and DM Perez. Results from tight and loose coupled multiphysics in nuclear fuels performance simulations using BISON. In *International Conference on Mathematics & Computational Methods Applied to Nuclear Science & Engineering, Sun Valley, Idaho*, 2013.

[18] Ryo Kobayashi, James A Warren, and W Craig Carter. A continuum model of grain boundaries. *Physica D: Nonlinear Phenomena*, 140(1):141–150, 2000.

[19] James A Warren, Ryo Kobayashi, Alexander E Lobkovsky, and W Craig Carter. Extending phase field models of solidification to polycrystalline materials. *Acta Materialia*, 51(20):6035–6058, 2003.

[20] T Pusztai, G Bortel, and L Gránásy. Phase field theory of polycrystalline solidification in three dimensions. *EPL (Europhysics Letters)*, 71(1):131, 2005.

[21] Yu U Wang, YM Jin, AM Cuitino, and AG Khachaturyan. Nanoscale phase field microelasticity theory of dislocations: model and 3D simulations. *Acta Materialia*, 49(10):1847–1857, 2001.

[22] Marisol Koslowski, Alberto M Cuitino, and Michael Ortiz. A phase-field theory of dislocation dynamics, strain hardening and hysteresis in ductile single crystals. *Journal of the Mechanics and Physics of Solids*, 50(12):2597–2635, 2002.

[23] D Rodney, Y Le Bouar, and A Finel. Phase field methods and dislocations. *Acta Materialia*, 51(1):17–30, 2003.

[24] F Roters, P Eisenlohr, L Hantcherli, DD Tjahjanto, TR Bieler, and D Raabe. Overview of constitutive laws, kinematics, homogenization and multiscale methods in crystal plasticity finite-element modeling: Theory, experiments, applications. *Acta Materialia*, 58(4):1152–1211, 2010.

[25] Anaïs Gaubert, Yann Le Bouar, and Alphonse Finel. Coupling phase field and viscoplasticity to study rafting in Ni-based superalloys. *Philosophical Magazine*, 90(1-4):375–404, 2010.

[26] M Cottura, Yann Le Bouar, Alphonse Finel, Benoit Appolaire, Kais Ammar, and Samuel Forest. A phase field model incorporating strain gradient viscoplasticity: application to rafting in Ni-base superalloys. *Journal of the Mechanics and Physics of Solids*, 60(7):1243–1256, 2012.

[27] Robert J Asaro and A Needleman. Overview no. 42 Texture development and strain hardening in rate dependent polycrystals. *Acta Metallurgica*, 33(6):923–953, 1985.

[28] Long-Qing Chen and Wei Yang. Computer simulation of the domain dynamics of a quenched system with a large number of nonconserved order parameters: The grain-growth kinetics. *Physical Review B*, 50(21):15752, 1994.

[29] Dana A Knoll and David E Keyes. Jacobian-free Newton–Krylov methods: a survey of approaches and applications. *Journal of Computational Physics*, 193(2):357–397, 2004.

[30] Derek Gaston, Chris Newman, Glen Hansen, and Damien Lebrun-Grandie. Moose: A parallel computational framework for coupled systems of nonlinear equations. *Nuclear Engineering and Design*, 239(10):1768–1778, 2009.

[31] Michael R Tonks, Derek Gaston, Paul C Millett, David Andrs, and Paul Talbot. An

object-oriented finite element framework for multiphysics phase field simulations. *Computational Materials Science*, 51(1):20–29, 2012.

[32] Mostafa Jamshidian, Prakash Thamburaja, and Timon Rabczuk. A continuum state variable theory to model the size-dependent surface energy of nanostructures. *Physical Chemistry Chemical Physics*, 17(38):25494–25498, 2015.

[33] M Jamshidian, P Thamburaja, and T Rabczuk. Modeling the effect of surface energy on stressed grain growth in cubic polycrystalline bodies. *Scripta Materialia*, 113:209–213, 2016.

[34] Michael Ortiz and EA Repetto. Nonconvex energy minimization and dislocation structures in ductile single crystals. *Journal of the Mechanics and Physics of Solids*, 47(2):397–462, 1999.

[35] JJ Mason, AJ Rosakis, and G Ravichandran. On the strain and strain rate dependence of the fraction of plastic work converted to heat: an experimental study using high speed infrared detectors and the Kolsky bar. *Mechanics of Materials*, 17(2):135–145, 1994.

[36] Geoffrey Ingram Taylor and H Quinney. The plastic distortion of metals. *Philosophical Transactions of the Royal Society of London. Series A, Containing Papers of a Mathematical or Physical Character*, 230:323–362, 1932.

[37] Michael Tonks, Paul Millett, Wei Cai, and Dieter Wolf. Analysis of the elastic strain energy driving force for grain boundary migration using phase field simulation. *Scripta Materialia*, 63(11):1049–1052, 2010.

[38] Michael Tonks and Paul Millett. Phase field simulations of elastic deformation-driven grain growth in 2D copper polycrystals. *Materials Science and Engineering: A*, 528(12):4086–4091, 2011.

[39] Gunter Gottstein and Lasar S Shvindlerman. *Grain boundary migration in metals: thermodynamics, kinetics, applications*. CRC press, 2009.

[40] M Jamshidian, Goangseup Zi, and T Rabczuk. Phase field modeling of ideal grain growth in a distorted microstructure. *Computational Materials Science*, 95:663–671, 2014.

[41] K Chockalingam, MR Tonks, JD Hales, DR Gaston, PC Millett, and Liangzhe Zhang. Crystal plasticity with Jacobian-Free Newton–Krylov. *Computational Mechanics*, 51(5):617–627, 2013.

[42] Michael Pernice and Homer F Walker. Nitsol: A newton iterative solver for nonlinear systems. *SIAM Journal on Scientific Computing*, 19(1):302–318, 1998.

[43] Youcef Saad and Martin H Schultz. GMRES: A generalized minimal residual algorithm for solving nonsymmetric linear systems. *SIAM Journal on scientific and statistical computing*, 7(3):856–869, 1986.

[44] B Schönfelder, D Wolf, SR Phillpot, and M Furtkamp. Molecular-dynamics method for the simulation of grain-boundary migration. *Interface Science*, 5(4):245–262, 1997.

[45] R Viswanathan and CL Bauer. Kinetics of grain boundary migration in copper bicrystals with [001] rotation axes. *Acta Metallurgica*, 21(8):1099–1109, 1973.

[46] Nele Moelans, Bart Blanpain, and Patrick Wollants. Quantitative analysis of grain boundary properties in a generalized phase field model for grain growth in anisotropic systems. *Physical Review B*, 78(2):024113, 2008.

[47] Yonggang Huang. *A User-material Subroutine Incroporating Single Crystal Plasticity in the ABAQUS Finite Element Program*. Harvard Univ., 1991.

[48] William F Hosford. *Mechanical behavior of materials*. Cambridge University Press, 2010.

[49] R Peierls. The size of a dislocation. *Proceedings of the Physical Society*, 52(1):34, 1940.

[50] FRN Nabarro. Dislocations in a simple cubic lattice. *Proceedings of the Physical Society*, 59(2):256, 1947.

[51] Marc A Meyers and Krishan Kumar Chawla. *Mechanical behavior of materials*, volume 2. Cambridge University Press Cambridge, 2009.

[52] UF Kocks. A statistical theory of flow stress and work-hardening. *Philosophical Magazine*, 13(123):541–566, 1966.

[53] M Verdier, I Groma, L Flandin, J Lendvai, Y Bréchet, and P Guyot. Dislocation densities and stored energy after cold rolling of Al-Mg alloys: Investigations by resistivity and differential scanning calorimetry. *Scripta Materialia*, 37(4):449–454, 1997.

[54] F Barlat, MV Glazov, JC Brem, and DJ Lege. A simple model for dislocation behavior, strain and strain rate hardening evolution in deforming aluminum alloys. *International Journal of Plasticity*, 18(7):919–939, 2002.

[55] E Hosseini and M Kazeminezhad. Dislocation structure and strength evolution of heavily deformed tantalum. *International Journal of Refractory Metals and Hard Materials*, 27(3):605–610, 2009.

[56] E Schafler, M Zehetbauer, and T Ungar. Measurement of screw and edge dislocation density by means of X-ray Bragg profile analysis. *Materials Science and Engineering: A*, 319:220–223, 2001.

[57] Elyas Rafiee, Mansour Farzam, Mohammad Ali Golozar, and Ali Ashrafi. An investigation on dislocation density in cold-rolled copper using electrochemical impedance spectroscopy. *International Scholarly Research Notices*, 2013, 2013.

[58] JE Bailey. The dislocation density, flow stress and stored energy in deformed polycrystalline copper. *Philosophical Magazine*, 8(86):223–236, 1963.

[59] RO Williams. The stored energy of copper deformed at 24 °C. *Acta Metallurgica*, 13(3):163–168, 1965.

[60] JE Bailey and PB Hirsch. The recrystallization process in some polycrystalline metals. In *Proceedings of the Royal Society of London A: Mathematical, Physical and Engineering Sciences*, volume 267, pages 11–30. The Royal Society, 1962.

[61] Taku Sakai, Andrey Belyakov, Rustam Kaibyshev, Hiromi Miura, and John J Jonas. Dynamic and post-dynamic recrystallization under hot, cold and severe plastic deformation conditions. *Progress in Materials Science*, 60:130–207, 2014.

[62] HJ McQueen and S Bergerson. Dynamic recrystallization of copper during hot torsion. *Metal Science*, 6(1):25–29, 1972.

[63] Anthony Rollett, FJ Humphreys, Gregory S Rohrer, and M Hatherly. *Recrystallization and related annealing phenomena*. Elsevier, 2004.

[64] G Mohamed and B Bacroix. Role of stored energy in static recrystallization of cold rolled copper single and multicrystals. *Acta Materialia*, 48(13):3295–3302, 2000.

[65] G Gottstein, D Zabardjadi, and H Mecking. Dynamic recrystallization in tension-deformed copper single crystals. *Metal Science*, 13(3-4):223–227, 1979.

Chapter 4 : Nucleation Kinetics in Al-Sm Metallic Glasses

In this chapter, the isothermal nucleation kinetics in Al-Sm MGs with low Sm concentrations (x_{Sm}) was studied using MD simulations in order to calculate time−temperature−transformation curves [1]. The average delay time of Al nanocrystal nucleation was found to increase exponentially with x_{Sm}, whereas the estimated critical cooling rate necessary to avoid crystallization decreases exponentially with x_{Sm}. Sm solutes were found to suppress Al nucleation by increasing the attachment barrier and therefore by reducing the attachment frequency. The analysis shows that the attachment of Al to the evolving nucleus has the same characteristics as Al diffusion within the amorphous matrix and they both take place heterogeneously via collective movement of a group of Al atoms.

4.1 Introduction

MGs have attracted a growing interest since they were first reported in 1960 by Duwez *et al.* [2], due to their superior mechanical properties, better corrosion resistance and formability [3–6], as compared to their crystalline counterparts. In particular, Al-based MGs have a lower density and higher specific strength, and therefore have become promising candidates for applications as structural components [7, 8]. Rapidly quenched Al-based MGs are usually characterized by a primary crystallization reaction upon heating which produces a high density of FCC Al nanocrystals and consequently enhances the mechanical properties evidently [9–11]. For instance, it has been reported that the fracture strength of MGs with such nanocrystalline dispersions is 20 to 120% higher than that of the pure amorphous phase alloys with the same compositions [12–14].

The primary crystallization is of significant importance in understanding glass formation of alloys and there are two aspects of the primary crystallization that are still not well understood. One of them concerns unknown mechanisms underlying the effect of micro-alloying on the glass forming ability (GFA) of Al-based and other systems. This effect is known to be significant [15, 16]. The second issue that needs to be elucidated is the nucleation kinetics in the primary crystallization [17], especially on the atomic level. To address these issues, here MD simulations were carried out to investigate the isothermal nucleation reactions of Al-Sm binary MG. This glass has been reported in experiments to undergo the primary crystallization during annealing [17–20]. In this study, a particular attention is devoted to Sm effect on the nucleation kinetics and the atomic-level mechanism controlling the nucleation attachment. Simulation of the crystal growth after the nucleation is outside the scope of this study.

4.2 Simulation methods

4.2.1 MD simulation of isothermal nucleation reaction

MD simulations are performed using the LAMMPS simulation package [21], based on a Finnis-Sinclair type semi-empirical potential developed for Al-Sm alloy by Mendelev *et al.* [22]. This potential is able to reproduce the basic pure Al properties and formation energies of Al-Sm crystal phases, as well as predict the realistic liquid/glass structure of Al-Sm alloy up to 10% Sm in a large temperature range [22]. Therefore, it is suitable for simulating the solidification/vitrification in Al-Sm system at low Sm concentrations. Bokas *et al.* [23] have successfully applied the same potential to study the icosahedral-ordering in the rapid solidification of Al-Sm alloys.

In the simulations, a $9 \times 9 \times 9$ nm^3 simulation box was used, that contained a total of 42,592 atoms, and the periodic BCs were enforced in all three Cartesian directions. An isothermal-isobaric (NPT) ensemble is used in all the simulations and the temperature

and pressure are controlled with the Nose-Hoover thermostat and barostat, respectively. The nominal pressure is maintained to 0 GPa. The Al-Sm sample is prepared by randomly substituting a certain fraction of Al atoms with Sm atoms in the solid state. The sample is first heated to 2000 K in order to melt it, then it is equilibrated at this high temperature for 300 ps, followed by a rapid cooling (4×10^{13} K/s) to 10 K to let the system vitrify. After an additional equilibration at 10 K, the as-quenched system is reheated quickly to the annealing temperature T_{anneal} for an isothermal nucleation reaction. The temperature history and the snapshots from simulations of heating, quenching and annealing are shown in Fig. 4.1. In the MD simulations, it is observed that the FCC Al crystal nucleates directly from the glassy state without the formation of any intermediate structures. This observation is consistent with those from the atomistic simulations of solidification of pure Al [24, 25], and is distinct from the reported nucleation mechanism in Lennard-Jones fluids and some metallic systems where a metastable BCC structure acts as the precursor for nucleation of the stable FCC phase [26–28].

The delay time τ for the first nucleation event since the start of the annealing process is recorded in every annealing simulation. An adaptive CNA method [29] was used for the structure identification, which examines the local environment to classify each atom as different structural types such as FCC, BCC, HCP or amorphous structure. Details of the method to determine the delay time can be found in Sec. 4.2.2.

In order to understand the Sm effect on nucleation, the nucleation data was fitted with the classical nucleation theory (CNT). From these fits the nucleation kinetic barriers were determined and then compared with Al/Sm diffusion energy barriers in order to identify the controlling process in the Al nucleation kinetics. The calculation of diffusion coefficients and diffusion barriers can be found in Sec. 4.2.3. The details are reported in Secs. 4.3.2 and 4.3.3. Finally, the mechanisms participating in the nucleation event were identified; these mechanisms are compared to those governing Al diffusion in Al-Sm MG and are discussed in Sec. 4.3.4.

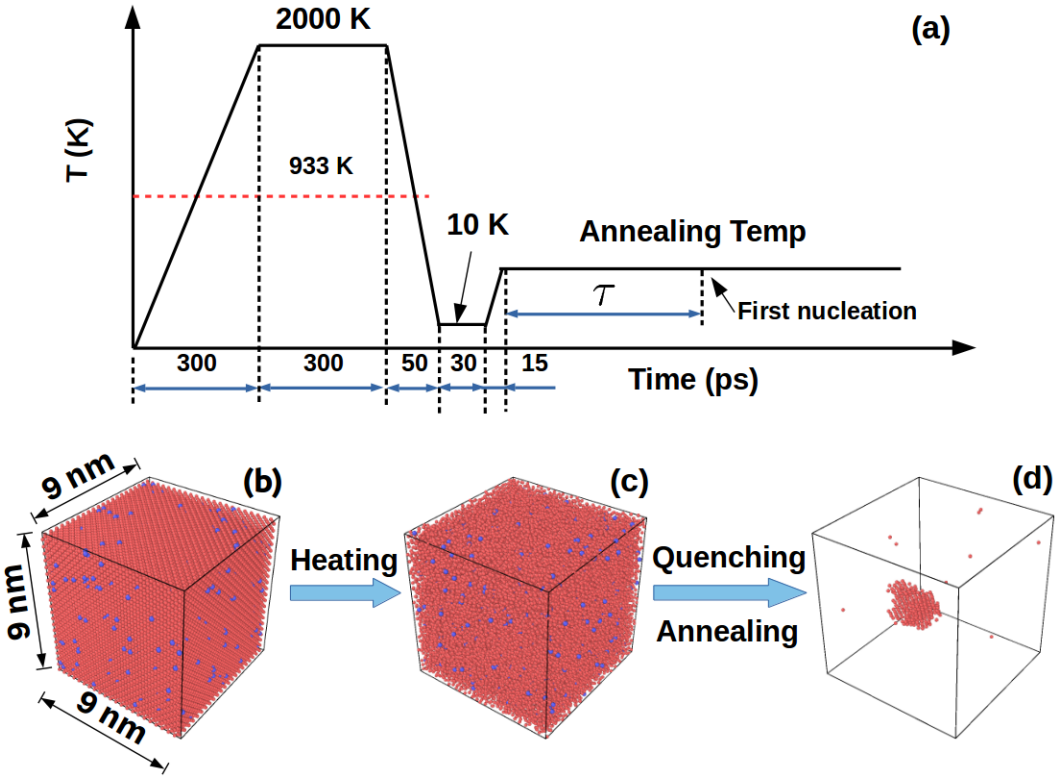

Fig. 4.1: (Color online) (a) The temperature history of Al-Sm samples. Delay time τ of the first nucleation is recorded in each simulation. (b)-(d) Snapshots of nucleation simulation process. The red and blue atoms represent Al and Sm, respectively. Only Al FCC atoms are shown in (d).

One should note that, in this chapter, the term "nucleation barrier" is avoided since it is ambiguous and does not distinguish the nucleation free energy barrier ΔG^* from the nucleation kinetic barrier Q. ΔG^* is the free energy cost associated with the formation of a critical nucleus of a new phase, whereas Q is the energy barrier per atom that needs to be overcome in the process of atomic attachment to nuclei.

4.2.2 Determination of delay time

According to classical nucleation theory (CNT) [30, 31], the nucleation delay time τ is the time required by the new phase cluster to grow and overcome the nucleation energy barrier. In experiments, τ is usually determined by fitting the measured number of nuclei as a function of annealing time. This approach gives the average delay time over a number of nuclei. Here, however, τ is only recorded for the first nucleation event, due to the temporal and spatial scale limitations of MD simulations.

There are two different approaches to determine τ of the first nucleus in the simulated samples. The first approach is to treat τ as the time the first nucleus takes to reach the critical nucleus radius r_c. This approach is accurate once the exact value of r_c is known and therefore it requires that r_c is determined first. To determine a single r_c at each temperature and composition from MD simulation, one typically needs to embed clusters of different sizes into an amorphous matrix to observe whether they would grow or shrink at that annealing temperature. For each size of the embedded cluster, one should perform multiple independent simulations to obtain statistically meaningful results. Consequently, it becomes computationally expensive to determine all the r_c for multiple temperatures and compositions. In addition, the embedded cluster is spherical, while the true nucleus usually has preferred surface planes. Since the effect of the cluster morphology on r_c is not considered in this approach, it may lead to some inaccuracies in the estimates of r_c as well as perhaps τ. The second approach to determine τ is simply based on the direct observation of the occurrence of the first nucleus. In the simulations the majority of time τ is spent on the formation of pre-nuclei and their sluggish growth. However, once the nucleus forms, it is found to grow at a relatively high rate. This transition of growth rate is used as a criterion to estimate the nucleation delay time τ.

In order to compare the two aforementioned approaches, the delay time τ are determined from both methods for different Sm concentrations x_{Sm} at a fixed fraction (0.95)

of glass transition temperatures T_g. The results are shown in Fig. 4.2, where one can see that the two approaches produce comparable delay times. Therefore, for the sake of computational efficiency all the delay times in the main text are determined using the second approach, i.e., through the direct observation of occurrence of the first nucleus.

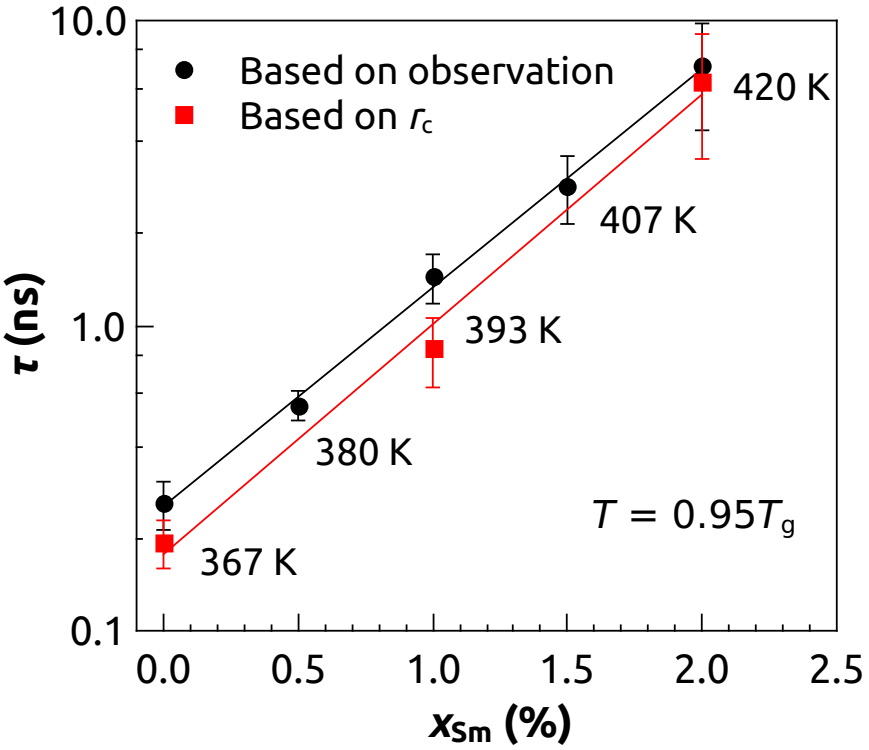

Fig. 4.2: (Color online) Comparison of nucleation delay time τ determined by observation and critical nucleus radius r_c. The annealing temperatures T are set to $0.95\,T_g$ and are shown along the fitted lines, where T_g is the respective annealing temperature for any composition x_{Sm}. The error bar represents the standard deviation of τ from 10 independent simulations.

4.2.3 Calculation of diffusion energy barriers

The diffusion coefficient D is calculated as $D = \langle |\mathbf{r}(t) - \mathbf{r}(0)|^2 \rangle / 6t$, where $\mathbf{r}$ is the position of a diffusing atom and t is the time interval measured during annealing before the

occurrence of the first nucleation event. The brackets $\langle\rangle$ represent an ensemble average, which is calculated as an average over all atoms of a given species in the system. Considering that MGs often exhibit temperature dependent diffusion energy barriers [32, 33], the diffusion coefficients are calculated for ≥ 1.0 at.% Sm in a wide temperature range below T_{nose}. One exception is the pure Al system where the nucleation delay time for temperatures $T > 360$ K is too short for a steady state (and therefore for a statistically meaningful) mean squared displacements to be obtained. Therefore, for pure Al system the diffusion coefficient is calculated only in a lower temperature range.

The Arrhenius equation, $D = D_0 \exp(-E/k_B T)$, is assumed to be followed, where D_0 and E are diffusion prefactor and energy barrier, respectively. D as a function of the inverse temperature and the Arrhenius fitting lines are shown in Fig. 4.3. The values of D_0 and E are obtained from the Arrhenius fitting and are listed in Table 4.1. From Fig. 4.3 one can see that the diffusion coefficients of both Al and Sm decrease and their energy barriers increase with increasing Sm concentration. This analysis suggests that Sm addition leads to a sluggish atomic mobility and to an improved structural stability of Al-Sm MG.

Table 4.1: Fitted values of diffusion prefactor D_0 and energy barrier E.

x_{Sm}(at.%)	D_0 (m^2/s)		E (eV)	
	Al	Sm	Al	Sm
0.0	2.6×10^{-8}		0.261	
1.0	4.8×10^{-6}	1.5×10^{-5}	0.461	0.574
2.0	4.3×10^{-5}	1.8×10^{-4}	0.579	0.746
2.5	5.3×10^{-5}	3.1×10^{-3}	0.621	0.941
3.0	1.9×10^{-4}	5.5×10^{-2}	0.666	1.044

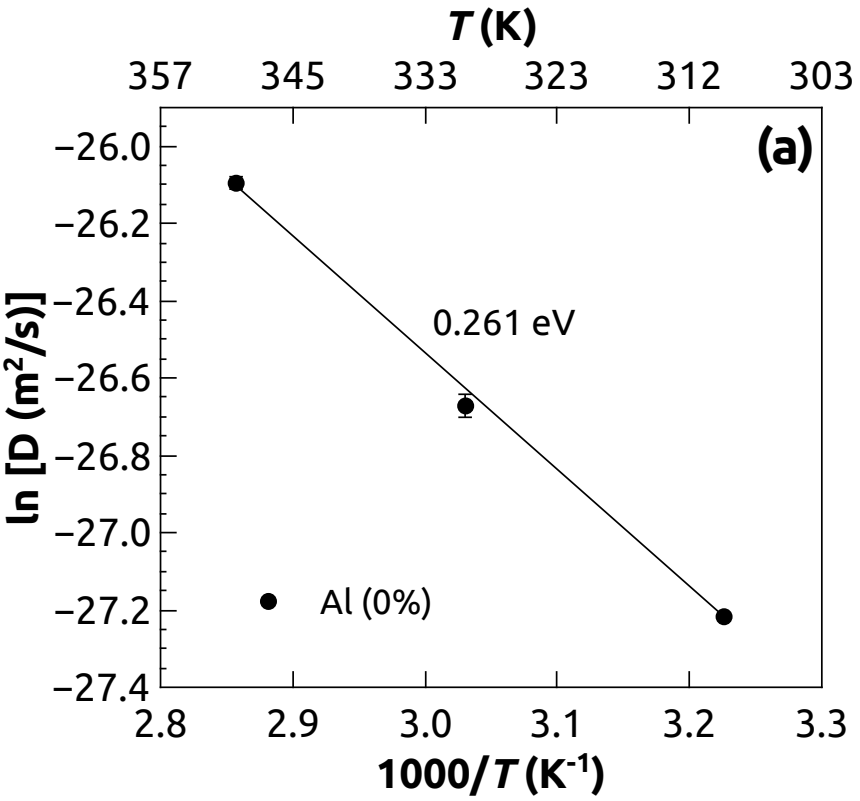
T (K)
357
345
333
323
312
303
(a)
0.261 eV
Al (0%)
ln [D (m²/s)]
−26.0
−26.2
−26.4
−26.6
−26.8
−27.0
−27.2
−27.4
2.8
2.9
3.0
3.1
3.2
3.3
1000/T (K⁻¹)

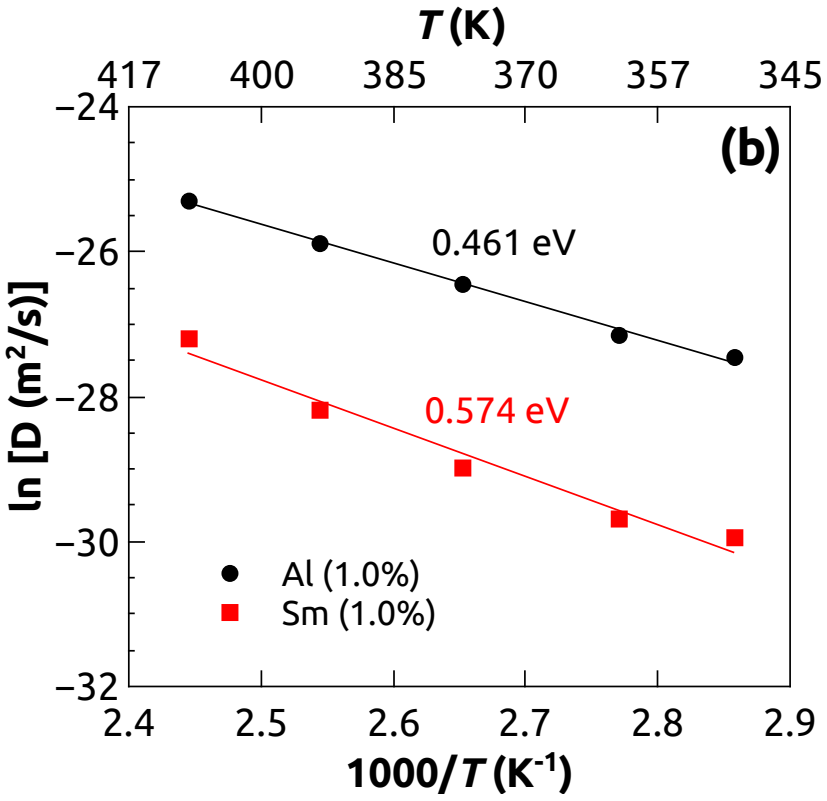
T (K)
417
400
385
370
357
345
(b)
0.461 eV
0.574 eV
Al (1.0%)
Sm (1.0%)
ln [D (m²/s)]
−24
−26
−28
−30
−32
2.4
2.5
2.6
2.7
2.8
2.9
1000/T (K⁻¹)

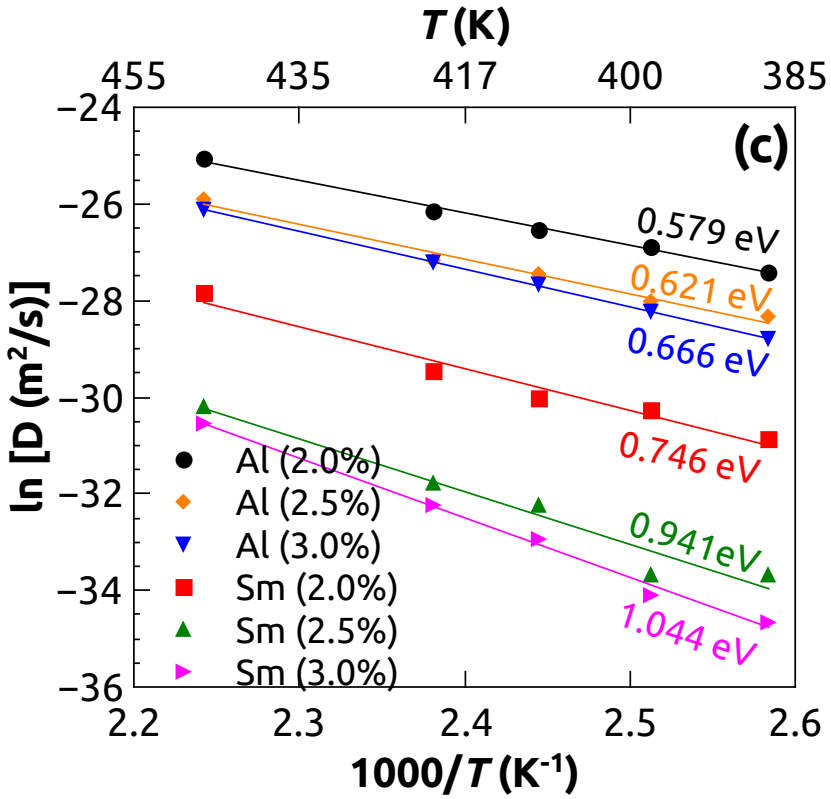

Fig. 4.3: (Color online) Diffusion coefficient D as a function of inverse temperature and fits to the data (lines) based on the Arrhenius relations for (a) x_{Sm} = 0.0 at.%, (b) x_{Sm} = 1.0 at.% and (c) x_{Sm} = 2.0, 2.5 and 3.0 at.%, respectively.

4.3 Results

4.3.1 Time−temperature−transformation (TTT) curves

Isothermal nucleation reactions were simulated for Al-Sm MGs with four Sm concentrations (x_{Sm} = 0.0, 1.0, 2.0 and 3.0 at.%) at different T_{anneal}. The time step was set to 10 fs for 3.0 at.% and 2 fs otherwise. 10 independent simulations were run for each composition and each temperature. The average τ and the corresponding error bars are plotted in Fig. 4.4a. The measured delay times for different temperatures comprise the

TTT curve that marks the onset of the crystallization transformation for each concentration. Fig. 4.4a shows that addition of Sm shifts the TTT curve towards the larger value of τ and therefore it retards the primary crystallization and enhances GFA of Al-Sm MGs. The "nose" temperatures (T_{nose}) of the TTT curves are in the range of $0.48\,T_{\mathrm{m}}$ - $0.54\,T_{\mathrm{m}}$, where T_{m} is the melting temperature (933 K) of pure Al. The cooling process starts at T_{m} and the temperature decreases linearly with time t, i.e., $T = 933\,\mathrm{K} - R_{\mathrm{c}}\,t$. The corresponding continuous cooling curves tangential to the TTT curves at the "nose" temperature are also shown in Fig. 4.4a. Here, R_{c} is the estimated critical cooling rate.

To calculate the steady state nucleation rate J_{s}, it is assumed that the instantaneous nucleation rate at $t = \tau$ is approximately $1/(V\tau)$, where V is the system volume. Unfortunately, this assumption cannot be verified in this work because it is difficult to obtain the statistics of delay times of the initial a few (at least two) nuclei due to the time scale limitations of MD simulations. Plugging in the nucleation rate $1/(V\tau)$ at $t = \tau$ into the instantaneous nucleation rate equation $J(t) = J_{\mathrm{s}} \exp(-\tau/t)$, one can obtain the estimated steady state nucleation rate $J_{\mathrm{s}} \approx e/(V\tau)$. Fig. 4.4b shows the estimated J_{s} at different temperatures, which (by construction) shows the opposite trend to the delay time with temperature and Sm concentration as in Fig. 4.4a.

To determine quantitatively the effect of Sm on the nucleation delay time τ, we anneal the systems at a fixed T/T_{g} ratio of 0.95. Here the glass transition temperature, T_{g}, is calculated with the method described in Refs. [22] and [34], and the calculated values of T_{g} are shown in Table 4.2. The ratio of 0.95 is chosen because typical annealing experiments of Al-based MG use similar ratios [19, 20]. τ as a function of x_{Sm} is plotted in Fig. 4.5a. Apart from the previously mentioned four Sm concentrations, simulations with 0.5 at.% and 1.5 at.% concentrations are also performed and reported here. The increasing trend of τ with x_{Sm} can be fitted with an exponential law: $\tau = C{\cdot}10^{k x_{\mathrm{Sm}}}$, where $C = 0.228$ ns and $k = 0.787$. The mechanism underlying this significant effect of Sm on τ will be discussed in Secs. 4.3.2 and 4.3.3. The fact that the error bar of τ

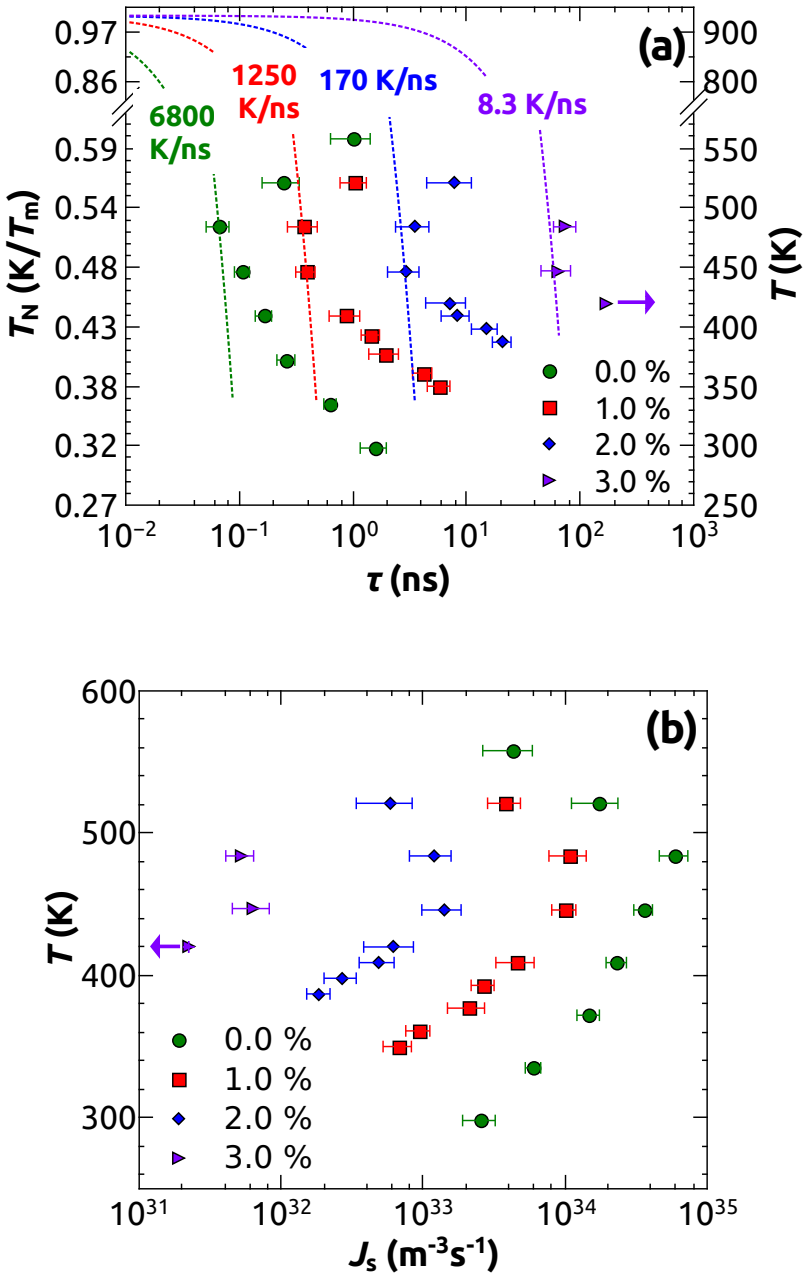

Fig. 4.4: (Color online) (a) TTT curves for x_{Sm} = 0.0 at.% (green circle), 1.0 at.% (red rectangle), 2.0 at.% (blue diamond) and 3.0 at.% (violet right triangle). T_N represents the homologous temperature T/T_m. The standard deviation is shown as the error bar. The continuous cooling curves are plotted as dashed lines and the values of R_c are indicated. (b) The steady state nucleation rate J_s at different temperatures for different Sm concentrations.

(note the logarithmic scale) increases with x_{Sm} implies a more stochastic nature of the nucleation process at higher Sm concentrations.

Table 4.2: Calculated T_g and T_{anneal} ($T_{anneal} = 0.95\,T_g$).

x_{Sm}(at.%)	T_g(K)	T_{anneal}(K)
0.0	386	367
0.5	400	380
1.0	414	393
1.5	428	407
2.0	442	420
3.0	471	447

The critical cooling rate R_c as a function of x_{Sm} is plotted in Fig. 4.5b. It is found that the decay of R_c with increasing x_{Sm} is well approximated by an exponential function, i.e., $R_c = C' \cdot 10^{-k' x_{Sm}}$, where $C' = (9.9 \pm 3.8) \times 10^{12}$ K/s and $k' = 0.96 \pm 0.09$. Our predictions are in a good agreement with available literature data. For instance, MD simulations by Hou *et al.* [35] with an embedded atom method interatomic potential [36] have shown that R_c for pure Al is within the range of 4.0×10^{12} - 1.0×10^{13} K/s. This result is consistent with that of 6.8×10^{12} K/s found in our work. On the other hand, if the exponential relation determined in our simulations is extrapolated to higher x_{Sm}, R_c is predicted to be 2.24×10^4 - 1.59×10^6 K/s for $x_{Sm} = 8.0$ at.%, which corresponds to the composition of a well-known marginal glass former [10, 11]. This predicted range is consistent with experimental data [37, 38], which showed that general Al-based MGs have R_c in the range of 10^4 - 10^6 K/s.

4.3.2 Kinetics-controlled nucleation

In order to understand the Sm effect on the nucleation kinetics, our simulation data was evaluated in the light of the CNT for homogeneous nucleation. From CNT, the steady-

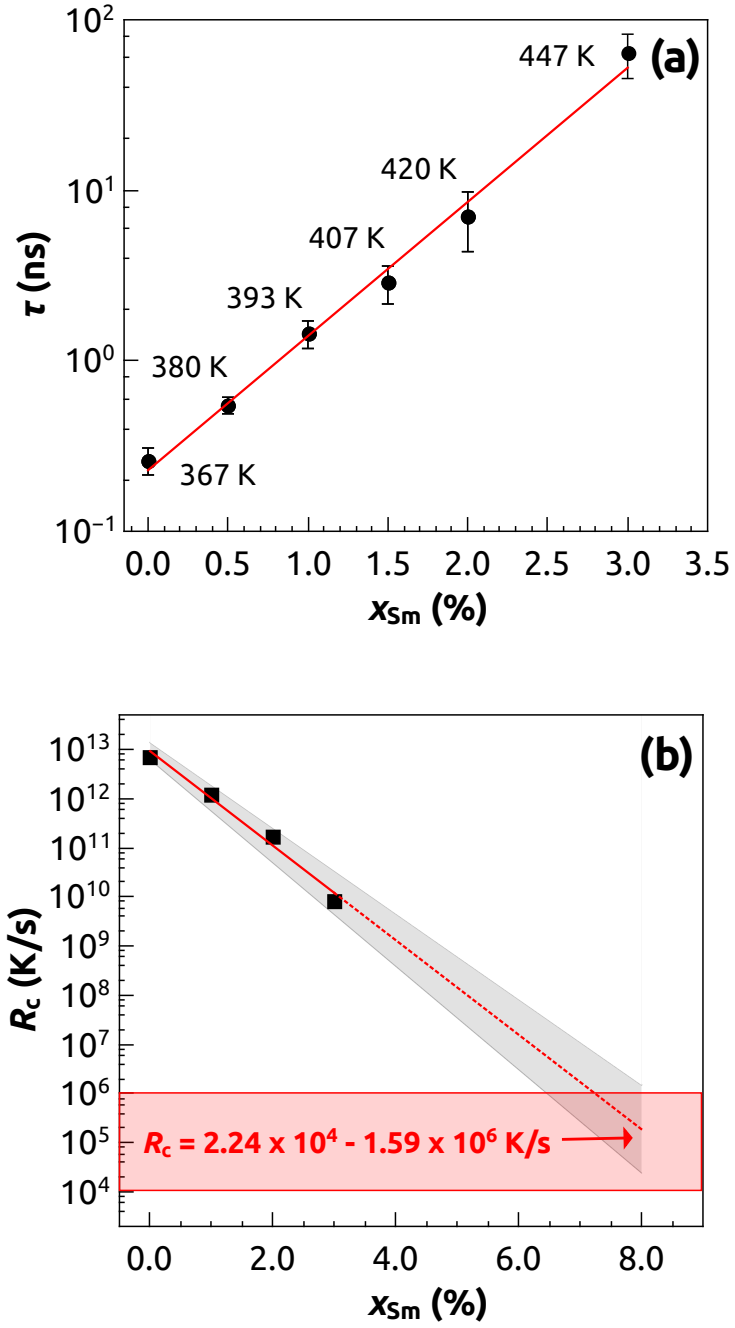

Fig. 4.5: (Color online) (a) Delay time τ as a function of x_{Sm} at 0.95 T_{g}. The solid line is the exponential fitting. (b) Critical cooling rate R_{c} as a function of x_{Sm}. The data is fitted with an exponential relation and extrapolated to higher x_{Sm}. The gray and red areas represent the fitting error bar and the reported range of R_{c} for marginal glass formers, respectively. The predicted range of R_{c} for $x_{\mathrm{Sm}} = 8.0$ at.% is 2.2×10^4 - 1.6×10^6 K/s.

state nucleation rate J_s, defined as the number of nuclei in unit volume per unit time, can be written as [30, 31]

$$J_s = \omega^* Z N^*, \tag{4.1}$$

where ω^*, Z and N^* are the attachment frequency of monomers to the critical nucleus, the Zeldovich factor, and the equilibrium concentration of critical nuclei, respectively. ω^* and N^* represent the kinetic and thermodynamic contributions, respectively, to the overall nucleation rate, and they can be calculated as

$$\omega^* = AC\nu\lambda \exp\left(-\frac{Q}{k_B T}\right), \tag{4.2}$$

$$N^* = N_1 \exp\left(-\frac{\Delta G^*}{k_B T}\right). \tag{4.3}$$

Here, A is the nucleus surface area, C is the concentration expressed in number of monomers per volume, ν is a frequency factor, λ is the mean free path of Al in MG, N_1 is Al monomer concentration, T is temperature, k_B is the Boltzmann constant, Q is the nucleation kinetic barrier, and ΔG^* is the free energy barrier determined by nucleation driving force ΔG_v and interfacial energy γ [31]. For spherical nuclei, $\Delta G^* = 16\pi\gamma^3/(3\Delta G_v^2)$ [39].

Nucleation is controlled by thermodynamics at shallow supercoolings ($T > T_{nose}$) due to the smaller nucleation driving force and it is controlled by kinetics at deep supercoolings ($T < T_{nose}$) due to the slower atomic mobility. The balance of these thermodynamic and kinetic factors results in the highest nucleation rate at T_{nose}. In our simulations a number of sub-critical Al FCC clusters have been observed at deep supercoolings, and their formation is due to the high nucleation driving force. However, these sub-critical clusters grow very slowly and very few of them have a chance to grow to

the super-critical size, indicating a sluggish nucleus attachment kinetics and resulting in the prolonged delay time at deep supercoolings. Therefore, at $T < T_{\text{nose}}$, the term $\exp(-Q/k_{\text{B}}T)$ dominates, and Eq. (4.1) can be rewritten as $J_{\text{s}} = K\exp(-Q/k_{\text{B}}T)$ with K as approximately constant. Since the delay time τ is inversely proportional to J_{s} [40], therefore, one can write $\tau \propto \exp(Q/k_{\text{B}}T)$.

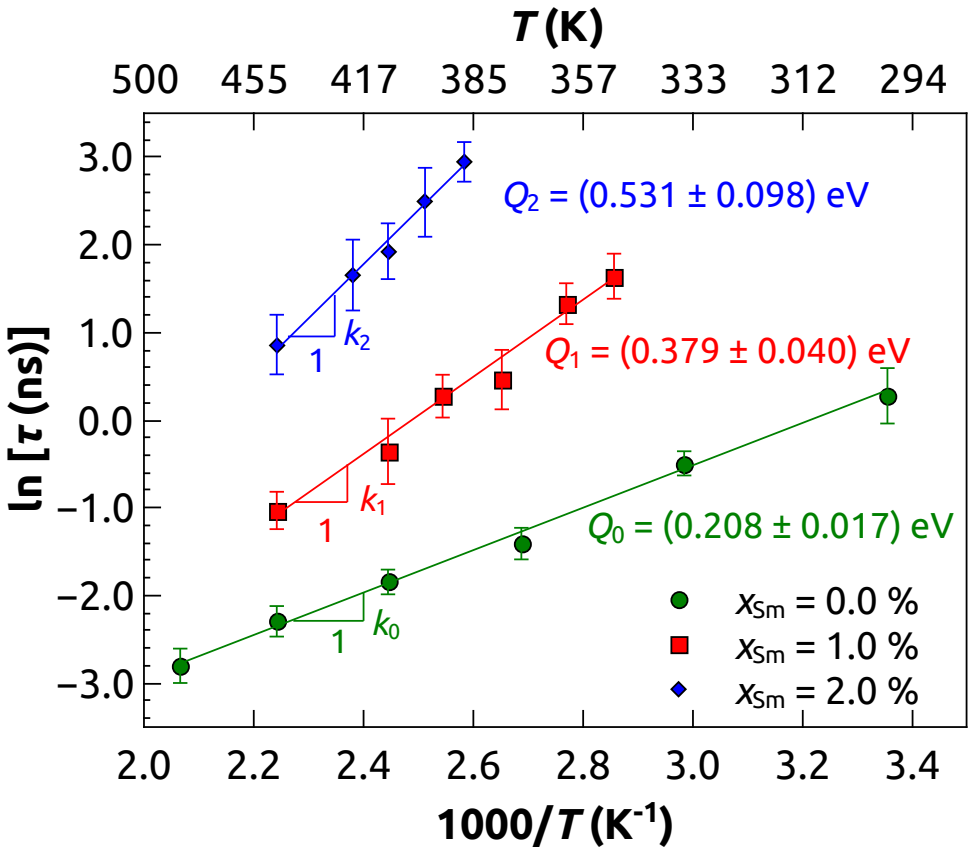

Fig. 4.6: (Color online) $\ln(\tau)$ vs. $1/T$ for $T < T_{\text{nose}}$. The solid lines are the weighted exponential fitting of delay time τ. The nucleation kinetic barrier Q_{i} is calculated as $Q_{\text{i}} = k_{\text{i}}\, k_{\text{B}}$, where k_{i} represents the slope of the fitting line.

Fig. 4.6 plots $\ln(\tau)$ vs. $1/T$ in the temperature range of $T < T_{\text{nose}}$, along with the exponential fitting lines. The nucleation kinetic barrier Q_{i} is calculated as $Q_{\text{i}} = k_{\text{i}}\, k_{\text{B}}$, where k_{i} is the slope of the fitting line. The values of Q for $x_{\text{Sm}} = 0.0$, 1.0 and 2.0 at.% are

0.208 ± 0.017, 0.379 ± 0.040 and 0.531 ± 0.098 eV, respectively. Note that Q for 2.0 at.% Sm concentration has a large error bar, because the long nucleation delay time restricts the temperature range that can be studied for this concentration. Clearly, Sm additions raise the nucleation kinetic barrier Q and therefore they significantly reduce the Al attachment rate ω^* to nuclei. As a result, the nucleation delay time increases exponentially with increasing Sm as shown in Fig. 4.5a.

4.3.3 Rate-limiting process in nucleation

Having shown that Sm solutes remarkably reduce the frequency of Al attachment to nuclei, an interesting question that arises is what is the controlling process in Al nucleation kinetics. It has been shown that the atomic transport in nucleation can be governed either by bulk diffusion or by interface attachment, depending on specific circumstances [41–43].

In order to discover the process controlling the development of Al nucleus, we calculated the diffusion energy barriers (E_{Al} and E_{Sm} for Al and Sm, respectively) and compared them with the nucleation attachment barrier Q. E_{Al} and E_{Sm} were obtained by fitting the diffusion coefficients determined during annealing before any nucleation took place (see Sec. 4.2.3 for more details). The nucleation kinetic barrier (Q) and the diffusion energy barriers (E_{Al} and E_{Sm}) are plotted together in Fig. 4.7 for comparison. The fact that the nucleation kinetic barrier Q is smaller than E_{Sm} indicates that the attachment frequency is controlled by a process that is faster than Sm bulk diffusion. There is a relatively good overall agreement between Q and E_{Al}, which in principle might mean that Al diffusion is the rate controlling process. However, this is not a valid explanation because the Sm concentration is very low and the prevalence of Al atoms near nuclei makes the long-distance diffusion of Al unnecessary for nucleation. This analysis implies that the attachment frequency is interface-controlled and Al atomic transfer across the interface (constituting an "attachment" event) is the rate limiting process in the composition range

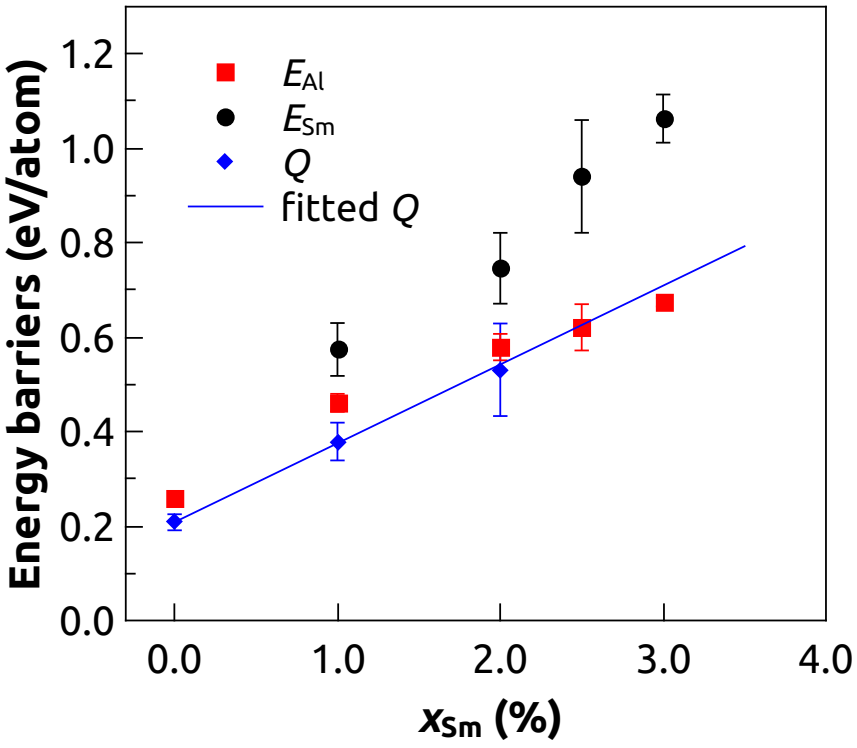

Fig. 4.7: (Color online) Nucleation kinetic barrier (Q) and diffusion energy barriers (E_{Al} and E_{Sm}). The sizes of the error bars represent standard deviations in the data.

considered in this study.

It is interesting that the interface attachment of Al to a nucleus would have a comparable energy barrier to the barrier for Al diffusion through the bulk MG. In order to shed light on this observation, the specific mechanisms underlying both Al diffusion and attachment will be examined and compared to each other in the following section.

4.3.4 Mechanisms for diffusion and nucleation attachment

Unlike crystalline metals where diffusion often occurs by means of single-atom jumps via a vacancy or interstitial mechanism, MD simulations have shown that diffusion in many MGs takes place in a heterogeneous manner (i.e., in a given time interval there are diffusing and non-diffusing regions of the structure) and that diffusion occurs through collective movement of a chain or ring of atoms [44, 45]. Here, first a quantitative analysis

was conducted for the simulated samples to confirm that Al diffusion in our system follows the same collective pattern as reported in many other MGs [44, 45]. Then it will be shown that during nucleation, attachment of Al atoms to nuclei is also heterogeneous and involves a collective motion of atoms.

4.3.4.1 Al diffusion mechanism

To elucidate the diffusion mechanism in MGs, it is first necessary to identify the diffusing atoms (DAs) and the diffusion events. Here, the DAs are defined as those which perform displacements larger than a cut-off d_c within a time window Δt. All the DAs identified in this section are Al atoms, as Sm atoms displace too slowly and are not diffusing by the cut-off definition. The fraction of DAs among all the atoms in the sample is usually smaller than a few percent and it decreases with increasing d_c and decreasing Δt. Fig. 4.8 shows the number N_d and fraction f_d of DAs for different displacement cut-offs d_c and time windows Δt. As expected, N_d and f_d decrease with increasing d_c and decreasing Δt. f_d is usually lower than a few percent. The small fraction of DAs indicates that majority of atoms only perform localized vibrations.

Once the DAs have been identified, the spatial correlations among these atoms are analyzed to address the question of whether Al diffusion is heterogeneous. For this purpose, the nearest neighbor analysis (NNA) and reduced number density analysis are employed on all the DAs.

In NNA, the average distance d_{nn} between the nearest neighboring DAs is first calculated. The nearest neighbor index (NNI) is then defined as d_{nn}/d_{ran}, where $d_{ran} = 0.55396\, N_v^{-\frac{1}{3}}$ is the theoretical average nearest neighbor distance for the same number of randomly distributed atoms [46]. From NNI one can learn whether the DAs are clustered (NNI < 1), randomly distributed (NNI ≈ 1), or more uniformly distributed than random (NNI > 1). Fig. 4.9a shows an example of a calculated NNI for a relaxed system with x_{Sm} = 2.0 at.% and $T = 0.95\, T_g$ before nucleation occurs. Since NNI < 1, this means

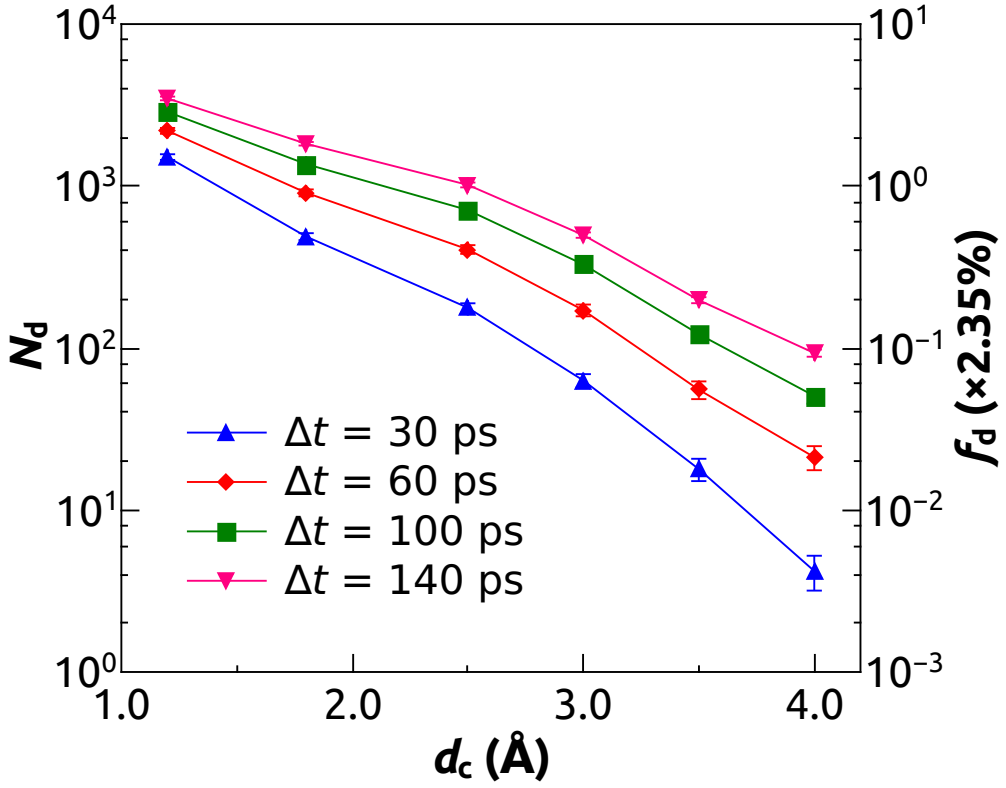

Fig. 4.8: (Color online) Number N_d and fraction f_d of DAs as functions of the displacement cut-off d_c and the time window Δt for a relaxed system with x_{Sm} = 2.0 at.% and $T = 0.95\,T_g$.

the DAs tend to cluster and they perform diffusing displacements collectively. Different choices of Δt lead to qualitatively the same results. Fig. 4.9b presents a 2D view of DAs for $d_c = 2.5$ Å and $\Delta t = 100$ ps. This analysis shows that the distribution of DAs is highly heterogeneous and that DAs form chains or rings, confirming the cooperative nature of Al diffusion.

In addition to NNA, the reduced number density ρ/ρ_0 of DAs was also calculated. Here, ρ is the number density of DAs around the central DA and is calculated as $\rho = N(r)/(\frac{4}{3}\pi r^3)$, where $N(r)$ is the DA count within a distance r from the central DA. ρ_0 is the average number density of DAs in the system. Fig. 4.9c shows ρ/ρ_0 of DAs for different Sm concentrations at $T = 0.95\,T_g$ using $d_c = 2.5$ Å and $\Delta t = 60$ ps. It is

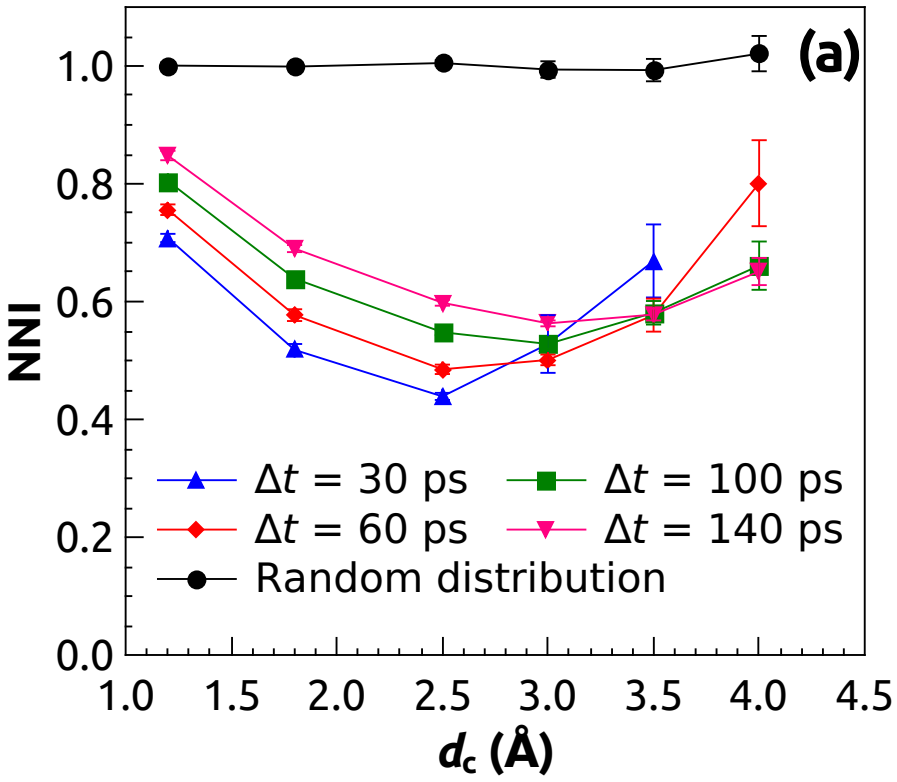
(a)
NNI
1.0
0.8
0.6
0.4
0.2
0.0
1.0
1.5
2.0
2.5
3.0
3.5
4.0
4.5
d_c (Å)
Δt = 30 ps
Δt = 100 ps
Δt = 60 ps
Δt = 140 ps
Random distribution

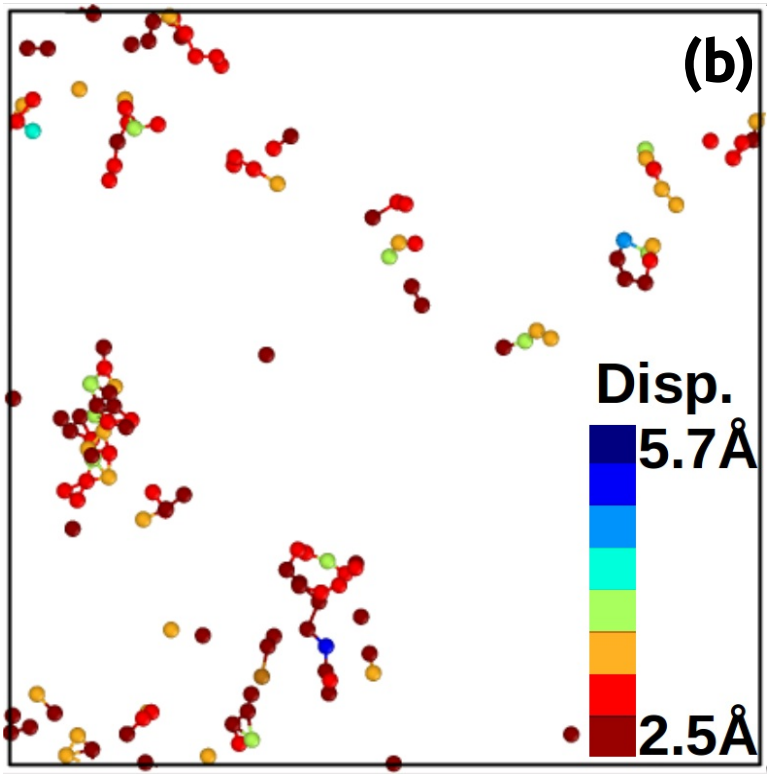
(b)
Disp.
5.7Å
2.5Å

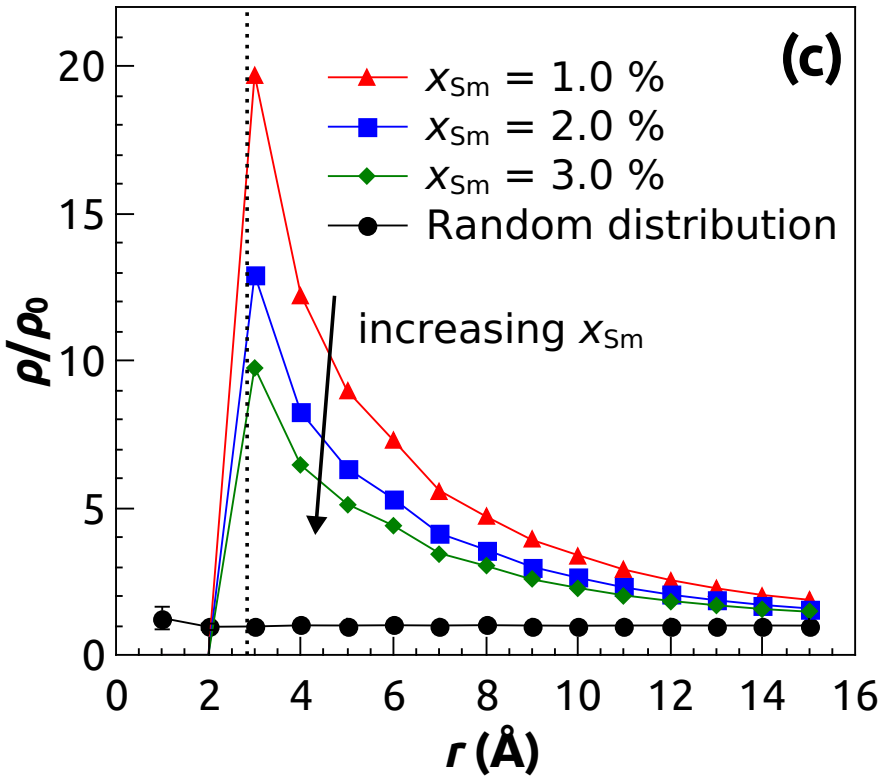

Fig. 4.9: (Color online) (a) NNI of DAs as a function of displacement cut-off d_c and time window Δt. (b) A 1-nm-thick 2D slice of the DAs for $d_c = 2.5$ Å and $\Delta t = 100$ ps. The color represents displacement magnitude. (c) Reduced number density of DAs around the central DA. Here $d_c = 2.5$ Å and $\Delta t = 60$ ps are used to define diffusing events. The vertical dashed line represents the nearest Al-Al distance (2.8 Å) in the system. For comparison, in (a) and (c), respectively, we also plot NNI and the reduced number density for randomly distributed atoms with the same number of atoms as DAs in our Al-Sm samples. In (c) the data corresponds to $\Delta t = 60$ ps.

evident that ρ/ρ_0 increases with decreasing r and reaches a maximum value at around the nearest Al-Al distance, which indicates that the DAs are prone to become direct nearest neighbors of each other. This is consistent with the observation in Fig. 4.9b. The decrease of ρ/ρ_0 with increasing Sm concentration suggests the decreasing size of the DA-cluster. This trend is attributed to the reduced size of the liquidlike diffusion channels with increasing Sm concentration, as discussed later in this section.

To elucidate further the collective nature of DAs, their spatial correlations are analyzed with the icosahedral Voronoi polyhedra (ICO VP) and Sm atoms. The motivation for this analysis is that the concentration of ICO VPs has been previously argued to be correlated with the GFA of an alloy [47, 48]. In this case, the ICO VPs are identified by applying the Voronoi tessellation technique [49] and then grouped based on their Voronoi indices [23]. The concentrations of the center atoms of ICO-like VPs and Sm atoms within a distance r from any DA are calculated and plotted in figs. 4.10a and 4.10b, respectively. According to Fig. 4.10a there are fewer ICO-like VPs near DAs, implying that DAs tend to avoid ICO VPs. This observation is consistent with findings previously reported in literature. Specifically, Zhang *et al.* [45] reported that the diffusion of Cu in a Cu-Zr MG is confined in the liquidlike regions that are poor in icosahedral short-range order, and Bokas *et al.* [23] found that in Al-Sm MGs the diffusion coefficient of Al with ICO-like VP is one order of magnitude lower than other Al atoms at low Sm concentration range. In the same vein, Fig. 4.10b shows that DAs are prone to avoid Sm atoms in the sample and that faster DAs (i.e., DAs that have larger displacements within a fixed time window) have stronger avoidance tendency. We speculate that Sm can have an important effect on Al diffusion by increasing the fraction of ICO-like VPs [23]. This would take place not only because Sm increases the fraction of Al-centered ICO-like VPs, but also because most of the Sm-centered clusters are ICO-like. As a result, the average size of liquidlike channels is reduced and it takes a longer time for Al atoms to navigate the torturous diffusion paths inside the narrower channels. Finally, the fact that the sizes

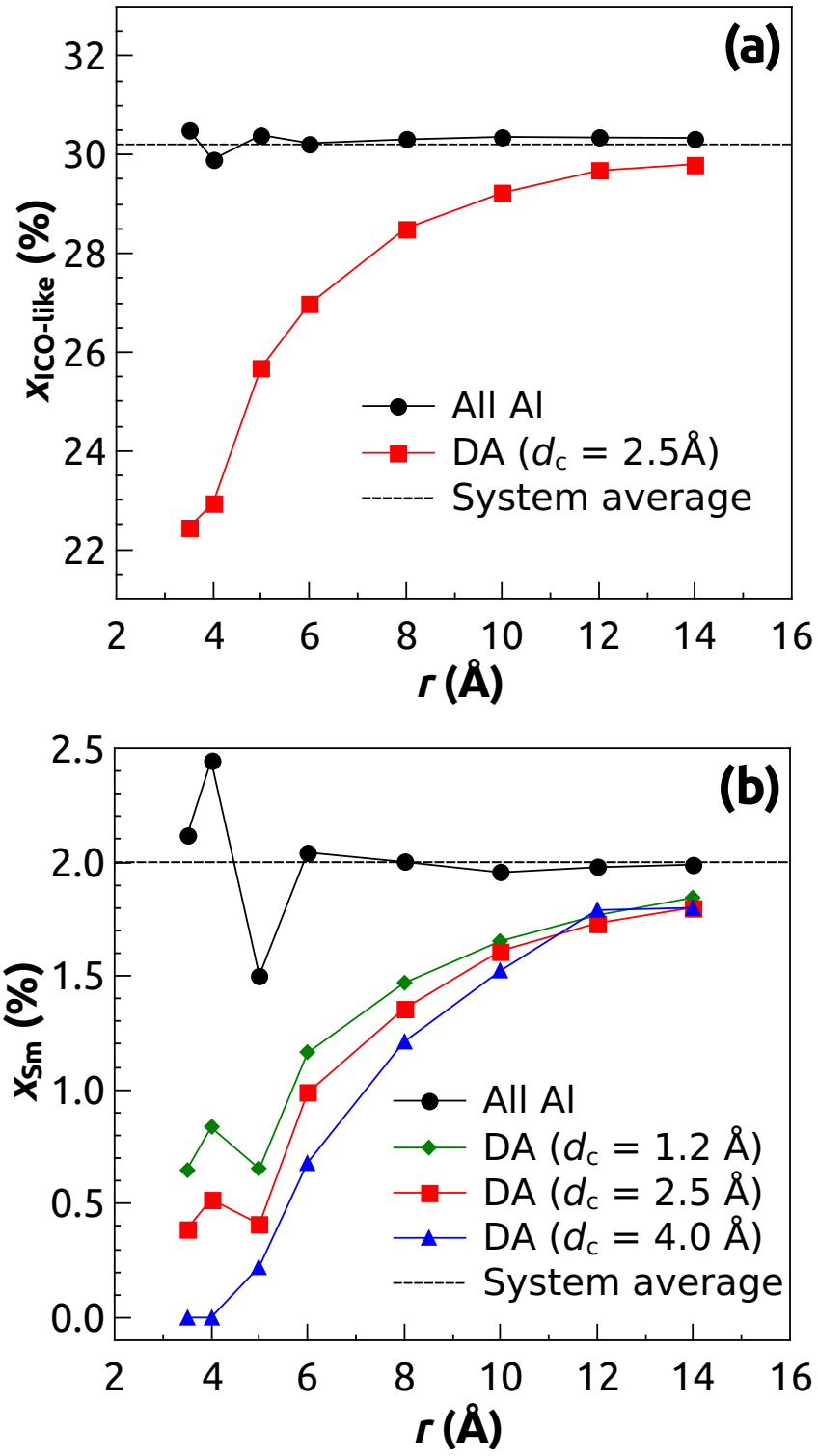

Fig. 4.10: (Color online) (a) ICO-like VP concentration $x_{\text{ICO-like}}$ and (b) Sm concentration x_{Sm} around the central diffusing Al atom. These concentrations around any Al atom and the system average concentrations are also plotted for comparison. The diffusing events are defined using $\Delta t = 100$ ps and different d_c.

of liquidlike channels and DA-clusters correlate with each other explains the decreasing size of DA-clusters with increasing x_{Sm}, as shown in Fig. 4.9c.

4.3.4.2 Nucleation attachment mechanism

In order to illustrate the mechanism of Al attachment during nucleation, Fig. 4.11 presents the snapshots of Al attachment process during the growth of a nucleus in the system with x_{Sm} = 2.0 at.% and $T = 0.95\,T_{\mathrm{g}}$. In the first image, the grey atoms are the original FCC atoms at $t = 0$ ps and they are used to construct an isosurface shown also in grey. In the following images (at longer times), only newly attached atoms are shown explicitly, and the colors and arrows, respectively, represent the magnitude and the direction of the atom's displacement relative to its position at $t = 0$ ps. From the images shown in Fig. 4.11, one can see that the attachment is heterogeneous in space and atoms tend to attach to nuclei collectively as a cluster. Examples of these clusters are marked with the blue ellipses in the images in Fig. 4.11.

The attachment is not only heterogeneous in space, but also in time. The temporal heterogeneity of attachment was verified by tracking the dynamic fluctuation of the instantaneous net increase N_{net} of the number of atoms added to the nucleus within the period of 10 ps, i.e., $N_{\mathrm{net}} = N_{\mathrm{att}} - N_{\mathrm{det}}$, where N_{att} and N_{det} are the instantaneous numbers of attachment and detachment events within 10 ps, respectively. Fig. 4.12 shows N_{net} vs. time t for a nucleus growing from 17 atoms to 189 atoms within 3.7 ns; during this time there are in total 4757 attachment events and 4585 detachment events. One can see that N_{net} exhibits strong fluctuations, which indicates the temporal heterogeneity of the nucleus growth. To further demonstrate this temporal heterogeneity, the simulation method was modified to numerically model a randomized nucleus growth. For the analysis, the following simplifying assumptions were made: 1) The nucleus is spherical and the nucleus surface area $A = (4\pi)^{\frac{1}{3}}(3NV_0)^{\frac{2}{3}}$, where N and V_0 are the number of nucleus atoms and the atomic volume, respectively; 2) the probability of attachment and

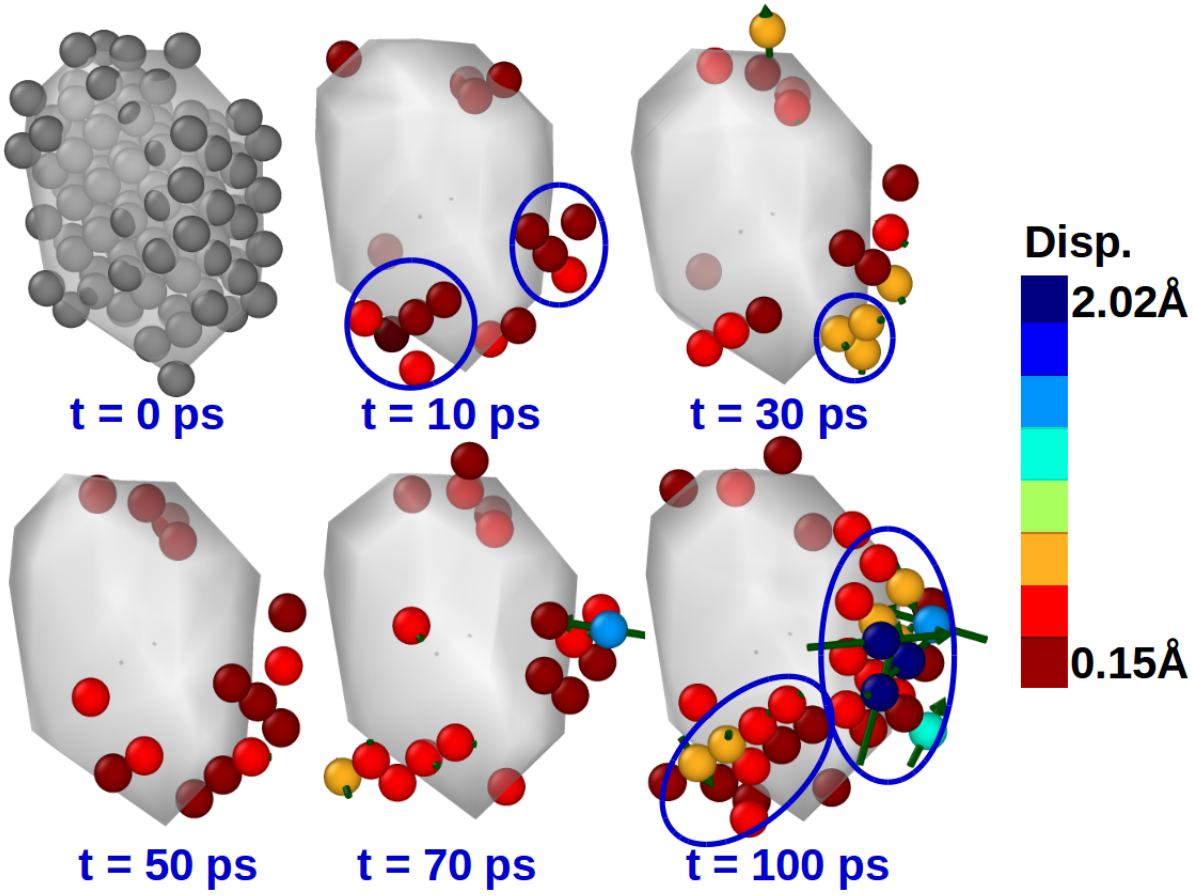

Fig. 4.11: (Color online) Nucleus attachment process for x_{Sm} = 2.0 at.% and $T = 0.95\,T_{\mathrm{g}}$. The isosurface represents the original nucleus surface at $t = 0$ ps. The color atoms are those that attach to nucleus subsequently. Color of the atoms and arrow represent the magnitude and direction of the displacement vector of a given atom.

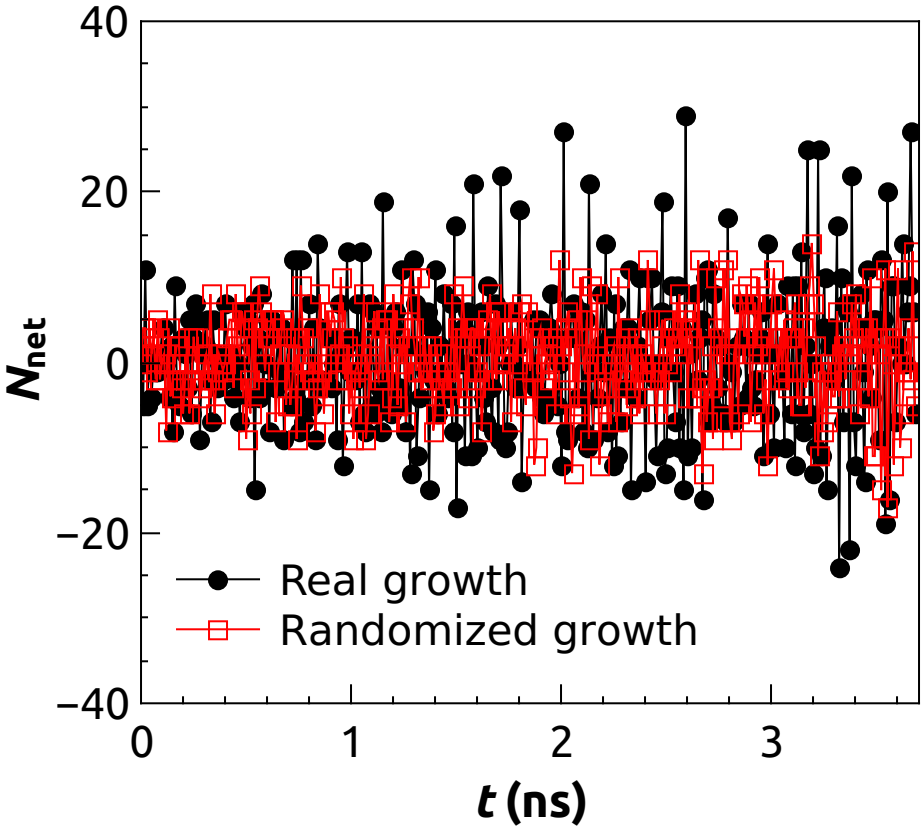

Fig. 4.12: (Color online) The instantaneous net increase, N_{net}, of the number of atoms in the nucleus within 10 ps for real and randomized nucleus growth.

detachment at any time is proportional to the nucleus surface area; and 3) the numbers of attachment and detachment events are the same as found in the full MD simulations with x_{Sm} = 2.0 at.% and $T = 0.95\,T_g$, i.e., $N_{att} = 4757$ and $N_{det} = 4585$. The randomized fluctuation of N_{net} is also plotted in Fig. 4.12. Clearly, the N_{net} fluctuation amplitude in randomized nucleus growth is much smaller than in the case of the real nucleus growth. This means that attachment of atoms to nuclei in a real system is not random and it is heterogeneous in time. The difference in N_{net} fluctuation in Fig. 4.12 can be attributed to the different nucleus growth modes (i.e., single atom attachment versus collective attachment) in these two systems.

In summary, our analysis shows that both Al diffusion and Al nucleation attachment

occur highly heterogeneously via collective jumps of a group of atoms. The common features of these physical processes may explain why the kinetic barrier Q of Al nucleation is comparable to the activation barrier E_{Al} of Al diffusion, as shown in Fig. 4.7.

4.4 Discussion

It has been suggested [50] that the homogeneous nucleation delay time τ is inversely proportional to the atomic attachment rate to nucleus, that is, $\tau \propto 1/\omega^*$. Combining the exponential law of τ (see Fig. 4.5a) and Eq. (4.2), taking the logarithm of both sides, and omitting constant terms, one can find that $Q \propto x_{\mathrm{Sm}}$. This analysis is consistent with data shown in Fig. 4.7, where the dependence of the mean value of the attachment kinetic barrier Q on Sm concentration x_{Sm} can be well approximated by a linear function (despite the large error bar of Q at higher concentrations). This consistence implies a good agreement between our simulations and the theory.

Our simulation results show that, in the composition range (0.0 - 3.0 at.% Sm) studied, the nucleation kinetics in Al-Sm MG is governed by the interfacial attachment process. Mechanisms underlying Al interfacial attachment and Al diffusion share critical atomic-level features, i.e., they both occur heterogeneously through collective jumps of a group of atoms. The fact that the nucleation kinetic barrier Q is smaller than E_{Sm}, as seen in Fig. 4.7, suggests that the bulk diffusion of Sm is not involved in the nucleation process. As the Sm concentration is low, most Sm atoms might be transported away from the nucleus via the local rearrangement between Sm and Al atoms, while others are incorporated into the nucleus. The dominant role of the interfacial attachment mechanism might not hold true for nucleation at high Sm concentration or in the crystal growth regime (past the critical nucleus radius). In those cases it is possible that a Sm-rich shell is formed around Al nucleus/crystal interface and thereby the diffusion of Sm away from the nucleus/crystal interface might be expected to play the dominant role, as has

been suggested in Refs. [11, 51]. Further studies are needed to confirm the role of solute diffusion in the nucleation kinetics for high solute concentrations.

Although it has been shown that Al nucleation attachment occurs highly heterogeneously via collective jumps of a group of atoms, such a collective attachment mechanism violates CNT which assumes the nucleus growth is continuous via single atom attachment. However, the application of CNT to extract the nucleation kinetic barrier Q in Eq. 4.2 can still be justified, since Q would represent the *average* kinetic barrier per atom in the collective attachment.

4.5 Conclusions

The isothermal nucleation kinetics in Al-Sm MG was studied with x_{Sm} in the range of 0.0 - 3.0 at.%. The following general conclusions can be drawn from the results of our MD simulations:

(1) Sm solutes significantly suppress the primary crystallization transformation in Al-Sm MG and thereby they enhance its glass formability. In particular, the nucleation delay time increases exponentially with x_{Sm} at a constant T/T_{g} ratio, whereas the critical cooling rate R_{c} decays exponentially with x_{Sm}. In addition, a reasonable range of R_{c} (2.24×10^4 - 1.59×10^6 K/s) has been predicted for $Al_{92}Sm_8$, which is a well-known marginal glass former.

(2) Sm solute retards Al nucleation by increasing the nucleation kinetic barrier (and therefore by reducing the nucleus attachment rate). In the composition range considered in this study, the nucleation kinetics is controlled by interfacial attachments, rather than by Sm diffusion.

(3) Similarly to Al diffusion in MGs, attachment of Al to a crystalline nucleus takes place heterogeneously in both space and time via the collective jump of a chain or ring of

atoms. The common atomic-level processes between Al attachment and Al diffusion is consistent with the two processes having comparable activation energy barriers.

References

[1] L Zhao, GB Bokas, Perepezko JH, and Szlufarska I. Nucleation kinetics in al-sm metallic glasses. *to be submitted to Acta Materialia*, 2017.

[2] W Klement, RH Willens, and POL Duwez. Non-crystalline structure in solidified gold–silicon alloys. *Nature*, 187:869–870, 1960.

[3] AL Greer, KL Rutherford, and IM Hutchings. Wear resistance of amorphous alloys and related materials. *Int. Mater. Rev.*, 47(2):87–112, 2002.

[4] Christopher A Schuh, Todd C Hufnagel, and Upadrasta Ramamurty. Mechanical behavior of amorphous alloys. *Acta Mater.*, 55(12):4067–4109, 2007.

[5] Golden Kumar, Hong X Tang, and Jan Schroers. Nanomoulding with amorphous metals. *Nature*, 457(7231):868–872, 2009.

[6] A Inoue and A Takeuchi. Recent development and application products of bulk glassy alloys. *Acta Mater.*, 59(6):2243–2267, 2011.

[7] Akihisa Inoue, Katsumasa Ohtera, An-Pang Tsai, Hisamichi Kimura, and Tsuyoshi Masumoto. Glass transition behavior of Al-Y-Ni and Al-Ce-Ni amorphous alloys. *Jpn. J. Appl. Phys.*, 27(9A):L1579, 1988.

[8] Y He, GM Dougherty, GJ Shiflet, and SJ Poon. Unique metallic glass formability and ultra-high tensile strength in Al-Ni-Fe-Gd alloys. *Acta Metall. et Mater.*, 41(2):337–343, 1993.

[9] Y He, SJ Poon, and GJ Shiflet. Synthesis and properties of metallic glasses that contain aluminum. *Science*, 241(4873):1640, 1988.

[10] JC Foley, DR Allen, and JH Perepezko. Analysis of nanocrystal development in Al-Y-Fe and Al-Sm glasses. *Scr. Mater.*, 35(5):655–660, 1996.

[11] G Wilde, H Sieber, and JH Perepezko. Glass formation versus nanocrystallization in an Al92Sm8 alloy. *Scr. Mater.*, 40(7):779–783, 1999.

[12] H Chen, Y He, GJ Shiflet, and SJ Poon. Mechanical properties of partially crystallized aluminum based metallic glasses. *Scr. Metall. et Mater.*, 25(6):1421–1424, 1991.

[13] Yeong-Hwan Kim, Akihisa Inoue, and Tsuyoshi Masumoto. Increase in mechanical strength of Al–Y–Ni amorphous alloys by dispersion of nanoscale fcc-Al particles. *Mater. Trans., JIM*, 32(4):331–338, 1991.

[14] Yeong-Hwan Kim, Akihisa Inoue, and Tsuyoshi Masumoto. Ultrahigh mechanical strengths of $Al_{88}Y_2Ni_{10-x}M_x$ (M= Mn, Fe or Co) amorphous alloys containing nanoscale fcc-Al particles. *Mater. Trans., JIM*, 32(7):599–608, 1991.

[15] ZH Huang, JF Li, QL Rao, and YH Zhou. Primary crystallization of Al–Ni–RE amorphous alloys with different type and content of RE. *Mater. Sci. Eng., A*, 489(1):380–388, 2008.

[16] ZH Huang, JF Li, QL Rao, and YH Zhou. Effects of replacing Ni by Co on the crystallization behaviors of Al–Ni–La amorphous alloys. *Intermet.*, 16(5):727–731, 2008.

[17] JH Perepezko, RI Wu, R Hebert, and G Wilde. Synthesis and stability of amorphous Al alloys. In *MRS Proc.*, volume 644, pages L4–7. Camb. Univ. Press, 2000.

[18] RI Wu, G Wilde, and John H Perepezko. Glass formation and primary nanocrystallization in Al-base metallic glasses. *Mater. Sci. Eng., A*, 301(1):12–17, 2001.

[19] John H Perepezko and Rainer J Hebert. Amorphous aluminum alloys-synthesis and stability. *JOM*, 54(3):34–39, 2002.

[20] DR Allen, JC Foley, and JH Perepezko. Nanocrystal development during primary crystallization of amorphous alloys. *Acta Mater.*, 46(2):431–440, 1998.

[21] Steve Plimpton. Fast parallel algorithms for short-range molecular dynamics. *J. Comput. Phys.*, 117(1):1–19, 1995.

[22] MI Mendelev, F Zhang, Z Ye, Y Sun, MC Nguyen, SR Wilson, CZ Wang, and KM Ho. Development of interatomic potentials appropriate for simulation of devitrification of Al90Sm10 alloy. *Model. Simul. Mater. Sci. Eng.*, 23(4):045013, 2015.

[23] GB Bokas, L Zhao, JH Perepezko, and I Szlufarska. On the role of Sm in solidification of Al-Sm metallic glasses. *Scr. Mater.*, 124:99–102, 2016.

[24] Caroline Desgranges and Jerome Delhommelle. Molecular simulation of the crystallization of aluminum from the supercooled liquid. *J. Chem. Phys.*, 127(14):144509, 2007.

[25] ZY Hou, KJ Dong, ZA Tian, RS Liu, Zhen Wang, and JG Wang. Cooling rate dependence of solidification for liquid aluminium: A large-scale molecular dynamics simulation study. *Phys. Chem. Chem. Phys.*, 18(26):17461–17469, 2016.

[26] HR Wendt and Farid F Abraham. Empirical criterion for the glass transition region based on monte carlo simulations. *Phys. Rev. Lett.*, 41(18):1244, 1978.

[27] Pieter Rein Ten Wolde, Maria J Ruiz-Montero, and Daan Frenkel. Numerical calculation of the rate of crystal nucleation in a lennard-jones system at moderate undercooling. *J. Chem. Phys.*, 104(24):9932–9947, 1996.

[28] Li-Li Zhou, Run-Yu Yang, Ze-An Tian, Yun-Fei Mo, and Rang-Su Liu. Molecular dynamics simulation on structural evolution during crystallization of rapidly supercooled Cu50Ni50 alloy. *J. Alloys Compd.*, 690:633–639, 2017.

[29] Alexander Stukowski. Structure identification methods for atomistic simulations of crystalline materials. *Model. Simul. Mater. Sci. Eng.*, 20(4):045021, 2012.

[30] AG Walton. Nucleation in liquids and solutions. *Nucleation*, pages 225–307, 1969.

[31] I Markov. Crystal Growth for Beginners: Fundamentals of Nucleation, Crystal Growth and Epitaxy, 2003.

[32] P Fielitz, M-P Macht, V Naundorf, and G Frohberg. Diffusion in ZrTiCuNiBe bulk glasses at temperatures around the glass transition. *J. Non-Cryst. Solids*, 250:674–678, 1999.

[33] K Knorr, M-P Macht, K Freitag, and H Mehrer. Self-diffusion in the amorphous and supercooled liquid state of the bulk metallic glass $Zr_{46.75}Ti_{8.25}Cu_{7.5}Ni_{10}Be_{27.5}$. *J. Non-Cryst. Solids*, 250:669–673, 1999.

[34] MI Mendelev, MJ Kramer, RT Ott, DJ Sordelet, D Yagodin, and P Popel. Development of suitable potentials for simulation of liquid and amorphous Cu-Zr alloys. *Philos. Mag.*, 11:967–987, 2009.

[35] Zhaoyang Hou, Zean Tian, Rangsu Liu, Kejun Dong, and Aibing Yu. Formation mechanism of bulk nanocrystalline aluminium with multiply twinned grains by liquid quenching: A molecular dynamics simulation study. *Comput. Mater. Sci.*, 99:256–261, 2015.

[36] MI Mendelev, MJ Kramer, Chandler A Becker, and M Asta. Analysis of semi-empirical interatomic potentials appropriate for simulation of crystalline and liquid Al and Cu. *Philos. Mag.*, 88(12):1723–1750, 2008.

[37] ON Senkov and DB Miracle. Effect of the atomic size distribution on glass forming ability of amorphous metallic alloys. *Mater. Res. Bull.*, 36(12):2183–2198, 2001.

[38] RO Suzuki, Y Komatsu, KF Kobayashi, and PH Shingu. Formation and crystallization of Al-Fe-Si amorphous alloys. *J. Mater. Sci.*, 18(4):1195–1201, 1983.

[39] FF Abraham. Homogeneous Nucleation: The Pretransition Theory of Vapor Condensation, 1974.

[40] Jonathan A Dantzig and Michel Rappaz. *Solidification*. EPFL press, 2009.

[41] Dimo Kashchiev. *Nucleation: Basic Theory with Applications*. Butterworth-Heinemann, 2000.

[42] D Kashchiev and GM Van Rosmalen. Review: nucleation in solutions revisited. *Cryst. Res. Technol.*, 38(7-8):555–574, 2003.

[43] Miguel A Durán-Olivencia and James F Lutsko. Unification of classical nucleation theories via a unified Itô-Stratonovich stochastic equation. *Phys. Rev. E*, 92(3):032407, 2015.

[44] Franz Faupel, Werner Frank, Michael-Peter Macht, Helmut Mehrer, Volkmar Naundorf, Klaus Rätzke, Herbert R Schober, Suman K Sharma, and Helmar Teichler. Diffusion in metallic glasses and supercooled melts. *Rev. Mod. Phys.*, 75(1):237, 2003.

[45] Y Zhang, CZ Wang, MI Mendelev, F Zhang, MJ Kramer, and KM Ho. Diffusion in a Cu-Zr metallic glass studied by microsecond-scale molecular dynamics simulations. *Phys. Rev. B*, 91(18):180201, 2015.

[46] Subrahmanyan Chandrasekhar. Stochastic problems in physics and astronomy. *Rev. Mod. Phys.*, 15(1):1, 1943.

[47] YQ Cheng, E Ma, and HW Sheng. Alloying strongly influences the structure, dynamics, and glass forming ability of metallic supercooled liquids. *Appl. Phys. Lett.*, 93(11):111913, 2008.

[48] HL Peng, MZ Li, WH Wang, C-Z Wang, and KM Ho. Effect of local structures and atomic packing on glass forming ability in CuxZr100-x metallic glasses. *Appl. Phys. Lett.*, 96(2):021901, 2010.

[49] JL Finney. Random packings and the structure of simple liquids. I. The geometry of random close packing. In *Proc. R. soc. Lond. A-Math. Phys. Eng. Sci.*, volume 319, pages 479–493. The R. Soc., 1970.

[50] Kenneth C Russell. Nucleation in solids: the induction and steady state effects. *Adv. Colloid Interface Sci.*, 13(3-4):205–318, 1980.

[51] SD Imhoff, J Ilavsky, F Zhang, P Jemian, PG Evans, and JH Perepezko. Kinetic transition in the growth of Al nanocrystals in Al-Sm alloys. *J. Appl. Phys.*, 111(6):063525, 2012.

Chapter 5 : Nucleation of Five-fold Growth Twins in Al-base Alloys

The nucleation mechanism of five-fold twins in Al alloys was investigated using molecular dynamics simulations. The simulation results reveals a new nucleation pathway for five-fold twins [1], which does not require any nucleation templates. Through the comparative studies among Al-Sm and Al-Mg model alloys, it has been found that the TB energy plays a dominant role in the twining and five-fold twinning frequency. Although nucleation process involves the formation of pentagon structure, the structural factor turns out not to correlate strongly with the five-fold twinning frequency. The nucleation mechanism revealed in this work would help with the understanding of formation of multiple twinned structures and contribute to the microstructure engineering of novel materials.

5.1 Introduction

Although grain refinement can increase the yield strength and hardness for bulk micro- and nano-crystalline (nc) alloys (known as Hall-Petch effect [2]), these beneficial attributes often come at the expense of substantially lowered ductility and resistance to stable fracture under monotonic and cyclic loading [3]. In contrast, TB strengthening can preserve the ductility of materials. For instance, bulk nc alloys with fine twin structures usually exhibit extraordinary overall mechanical properties, including both increased strength and good tensile ductility, as compared to their regular ultrafine grained counterparts [3, 4]. Such a preservation of material ductility has been attributed to the switch of the dominant slip mechanism from full dislocation activities to TB migration via slip

of partial dislocations, which are emitted at intersections between GBs and TBs [5]. This TB migration mechanism accommodates a considerable amount of plastic strain and hence preserves the material ductility [3]. Therefore, the tailored creation of fine twin structures has become a promising microstructure engineering strategy for design of polycrystalline metals and alloys with excellent overall mechanical properties. However, the control over the twin density and twin size during the introduction of TBs in bulk form becomes a practical challenge.

Among the twinned structures, five-fold twins (five {111} neighboring twins that share a common ⟨110⟩ direction and have a five-fold symmetry relationship) have recently attracted a growing interest due to their unique microstructures and controversial formation mechanisms [6–12]. These mechanisms include the different variants of sequential twinning mechanisms [6, 7] for the five-fold deformation twins, and sequential twinning [8] or GB migration mechanism [9] for five-fold annealing twins. In addition, five-fold growth twins have not only been suggested to correlate with effective grain refinement in Al and gold alloys [10, 11, 13], they might also be responsible for the formation of twinned dendrites [14, 15], a morphology known in industrial direct chill-cast Al alloys for over 60 years and whose origin is still unclear for lack of understanding of the five-fold twinning mechanism [16].

To our best knowledge, the formation mechanism for five-fold growth twins has only been limitedly studied. For instance, Kurtuldu *et al.* [10, 11] proposed that, in Al-Zn-Cr alloy and yellow gold doped with Ir, five-fold twins would nucleate through an epitaxial growth on the facets of pre-existing metastable icosahedral quasicrystals (iQCs), which form around the icosahedral short-range order template in the liquid state. However, this mechanism remains a conjecture, as neither the nucleation process was directly observed, nor was there any solid evidence of the formation of iQCs in these specific alloys. More recently, Hou *et al.* [12] performed large-scale MD simulations of the rapid solidification of pure Al and reported that the five-fold twins result from the successive

formation of the five TBs, which depicts a visualized formation pathway of the five-fold growth twins. However, the controlling factor and the solute effect is still obscure in this process.

Here, in order to advance the design of tailored morphology of twin structures, we carried out MD simulations to investigate the nucleation mechanism of five-fold twins during solidification of Al alloys, with a focus on identifying the dominant factors in the five-fold twinning. Since empirical potentials for Al-Zn-Cr alloy and yellow gold alloy are not available so far, Al-Sm and Al-Mg alloys are studied here as the model systems. This is not only because of the availability of the empirical or semi-empirical potentials [17–19] for both Al-Sm and Al-Mg alloys, but also because MD simulations with these potentials have predicted the formation of five-fold growth twins.

5.2 Computational Methods

MD simulations are performed using the LAMMPS simulation package [20] based on empirical potentials for Al-Sm and Al-Mg alloys. Specifically, we apply both the Finnis-Sinclair (FS) potential [17] and embedded atom method (EAM) potential [18] for Al-Sm systems, and FS potential [19] for Al-Mg system. In all the simulations throughout this paper, an adaptive CNA method [21] was used for the structure identification, which examines the local environment to classify each atom as different structural types such as FCC, BCC, HCP, and amorphous structure.

5.2.1 Isothermal solidification

We simulated the isothermal solidification of Al-Sm and Al-Mg model alloys. In particular, a $9 \times 9 \times 9$ nm^3 simulation box was used, which contained a total of 42 thousand atoms, and the periodic BCs were enforced in all three Cartesian directions. An isothermal-isobaric (NPT) ensemble was used and the temperature and pressure were controlled with the Nose-Hoover thermostat and barostat, respectively. The nominal

pressure was maintained to 0 GPa. The samples were quenched from well-mixed liquid state and held at the temperature of 470 K to solidify. From the simulations, the atomic-scale nucleation pathway and the possible controlling factors of five-fold twinning were first identified. Then we calculated the propensity of twinning (PoT), defined as the fraction of the number of HCP atoms among the total number of crystalline atoms, and obtained the statistics of the frequency of five-fold twins in these model systems. The effect of both TB energy (see Sec. 5.2.2 for the calculation method) and the structural factor on the twinning and five-fold twins were finally analyzed.

5.2.2 TB energy

TB energy E_{TB} is the excess energy of crystalline materials due to the introduction of $\{111\}$ twins. Here, the value of E_{TB} for Al-Sm and Al-Mg alloys were calculated as follows. Firstly, we randomly doped both the single crystal and bicrystal samples, as shown in Figs. 5.2a and 5.2b, with the same amount of solute atoms. Both samples have the same geometry ($7.5 \times 8.0 \times 5.6$ nm^3) with 20 thousand atoms. We used NPT ensemble and applied periodic BCs in all three Cartesian directions. As in Sec. 5.2.1, the temperature and pressure were controlled with the Nose-Hoover thermostat and barostat, respectively. The nominal pressure was maintained to 0 GPa. Secondly, a hybrid Monte Carlo (MC) + MD method was used for the system relaxation. The systems were maintained at 550 K for 0.5 ns, and 5,000 MC attempts were invoked every 5 ps to randomly swap Al atoms with solute atoms. The swap probability was calculated based on the Metropolis criterion. The solute segregation to TBs is expected to take place during this process. After the relaxation, the system energy was minimized using the conjugate gradient algorithm while maintaining the external pressure of 0 GPa. Finally, TB energy is defined as $E_{\mathrm{TB}} = (E_{\mathrm{b}} - E_{\mathrm{s}})/2A$, where E_{b} and E_{s} are the potential energies of the bicrystal and single crystal, respectively, and $2A$ is the total TB area in the bicrystal sample.

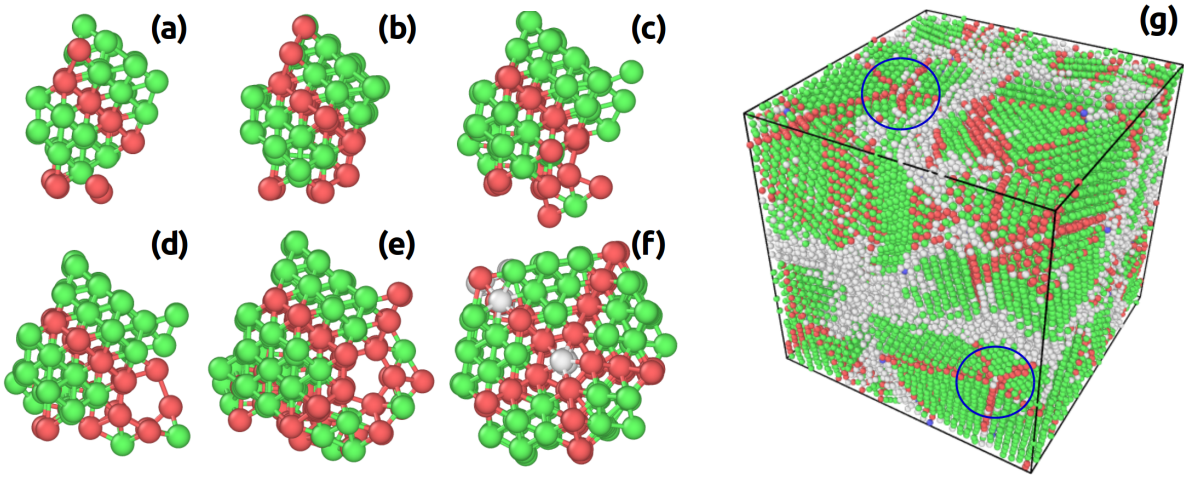

Fig. 5.1: (Color online) (a)-(f) The nucleation snapshots of five-fold twins and (g) a typical twined structure in FS Al-1Sm system solidified at 470 K, where the five-fold twins are marked with blue circles. The green, red and while colors represent FCC, HCP and amorphous atoms, respectively.

5.3 Results

5.3.1 Nucleation pathway of the five-fold growth twins

In the simulations, the five-fold twins have been observed during the isothermal solidification of both Al-Mg and Al-Sm alloys with different solute concentrations. In order to identify the nucleation pathway, these five-fold twins were traced back to the liquid state. It has been found that the five-fold twinning in different model systems follows a common nucleation pathway, as depicted in Fig. 5.1. One can see that, the five-fold twins start with the intersection of two initial non-coplanar TBs, which is then followed by the formation of a local pentagon structure around the intersection line. The pentagon structure consists of 5 HCP atoms and, along with the initial two TBs, becomes a prototype which promotes the subsequent formation of the rest 3 twins.

Note that during this nucleation process, neither the pre-existing iQC phase nor the

icosahedral cluster has been observed near the center of five-fold twins. This suggests that the iQC nucleation template is not required in the five-fold twinning in these model systems. In the meantime, the nucleation pathway also suggests that the intersection of two initial TBs and the formation of pentagon structure are the prerequisites for the formation of five-fold twins, therefore, the inherent propensity of twinning (PoT) and the inherent pentagon population may play significant roles in the five-fold twinning. Both effects will be discussed in the following sections.

5.3.2 Effect of TB energy

5.3.2.1 Calculation of TB energies

As the twinning propensity is energetically correlated with the stacking fault energy E_{SF} or TB energy E_{TB}, therefore, in order to analyze the twinning propensity of different model systems, we first calculated E_{TB} for different systems using the method described in Sec. 5.2.2 and compared them with experimental and computational data available in literature. The results from the calculation in this work as well as the literature are plotted in Fig. 5.2c. Since the empirical relationship $2E_{TB} \approx E_{SF}$ is shown to hold generally [22], therefore, the experimental measurements or calculations of E_{SF} in Refs. [23–27] were converted to the values of E_{TB}. From Fig. 5.2c, one can see that there is a large uncertainty in the values of E_{TB} obtained from different methods and different empirical potentials even for the same material and composition. Therefore, here we use Al-Sm and Al-Mg alloys with potentials in Refs. [17–19] only as the model systems to determine the effect of E_{TB} on the formation of five-fold twins. However, one should be careful interpreting the results as predictions for real Al-Sm and Al-Mg alloys, given the uncertainty in the values of E_{TB}.

In addition, it can also be seen from Fig. 5.2c that the FS potential of Al-Mg predicts a very weak composition dependence of its E_{TB}. In contrast, both FS and EAM potentials give drastically decreasing TB energies for Al-Sm system as Sm concentration increases.

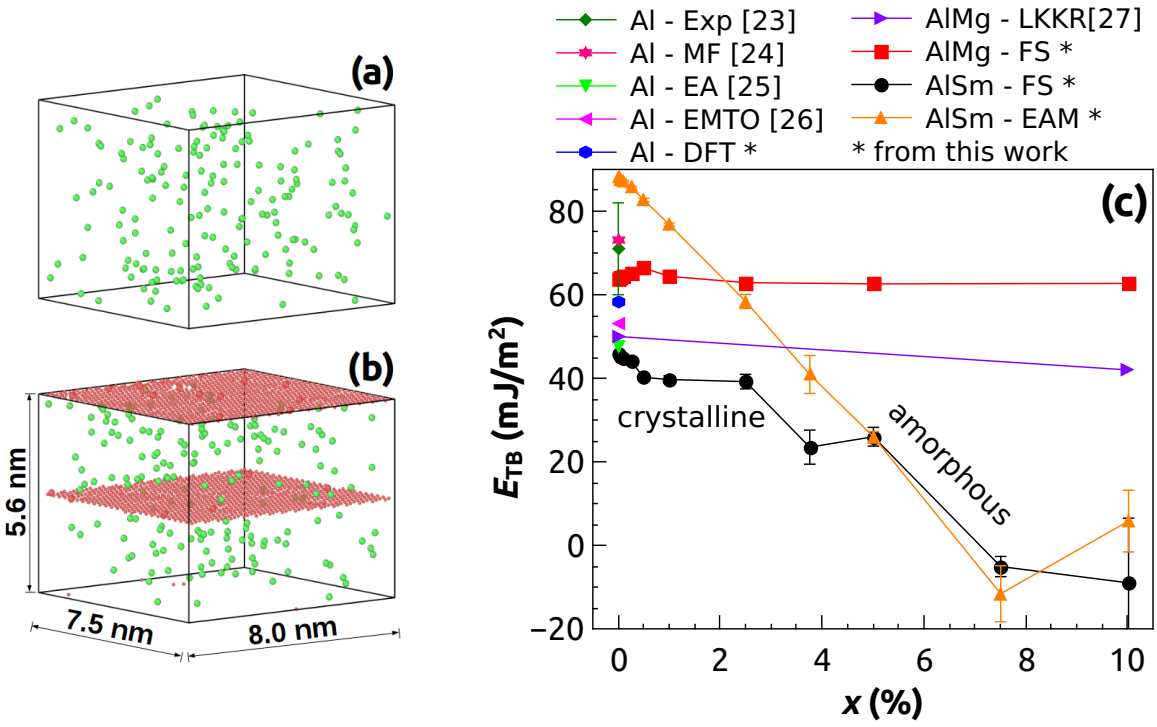

Fig. 5.2: (Color online) (a) Single crystal and (b) bicrystal samples for calculating E_{TB}, where only solute atoms and boundary atoms are shown. (c) E_{TB} v.s. solute concentration x of pure Al, Al-Mg and Al-Sm model systems calculated in this work and obtained from Refs. [23–27]. "Exp", "MF", "EA", "EMTO" and "LKKR" represent experimental measurement [23], prediction from EAM interatomic potential by Mishin and Farkas *et al.* [24], *ab initio* force-matching calculation by Ercolessi and Adams [25], *ab initio* exact muffin-tin orbitals calculation [26] and the layer korringa kohn rostoker method [27], respectively. "DFT", "FS" and "EAM" represent the density functional theory calculation, predictions from FS potential and EAM potential, respectively.

However, one should note that when Sm concentration reaches 5 at.%, we observed a considerable amount of amorphous phase and the distinction between TB and the crystal interior becomes less clear, due to the high temperature (550 K) relaxations in MD simulations. Therefore, these values of E_{TB} for Al-Sm at high Sm concentration are not accurate and are plotted for reference only. Actually, in the following sections, only low solute concentrations (0 - 2 at.%) will be used to study the effect of E_{TB} on twinning.

5.3.2.2 Correlation between TB energy and (five-fold) twinning frequency

In order to show the effect of E_{TB}, we define the propensity of twinning (PoT) as the fraction of the number of HCP atoms among the total number of crystalline atoms in the solidified structures. We chose 5 model systems (Al-Mg FS alloy with 1 at.% and 2 at.% Mg, Al-Sm EAM alloy with 0 at.% and 1 at.% Sm and Al-Sm FS alloy with 1 at.% Sm) and simulated the isothermal solidification as described in Sec. 5.2.1. In order to obtain meaningful statistics of the (five-fold) twinning frequency, 20 independent solidification simulations were performed for each system. As the TB is not the stable structure, the formed TB may disappear in the annealing process, which would result in a decrease of PoT and the number of five-fold twins $N_{5\mathrm{T}}$. Figs. 5.3a and 5.3b show the values of PoT and $N_{5\mathrm{T}}$ in each system, respectively, including both the maximum values in the solidified structure and the (relatively) stable values after annealing for 1.5 ns. From Fig. 5.3 one can see that both PoT and $N_{5\mathrm{T}}$ drop after annealing for all systems, especially for Al-Mg system, indicating the unstable nature of twin structures. Also, it can be seen that even for the same Al-Sm alloy, the FS potential and EAM potential predict totally different propensity of twinning and five-fold twinning frequency. Finally, the large variances of PoT and $N_{5\mathrm{T}}$ have been observed among independent simulations, which suggests a strong stochastic nature of (five-fold) twinning nucleation.

In order to correlate the (five-fold) twinning frequency with TB energy, we plot PoT and $N_{5\mathrm{T}}$ as functions of E_{TB} in Figs. 5.4a and 5.4b, respectively. We can see that the

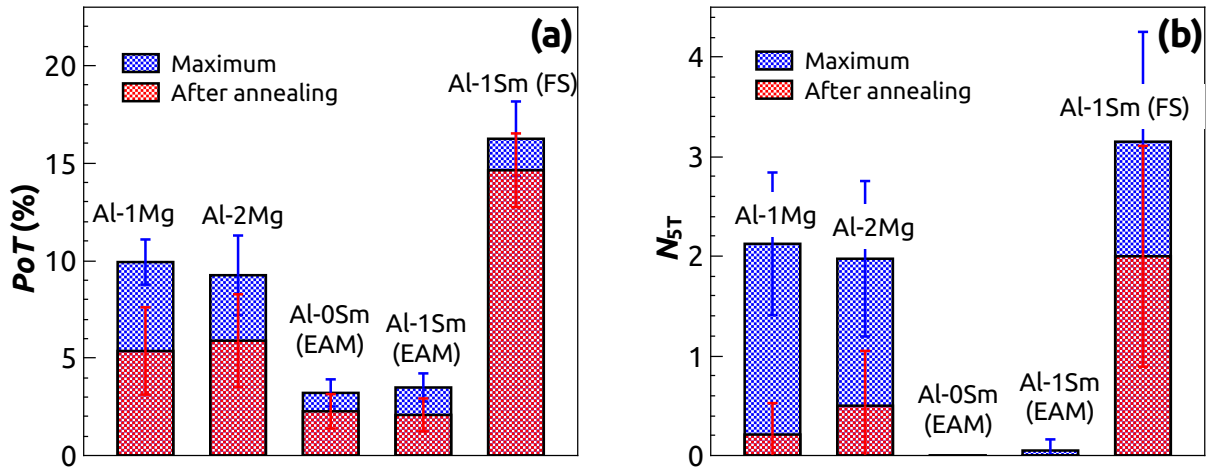

Fig. 5.3: (Color online) (a) Propensity of twinning (PoT) and (b) the number of five-fold twins (N_{5T}) in different model systems, including the maximum values in the solid structure and those after annealing for 1.5 ns.

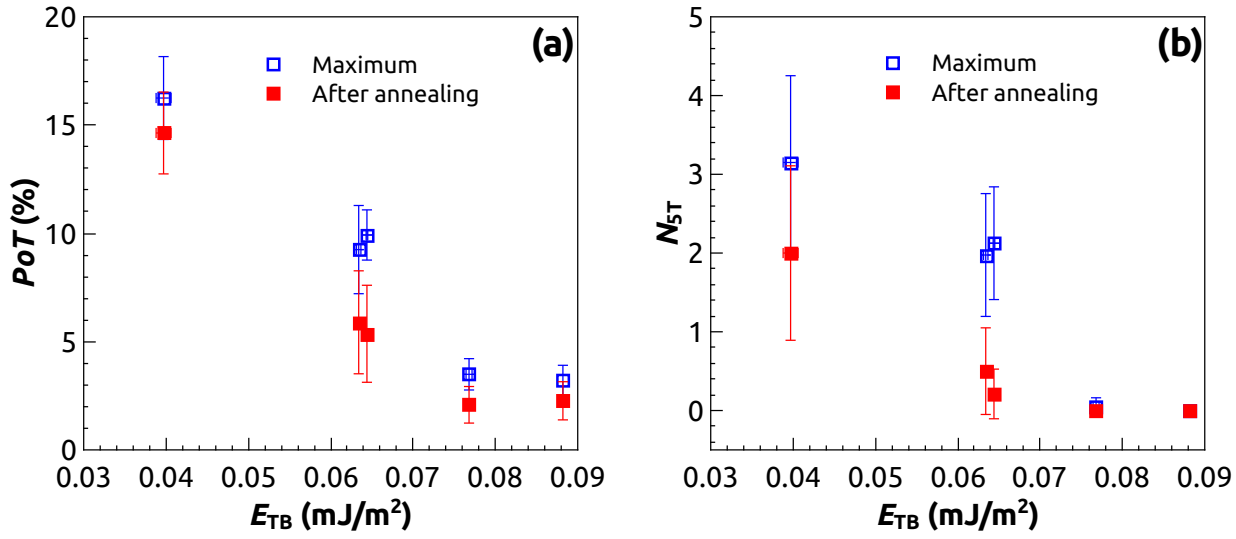

Fig. 5.4: (Color online) (a) Propensity of twinning (PoT) and (b) the number of five-fold twins (N_{5T}) as functions of TB energy E_{TB}.

propensity of twinning and five-fold twinning frequency strongly correlate with the TB energy of materials, that is, both the twinning propensity and five-fold twinning frequency decrease with the increasing TB energy. As E_{TB} reaches above $\sim$0.08 mJ/m^2, the twinning propensity drops to $2-3$ % only and the five-fold twinning becomes very rare to observe.

5.3.3 Effect of pentagon structure

As suggested by the nucleation pathway of five-fold twins in Sec. 5.3.1, not only is the initial TB intersection the prerequisite, but the formation of the pentagon structure is also required in the nucleation process. In order to analyze the effect of pentagon structure on the five-fold twin nucleation, we calculate the degree of five-fold local symmetry W, $W = \sum_i (f_i^5 \times P_i)$ [28], where P_i is the fraction of Voronoi polyhedron type i, and f_i^5 represents the fraction of pentagons in polyhedron type i. The degree of five-fold symmetry is approximately equal to the fraction of pentagons among all populations of polyhedron polygons. Fig. 5.5 shows the maximum degree of five-fold symmetry before the solidification happens, which is actually the inherent pentagon population in the supercooled liquid and is an indicator of easiness to form the pentagon structure during the nucleation of five-fold twins. From Fig. 5.5 one can see that the inherent pentagon populations are all pretty high and they do not differ much from one model system to another (ranging from 0.5 to 0.6). In order to examine the possible correlation between the (five-fold) twinning frequency and the inherent pentagon population, PoT and $N_{5\mathrm{T}}$ are plotted as functions of W in Figs. 5.6a and 5.6b, respectively. Apparently, based on the data we have, no strong correlation can be observed between PoT or $N_{5\mathrm{T}}$ and W, suggesting that for the model systems we studied, the pentagon structure might not be a main factor that controls the five-fold twinning frequency.

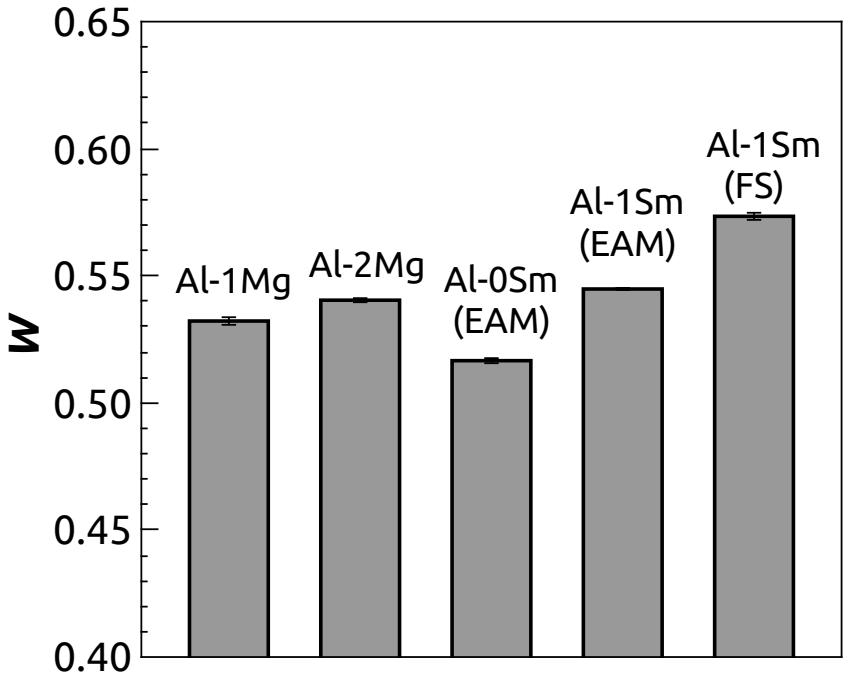

Fig. 5.5: (Color online) Maximum degree W of five-fold symmetry before solidification in different model systems.

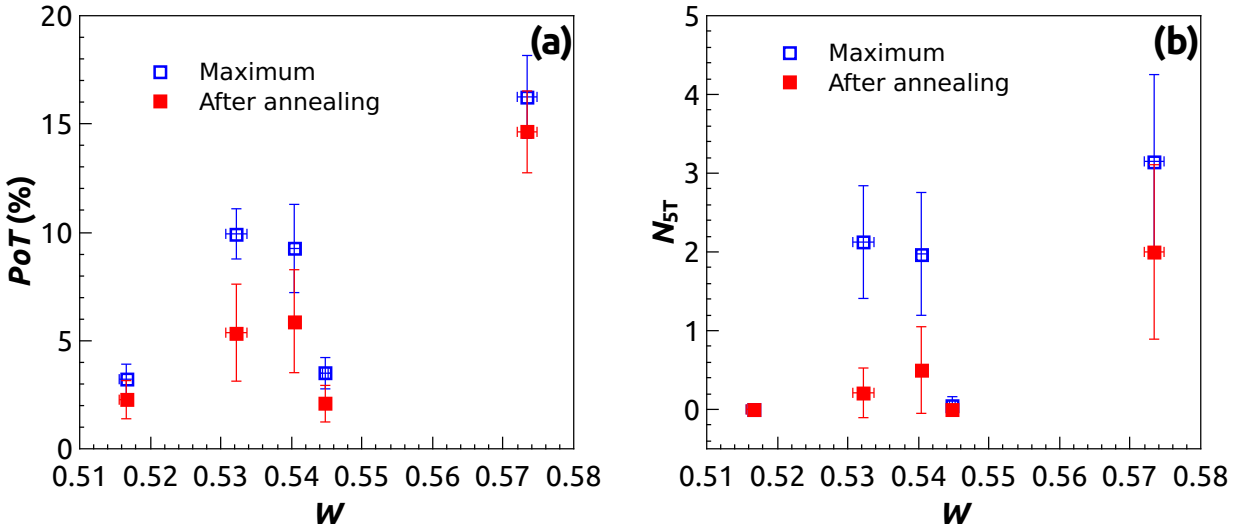

Fig. 5.6: (Color online) (a) Propensity of twinning (PoT) and (b) the number of five-fold twins (N_{5T}) as functions of the degree W of five-fold symmetry.

5.4 Discussion

The nucleation pathway discovered in this work suggests that the pre-existing iQC phase is not required for the five-fold twinning, as no such phase is observed in the model systems. However, it does not rule out the possibility that the metastable iQC phase would be able to promote the five-fold twinning if it was present. In fact, iQCs have been observed in many Al alloys [29]. Lüscher *et al.* [30] has even observed the five-fold twinning of vapor deposited Al textures on the iQC Al-Pt-Mn surface. Therefore, it might be possible that iQC phase, if present, would promote the five-fold twinning during solidification of alloys, as proposed in Refs. [10, 11].

Our analysis suggests that for the model systems studied here, TB energy plays the dominant role in the nucleation of five-fold twins, as it strongly correlates with the twinning propensity and five-fold twinning frequency. The pentagon population, on the other hand, does not exhibit a strong correlation with the twinning propensity or five-fold twinning frequency. This could be because that, the pentagon structures are abundant in each model system and the distinction of the pentagon population may not be able to differentiate these model systems. However, the effect of pentagon structures may be reflected in other cases. For instance, the large-scale MD simulations of solidification of pure Al in Ref. [31] show that the five-fold twin structure can be achieved only at intermediate cooling rates, while fast cooling rates favour the formation of amorphous structures and slow cooling rates favour the formation of FCC crystalline structures with less five-fold twins. The effect of cooling rates can be analyzed as follows. On the one hand, the pentagon population increases with decreasing temperatures [28]. On the other hand, slower cooling rates result in higher crystallization temperatures. Therefore, the slower cooling rate would lead to the lower pentagon population before crystallization, which might limit the formation of five-fold twins.

In addition, we also observed that the annealing temperature affects the (five-fold)

twinning frequency, implying that the atomic dynamics also plays a role in the twinning. In fact, there is a competition between FCC and HCP structures during the crystallization transition [31], and atomic dynamics is a key factor in such a competition.

5.5 Conclusions

The nucleation of five-fold twins was studied in a set of Al base model systems using MD simulations. The following conclusions can be drawn from the comparative studies:

(1) A new nucleation mechanism of five-fold twins was discovered. It has been found that the five-fold twinning starts with the intersection of two initial TBs, which is followed by the formation of a pentagon structure around the nucleation center. The pentagon and initial TBs form the prototype for the formation of subsequent twins.

(2) iQC phase or icosahedral clusters are not required to participate in the nucleation process. Instead, TB energy plays the dominant role in the (five-fold) twinning in the model systems. The general role of pentagon structure needs to be confirmed further.

References

[1] L Zhao, GB Bokas, and Szlufarska I. Nucleation of five-fold growth twins in al-base alloys. *in preparation*.

[2] Thomas H Courtney. Mechanical behavior of materials. 2000.

[3] Ke Lu, Lei Lu, and S Suresh. Strengthening materials by engineering coherent internal boundaries at the nanoscale. *science*, 324(5925):349–352, 2009.

[4] Y-H Zhao, John F Bingert, X-Z Liao, B-Z Cui, Ke Han, Alla V Sergueeva, Amiya K Mukherjee, Ruslan Z Valiev, Terence G Langdon, and Yuntian T Zhu. Simultane-

ously increasing the ductility and strength of ultra-fine-grained pure copper. *Advanced Materials*, 18(22):2949–2953, 2006.

[5] A Frøseth, H Van Swygenhoven, and PM Derlet. The influence of twins on the mechanical properties of nc-al. *Acta Materialia*, 52(8):2259–2268, 2004.

[6] AJ Cao and YG Wei. Formation of fivefold deformation twins in nanocrystalline face-centered-cubic copper based on molecular dynamics simulations. *Applied physics letters*, 89(4):041919, 2006.

[7] YT Zhu, XZ Liao, and XL Wu. Deformation twinning in nanocrystalline materials. *Progress in Materials Science*, 57(1):1–62, 2012.

[8] EM Bringa, Diana Farkas, A Caro, YM Wang, J McNaney, and R Smith. Fivefold twin formation during annealing of nanocrystalline cu. *Scripta Materialia*, 59(12):1267–1270, 2008.

[9] P Huang, GQ Dai, F Wang, KW Xu, and YH Li. Fivefold annealing twin in nanocrystalline cu. *Applied Physics Letters*, 95(20):203101, 2009.

[10] Güven Kurtuldu, Philippe Jarry, and Michel Rappaz. Influence of cr on the nucleation of primary al and formation of twinned dendrites in al–zn–cr alloys: Can icosahedral solid clusters play a role? *Acta Materialia*, 61(19):7098–7108, 2013.

[11] Güven Kurtuldu, Alberto Sicco, and Michel Rappaz. Icosahedral quasicrystal-enhanced nucleation of the fcc phase in liquid gold alloys. *Acta Materialia*, 70:240–248, 2014.

[12] Zhaoyang Hou, Zean Tian, Rangsu Liu, Kejun Dong, and Aibing Yu. Formation mechanism of bulk nanocrystalline aluminium with multiply twinned grains by liquid quenching: A molecular dynamics simulation study. *Comput. Mater. Sci.*, 99:256–261, 2015.

[13] Güven Kurtuldu and Michel Rappaz. Probability of twin boundary formation associated with the nucleation of equiaxed grains on icosahedral quasicrystal templates. In *IOP Conference Series: Materials Science and Engineering*, volume 84, page 012012. IOP Publishing, 2015.

[14] S Henry, M Rappaz, and P Jarry. $\langle 110 \rangle$ dendrite growth in aluminum feathery grains. *Metallurgical and Materials Transactions A*, 29(11):2807–2817, 1998.

[15] MA Salgado-Ordorica and M Rappaz. Twinned dendrite growth in binary aluminum alloys. *Acta Materialia*, 56(19):5708–5718, 2008.

[16] Hasse Fredriksson and Mats Hillert. On the mechanism of feathery crystallisation of aluminium. *Journal of Materials Science*, 6(11):1350–1354, 1971.

[17] MI Mendelev, F Zhang, Z Ye, Y Sun, MC Nguyen, SR Wilson, CZ Wang, and KM Ho. Development of interatomic potentials appropriate for simulation of devitrification of al90sm10 alloy. *Modelling and Simulation in Materials Science and Engineering*, 23(4):045013, 2015.

[18] GB Bokas, Y Shen, L Zhao, HG Sheng, JH Perepezko, and I Szlufarska. Synthesis of sm-al metallic glasses designed by molecular dynamics simulations. *to be submitted to Physical Review B*, 2017.

[19] MI Mendelev, M Asta, MJ Rahman, and JJ Hoyt. Development of interatomic potentials appropriate for simulation of solid–liquid interface properties in al–mg alloys. *Philosophical Magazine*, 89(34-36):3269–3285, 2009.

[20] Steve Plimpton. Fast parallel algorithms for short-range molecular dynamics. *J. Comput. Phys.*, 117(1):1–19, 1995.

[21] Alexander Stukowski. Structure identification methods for atomistic simulations of crystalline materials. *Model. Simul. Mater. Sci. Eng.*, 20(4):045021, 2012.

[22] John P Hirth and Jens Lothe. Theory of dislocations. 1982.

[23] Y Mishin, Diana Farkas, MJ Mehl, and DA Papaconstantopoulos. Interatomic potentials for monoatomic metals from experimental data and ab initio calculations. *Physical Review B*, 59(5):3393, 1999.

[24] Y Mishin, D Farkas, MJ Mehl, and DA Papaconstantopoulos. Interatomic potentials for al and ni from experimental data and ab initio calculations. *MRS Online Proceedings Library Archive*, 538, 1998.

[25] Furio Ercolessi and James B Adams. Interatomic potentials from first-principles calculations: the force-matching method. *EPL (Europhysics Letters)*, 26(8):583, 1994.

[26] Wei Li, Song Lu, Qing-Miao Hu, Se Kyun Kwon, Börje Johansson, and Levente Vitos. Generalized stacking fault energies of alloys. *Journal of Physics: Condensed Matter*, 26(26):265005, 2014.

[27] TC Schulthess, PEA Turchi, A Gonis, and T-G Nieh. Systematic study of stacking fault energies of random al-based alloys. *Acta materialia*, 46(6):2215–2221, 1998.

[28] YC Hu, FX Li, MZ Li, HY Bai, and WH Wang. Five-fold symmetry as indicator of dynamic arrest in metallic glass-forming liquids. *Nature communications*, 6, 2015.

[29] KF Kelton. Quasicrystals: structure and stability. *International materials reviews*, 38(3):105–137, 1993.

[30] R Lüscher, M Erbudak, and Y Weisskopf. Al nanostructures on quasicrystalline al-pd-mn. *Surface science*, 569(1):163–175, 2004.

[31] ZY Hou, KJ Dong, ZA Tian, RS Liu, Zhen Wang, and JG Wang. Cooling rate dependence of solidification for liquid aluminium: a large-scale molecular dynamics simulation study. *Physical Chemistry Chemical Physics*, 18(26):17461–17469, 2016.

Chapter 6 : Conclusions and future directions

6.1 Conclusions

In this thesis, we have applied the multi-scale modeling approach to investigate the microstructural evolution in metallic structural materials, including polycrystalline materials and MGs. In particular, we used phase field method to simulate the GB migration in polycrystalline materials, and used MD simulations to investigate the atomic-level details in the microstructural evolution of Al alloys. These studies bring new insights into the understanding of the fundamentals in the microstructural evolution and contribute to the design of more advanced metallic materials. The following major conclusions can be drawn from these studies:

(1) We developed a multi-physics finite element model which couples strongly and fully the phase field grain growth model with crystal plasticity finite element. The coupled model explicitly includes the plastic driving force for GB migration, and can also qualitatively capture the interaction of dislocations with mobile GBs. The model provides a useful tool to effectively simulating GB migration in metals undergoing large plastic deformations.

(2) The investigation of the nucleation kinetics in Al-Sm MGs with MD simulations reveals the micro-alloying effect of Sm on suppressing the crystallization and enhancing the glass forming ability of Al-Sm MG. Sm solutes were found to delay Al nucleation by increasing the attachment barrier and therefore by reducing the attachment frequency. The analysis shows that the Al attachment has the same characteristics as Al diffusion in MGs and they both take place heterogeneously and collectively.

(3) A new nucleation pathway for the five-fold twins was discovered from the MD simulations of solidification of Al alloys, which does not require the participation of any nucleation templates. The low TB energy and the formation of pentagon structures are prerequisites in the discovered nucleation mechanism. Through the comparative study among Al-Sm and Al-Mg model alloys, it has been found that the TB energy plays the dominant role in the five-fold twinning frequency in these model alloys.

6.2 Future directions

Microstructural evolution in metallic materials is a very broad area and there are plenty of topics worthy of exploration. Here a few interesting future directions related closely to the projects in this thesis are briefly described. First, for the current coupling phase field model developed in this thesis, it would be interesting to implement further the strain gradient theory [1–3] into the framework to account for the grain size effect on the mechanical response to external loading. Strain gradient is associated with the geometrically necessary dislocations, which can be regarded to constitute GB structures. Therefore, more complex GB-dislocation interactions could be captured.

For the Al-Sm MGs, our current study is only limited to low Sm concentrations. To verify the applicability of our conclusions, one may want to perform long-time MD simulations of nucleation reactions for higher Sm concentrations. This will help with the understanding of glass forming ability of real systems. In order to improve the efficiency, the GPU accelerated MD simulation technique [4] can be applied.

Finally, for the study of five-fold twinning in Al alloys, we only considered several model systems. We are still not clear about the roles of iQC (if any) and the pentagon structure in promoting the five-fold twinning. One can embed a dummy iQC to supercooled liquid to observe whether it promotes the formation of five-fold twins, or study a system where iQC is proved to form. In addition, the effect of pentagon structure may

also be clarified through a comparative study of alloys with distinct inherent pentagon fractions.

References

[1] NA Fleck, GM Muller, MF Ashby, and JW Hutchinson. Strain gradient plasticity: theory and experiment. *Acta Metallurgica et Materialia*, 42(2):475–487, 1994.

[2] NA Fleck and JW Hutchinson. Strain gradient plasticity. *Advances in applied mechanics*, 33:296–361, 1997.

[3] William D Nix and Huajian Gao. Indentation size effects in crystalline materials: a law for strain gradient plasticity. *Journal of the Mechanics and Physics of Solids*, 46(3):411–425, 1998.

[4] Christian Robert Trott. *LAMMPScuda-a new GPU accelerated Molecular Dynamics Simulations Package and its Application to Ion-Conducting Glasses.* PhD thesis, Technische Universität Ilmenau, Germany, 2012.